

CERN-PH-TH/2009-108

UMN-TH-2803/09

FTPI-MINN-09/23

Nucleosynthesis Constraints on a Massive Gravitino in Neutralino Dark Matter Scenarios

Richard H. Cyburt¹, John Ellis², Brian D. Fields³,
Feng Luo⁴, Keith A. Olive^{4,5}, and Vassilis C. Spanos⁶

¹*Joint Institute for Nuclear Astrophysics(JINA), National Superconducting Cyclotron
Laboratory(NSCL), Michigan State University, East Lansing, MI 48824, USA*

²*TH Division, Physics Department, CERN, CH-1211 Geneva 23, Switzerland*

³*Center for Theoretical Astrophysics, Departments of Astronomy and of Physics,
University of Illinois, Urbana, IL 61801, USA*

⁴*School of Physics and Astronomy,
University of Minnesota, Minneapolis, MN 55455, USA*

⁵*William I. Fine Theoretical Physics Institute,
University of Minnesota, Minneapolis, MN 55455, USA*

⁶*Department of Physics, University of Patras, GR-26500 Patras, Greece*

Abstract

The decays of massive gravitinos into neutralino dark matter particles and Standard Model secondaries during or after Big-Bang nucleosynthesis (BBN) may alter the primordial light-element abundances. We present here details of a new suite of codes for evaluating such effects, including a new treatment based on `PYTHIA` of the evolution of showers induced by hadronic decays of massive, unstable particles such as a gravitino. We present several sets of results obtained using these codes, including general constraints on the possible lifetime and abundance of an unstable particle decaying into neutralino dark matter under various hypotheses for its decay mechanism. We also develop an analytical treatment of non-thermal hadron propagation in the early universe, and use this to derive analytical estimates for light-element production and in turn on decaying particle lifetimes and abundances, which confirm our numerical results and illuminate the underlying physics. We then consider specifically the case of an unstable massive gravitino within the constrained minimal supersymmetric extension of the Standard Model (CMSSM). We present upper limits on its possible primordial abundance before decay for different possible gravitino masses, with CMSSM parameters along strips where the lightest neutralino provides all the astrophysical cold dark matter density. We do not find any CMSSM solution to the cosmological ${}^7\text{Li}$ problem for small $m_{3/2}$. Discounting this, for $m_{1/2} \sim 500$ GeV and $\tan\beta = 10$ the other light-element abundances impose an upper limit $m_{3/2}n_{3/2}/n_\gamma \lesssim 3 \times 10^{-12}$ GeV to $\lesssim 2 \times 10^{-13}$ GeV for $m_{3/2} = 250$ GeV to 1 TeV, which is similar in both the coannihilation and focus-point strips and somewhat weaker for $\tan\beta = 50$, particularly for larger $m_{1/2}$. The constraints also weaken in general for larger $m_{3/2}$, and for $m_{3/2} > 3$ TeV we find a narrow range of $m_{3/2}n_{3/2}/n_\gamma$, at values which increase with $m_{3/2}$, where the ${}^7\text{Li}$ abundance is marginally compatible with the other light-element abundances.

1 Introduction

Many extensions of the Standard Model of particle physics predict the existence of massive, unstable or metastable particles. If these have lifetimes longer than about a second, their decay products may affect the abundances of light nuclei, such as D, ^4He and ^7Li , produced during Big-Bang nucleosynthesis (BBN). If the particles have lifetimes exceeding about 100 seconds, they decay after BBN, but their decay products may re-process the abundances produced during BBN. Both of these possibilities are strongly constrained by the degree of concordance between abundance predictions of D and ^4He and the observational determination of these abundances, if the baryon density is within the range determined from measurements of fluctuations in the cosmic microwave background radiation (CMB) [1]. This concordance is not only an important vindication of BBN calculations [2–6], but also sets severe limits on the possible abundance of any massive, metastable particle as a function of its lifetime. These limits have been the subject of many previous studies that have modeled both the electromagnetic and hadronic components of the showers induced by the decays of such heavy particles [7]– [28].

We revisit here these constraints using a new suite of codes to model the decay spectra, the evolution of the showers that they induce in the electromagnetic plasma that filled the universe during the epoch between BBN and the decoupling of the CMB, and their potential for either destroying or creating light nuclear species [29]. Studying the decays of heavy particles during BBN requires a code that calculates the direct impact of electromagnetic and/or hadronic showers during nucleosynthesis, rather than just the effects on abundances that had previously been fixed independently by BBN. Our earlier code [20] considered only electromagnetic decays and did not provide constraints for particle lifetimes $\lesssim 10^4\text{s}$. Here we describe a new suite of codes that includes hadronic decays and is applicable also to particles with lifetimes $\lesssim 10^4\text{s}$.

The effects included in this suite of codes are potentially relevant to any extension of the Standard Model that predicts the existence of massive unstable or metastable particles. One example is supersymmetry (SUSY). Many supersymmetric models incorporate a discrete Z_2 symmetry known as R parity. If R parity is not maintained, the lightest supersymmetric particle (LSP) is unstable, and the consistency of BBN with astrophysical observations and the density of baryons inferred from the CMB imposes important constraints on the mechanism and amount of R violation [30]. On the other hand, if R parity is conserved, the LSP is stable, but there is in general a heavier metastable supersymmetric particle. The possibility studied most frequently has been that the LSP is the lightest neutralino χ [31].

In this case, the gravitino would be metastable, and the BBN constraints on its decays impose important limits on the primordial production of gravitinos that are potentially problematic for some inflationary cosmological scenarios [32] - [40]. However, the neutralino is not the only candidate for the LSP, and another generic possibility is the gravitino itself. In this case, the gravitino itself would be stable, but the next-to-lightest supersymmetric particle (NLSP) would in general be metastable, and its decays would be subject to the BBN constraints [41–43].

Our goals in this paper are threefold. The first is to document our new interlocking suite of codes for decay showers in the early universe and their impact on BBN; our codes include the effects of both hadronic and electromagnetic showers, and are applicable to a large range of unstable particle lifetimes. The second goal is to set out the constraints obtained using this code on the lifetime and abundance of a generic unstable or metastable particle, under various plausible hypotheses for its dominant decay modes. The third goal is to explore in more detail the consequences of the shower effects for supersymmetric models with a neutralino LSP. In the context of such models, we demonstrate how our new BBN codes may be used to obtain constraints on the gravitino abundance as a function of its mass.

In previous analyses of the constrained minimal supersymmetric extension of the Standard Model (CMSSM) with a neutralino LSP, cosmological constraints on the decays of the metastable gravitino have usually been ignored. Essentially, it has been assumed implicitly that the gravitino is so heavy, and hence its lifetime is so short, that its decays take place so early in the history of the universe that they do not affect light-element abundances. However, from a theoretical point of view, a large hierarchy between the gravitino and LSP masses may appear unlikely. Indeed, in minimal supergravity (mSUGRA) and related models [44], it is usually the case that the gravitino is not much heavier than the LSP, if it is not the LSP itself. Therefore, it is important to analyze the case when the decays of gravitinos *do* affect the light-element abundances, and evaluate the resulting constraint on the primordial gravitino abundance as a function of its mass.

We exemplify these constraints in the specific case of the CMSSM, in which supersymmetry-breaking gaugino and scalar masses $m_{1/2}$ and m_0 are each assumed to be universal [45,46]. In this case, when the LSP is the lightest neutralino, its relic density $0.0975 < \Omega_{\text{CDM}} h^2 < 0.1223$ as inferred from astrophysical and cosmological measurements [1] constrains $(m_{1/2}, m_0)$ to lie along narrow “WMAP strips” for given fixed values of the other CMSSM parameters [45,47]. Moreover, the gravitino lifetime and decay modes are known as functions of its mass and the CMSSM parameters. Thus, we are able to set firm upper limits on the possible abundance of the gravitino as a function of its mass and $m_{1/2}$. This upper limit on the gravitino abundance

may, in some circumstances, constrain severely the maximum temperature reached in the universe, e.g., following an early inflationary epoch [32] - [40].

The layout of this paper is as follows. In Section 2 we summarize the cosmological data that we use in our analysis. Then, in Section 3 we explain our treatment of the evolution of the hadronic and electromagnetic showers initiated by the decay of a generic metastable particle into the cosmic plasma, and their effects on the primordial light-element abundances. Appendix A summarizes our treatment of hadronic spectra, and describes the propagation of non-thermalized particles in the cosmic plasma. In Section 4 we turn to the specific case in which the gravitino is the metastable particle, relegating some technical details to Appendix B. In Section 5 we discuss the resulting constraints on the abundance of a metastable neutral particle, under plausible assumptions on its dominant decay modes. We consider constraints as a function of a generic particle lifetime, as well as constraints on the gravitino abundance in specific CMSSM scenarios with a neutralino LSP. For $m_{3/2} \leq 1$ TeV, we find no parameter choices where the ${}^7\text{Li}$ abundance can be reconciled with the other light-element abundances. However, for $m_{3/2} > 3$ TeV we find narrow ranges of the gravitino abundance that may reconcile marginally the ${}^7\text{Li}$ and other light-element abundances. Finally, in Section 6 we summarize our conclusions and present some prospects for future work.

2 Cosmological Data

2.1 Light-Element Abundances

The abundances of the light elements D and ${}^4\text{He}$ predicted by BBN theory agree quite well with the values determined by observation, if the baryon-to-photon ratio η is that inferred from CMB measurements [1]. This concordance provides the basis for the constraints on metastable particles to be discussed in this paper. However, there is known to be an issue regarding the abundance of ${}^7\text{Li}$, which we discuss below.

Deuterium provides a powerful constraint, as it is very sensitive to the baryon content in the universe, and thus offers by itself a measure of η . Local deuterium that is measured in the solar neighborhood in the interstellar medium provides a strong lower limit on the cosmological abundance, given that astrophysical effects destroy more deuterium than they produce [48]. Recent observations by FUSE show a wide dispersion in the deuterium abundance in local gas seen via its absorption, $(\text{D}/\text{H})_{\text{local gas}} = (0.5 - 2.2) \times 10^{-5}$ [49]. This surprisingly large spread, taken together with the positive correlation of D/H with temperature and metallicity along various sightlines, led [49] to suggest that deuterium may suffer significant and preferential depletion onto dust grains. In this case the true local interstellar D/H value

would lie at the upper limit of the observed values, giving $(\text{D}/\text{H})_{\text{ISM}} \gtrsim (2.31 \pm 0.24) \times 10^{-5}$. However, extracting a primordial deuterium value requires a Galactic chemical evolution model (e.g., [50]), whose model dependences yield uncertainties in the determination of the primordial deuterium abundance.

A high-redshift, metal-poor system is free of many such model uncertainties. In particular, observing the absorption features of quasar light due to a dense high-redshift cloud can be used to determine the primordial deuterium abundance. Several studies yield results [51–57] that are broadly consistent, but with a reduced $\chi^2_\nu = 2.95$, suggesting that the uncertainties have been underestimated. Taking a weighted mean, we find a “world average” range:

$$\left(\frac{\text{D}}{\text{H}}\right)_p = (2.82 \pm 0.21) \times 10^{-5}, \quad (1)$$

where the error bar has been inflated by a factor of $\sqrt{\chi^2_\nu}$. Because it is likely that systematic errors dominate, an even more conservative approach would be to use the sample variance of the D/H data [2]; this would give $\sigma(\text{D}/\text{H}) = (\pm 0.53) \times 10^{-5}$, i.e., a significantly higher error. In this study we adopt 3.2×10^{-5} as our fiducial upper limit on the D/H abundance, but we also illustrate the effect of significant variations in D/H around this value.

Since ${}^3\text{He}$ is also quite sensitive to the baryon density, one might hope that it too could be used as a baryometer. Observations of HII regions in our own Galaxy yield values of the ${}^3\text{He}/\text{H}$ ratio that are compatible with calculations of the primordial value [58, 59]. However, the extrapolation from the observations to a primordial abundance is complicated by the unknown chemical evolution of ${}^3\text{He}$. Indeed, one does not even know whether ${}^3\text{He}/\text{H}$ is increasing or decreasing with cosmic time. Thus, a primordial extrapolation yields only an order-of-magnitude range of allowable values of ${}^3\text{He}/\text{H}$ [60]. However, if we use the results of [48, 61] that the deuterium abundance is always decreasing with time, and assume that ${}^3\text{He}$ changes relatively slowly, we can adopt their ratio:

$$\left(\frac{{}^3\text{He}}{\text{D}}\right)_p < 1.0 \quad (2)$$

as a conservative constraint on the primordial ${}^3\text{He}/\text{D}$ ratio.

HII regions also yield observations of ${}^4\text{He}$. However, measurements of extra-galactic and metal-poor sources yield *a priori* more reliable estimates of the primordial ${}^4\text{He}$ abundance. Various evaluations of the same data yield differing results ranging from $Y_p = 0.234$ [62] to $Y_p = 0.244$ [63]. These differences point to the dominance of systematic uncertainties [64] over statistical errors. The allowed ranges of systematic shifts are discussed in [65], but their analysis does not provide a full estimate for the systematic error. Subsequently, another

analysis of the data was performed [66], making more realistic assumptions than those used in previous analyses. This analysis found a systematically higher Y_p , with significantly increased errors, suggesting that previous analyses had underestimated their systematics:

$$Y_p = 0.249 \pm 0.009. \quad (3)$$

The inclusion of one of these systematics has been explored in [67], which finds results similar to [66]. In our subsequent analysis, we adopt the lower limit $Y_p > 0.240$.

Lithium is seen in the atmospheres of the most primitive, metal-poor stars in the stellar halo of our Galaxy (extreme Population II). Some $\gtrsim 100$ such stars show a plateau [68] in (elemental) lithium versus metallicity, with a small scatter consistent with observational uncertainties. This insensitivity of Li/H to (proto)-Galactic metal content and thus stellar nucleosynthesis indicates that lithium in these stars has a primordial or at least pre-Galactic origin. An analysis [69] of field halo stars gives a plateau abundance of

$$\left(\frac{\text{Li}}{\text{H}}\right)_{\text{halo}\star} = (1.23^{+0.68}_{-0.32}) \times 10^{-10}, \quad (4)$$

where the errors represent a 95% CL and include both statistical and systematic uncertainties. On the other hand, studies of globular cluster stars generally find higher lithium abundances. The measurement [70] of

$$\left(\frac{\text{Li}}{\text{H}}\right)_{\text{gc}} = (2.19 \pm 0.28) \times 10^{-10}, \quad (5)$$

is consistent with results for other systems: $\text{Li}/\text{H} = (1.91 \pm 0.44) \times 10^{-10}$ [71]; $\text{Li}/\text{H} = (1.69 \pm 0.27) \times 10^{-10}$ [72]; and $\text{Li}/\text{H} = (2.29 \pm 0.94) \times 10^{-10}$ [73]. Both sets of abundances are substantially lower than the standard BBN prediction of ${}^7\text{Li}$ based on the WMAP estimate of η [1], by factors of $\sim 2.4 - 4.3$, or $4 - 5\sigma$ [6]. This discrepancy is known as the “lithium problem” or more specifically the “ ${}^7\text{Li}$ problem.” In our later analysis, we adopt ${}^7\text{Li}/\text{H} < 2.75 \times 10^{-10}$ as our fiducial upper limit on the cosmological ${}^7\text{Li}$ abundance.

The existence of the ${}^7\text{Li}$ problem, and the nature of its solution, both have a direct impact on our analysis. It is possible that the problem points to new physics, in particular if the observations and standard theory are both correct with accurate error estimates. If SUSY were to lead to a solution of the ${}^7\text{Li}$ problem, this would tie together a wide array of particle astrophysics experiments and observations. Indeed, it has been suggested [21, 22] that the ${}^7\text{Li}$ problem could be solved by hadronic decays of a metastable neutral particle X with lifetime $\tau_X \sim 10^3$ sec. We will directly address and update this issue below. On the other hand, it remains possible that the standard BBN light-element abundance predictions

remain correct, i.e., unperturbed by any dark matter interactions and/or decays. Rather, it could be that the ${}^7\text{Li}$ problem instead reflects astronomical observational systematics in recovering a Li/H abundance from stellar spectra, though a recent study [74] of the effective temperature of metal poor stars confirmed the use of relatively low temperatures and a Li abundance in the range $\text{Li}/\text{H} = (1.3 - 1.4 \pm 0.2) \times 10^{-10}$. The ${}^7\text{Li}$ problem may also reflect astrophysical systematics due to Li depletion via circulation and nuclear burning over the > 10 Gyr lifetime of metal-poor stars [75], though the lack of star-to-star scatter in Li/H suggests the depletion could be negligibly small [69]. If there is depletion, for our problem the correct procedure would be to use the initial, undepleted Li/H abundances. However, since these cannot be determined accurately, we do not adopt a quantitative constraint for this possibility. Instead, we consider the limits on unstable particles when the ${}^7\text{Li}$ is assumed to be solved and thus the ${}^7\text{Li}$ constraints are ignored.

Recent work has claimed to resolve lithium isotope information in halo stars [76, 77], and indicates the presence of ${}^6\text{Li}$. In fact, the isotopic ratio has a roughly constant value of

$$\frac{{}^6\text{Li}}{{}^7\text{Li}} \approx 0.05. \quad (6)$$

This has several immediate implications. First, we see that most of the lithium is in the form of ${}^7\text{Li}$, so that the total elemental lithium abundance (as in eqs. (4) and (5)) is mainly ${}^7\text{Li}$: $\text{Li}/\text{H} \approx {}^7\text{Li}/\text{H}$. Secondly, given that Li/H in these stars has a plateau, the constancy of the isotopic ratio implies that both isotopes have a plateau. However, the inferred ${}^6\text{Li}$ plateau abundance is about 1000 times the ${}^6\text{Li}$ abundance predicted by standard BBN [78, 79].

Extracting isotopic information from thermally broadened absorption lines is extremely challenging, and the existence of a ${}^6\text{Li}$ plateau has been questioned [80]. If real, the ${}^6\text{Li}$ plateau abundance cannot be explained by conventional Galactic cosmic-ray nucleosynthesis [79, 81, 82]. Therefore, one is led to think that there is a “ ${}^6\text{Li}$ problem” in addition to that for ${}^7\text{Li}$.

It is possible to arrange decaying-particle scenarios in which ${}^6\text{Li}$ is produced at the plateau level with some destruction of ${}^7\text{Li}$, thus fixing both lithium problems simultaneously [26, 29, 83–86], a point to which we will return in detail below. However, even granting the existence of the ${}^6\text{Li}$ plateau, the ${}^6\text{Li}$ problem really only requires a pre-Galactic source, which need not arise prior to the first star formation. For example, the ${}^6\text{Li}$ problem might be explained by cosmological cosmic-ray nucleosynthesis due to cosmic rays produced at the epoch of structure formation [87]. For our purposes, therefore, we simply interpret eq. (6) as a firm upper limit on any primordial ${}^6\text{Li}$ [77, 80].

2.2 Baryon Density

The baryon-to-photon ratio $\eta \equiv n_{\text{B}}/n_{\gamma} \equiv 10^{-10}\eta_{10}$ is related to the present baryon density parameter $\Omega_{\text{B}} = \rho_{\text{B}}/\rho_{\text{crit}}$ by $\Omega_{\text{B}}h^2 = \eta_{10}/274$. Adopting the value of $\Omega_{\text{B}}h^2$ indicated by the WMAP 5-year CMB data [1] gives the following estimate of the baryon-to-photon ratio:

$$\eta_{10} = 6.23 \pm 0.17. \quad (7)$$

This is the default value we assume later in our BBN analysis. The central value and error range here correspond to WMAP data combined with large-scale structure information, in a framework for which the primordial power spectrum is a simple power law with fixed index. Similar but slightly different values would result from, e.g., a running spectral index.

3 Hadronic Decays during Primordial Nucleosynthesis

Particle decays during BBN generally have two main effects [7, 31]. First, they change the cosmic expansion rate due to the injection of additional relativistic species. This effect is model-independent, in that it is insensitive to the details of the decays, beyond the assumption that the daughter particles are relativistic [10]. Secondly, they introduce new, non-thermal decay products—possibly electromagnetic and/or hadronic—which can interact with the background thermal nuclei and change the final light-element abundances. The branching ratios and spectra of hadronic and electromagnetic decay particles and energies are model-dependent, and are further discussed below in Section 4. While both effects occur in principle, the expansion effects are negligible for the decay parameters of practical interest to us, and the non-thermal interaction effects are the dominant perturbations to the abundances. Consequently, we focus on these effects, and henceforth neglect the perturbation to the expansion rate. If the decaying particles are electrically charged and thus can form bound states with nuclei, additional effects arise [29, 83–86, 88–96]. This is not the case in the scenarios considered in the present paper, but we will revisit this subject in future work.

To fix notation: we consider decays of some generic heavy particle X , which we will eventually specialize to the case of the gravitino. The particle has lifetime τ_X and decay rate $\Gamma_X = \tau_X^{-1}$. We can quantify the X abundance either as the number of decaying particles per background baryon,

$$Y_X \equiv \frac{n_X}{n_{\text{B}}}, \quad (8)$$

or as the number of particles per unit entropy

$$y_X = \frac{n_X}{s} = Y_X \frac{n_{\text{B}}}{s} \approx \frac{1}{7}\eta Y_X, \quad (9)$$

where $s \simeq 7n_\gamma$ is the entropy density, and the factor of $\simeq 7$ is appropriate after e^\pm annihilation. We note that, in the absence of X decays, conservation of baryon number guarantees the constancy of Y_X , while y_X changes during BBN due to the usual photon heating from e^\pm annihilation. Due to decays, we have $Y_X(t) = Y_X^{\text{init}} e^{-t/\tau_X}$; our constraints will be on the initial, pre-decay abundance Y_X^{init} , and this should be understood hereafter whenever we write Y_X . The only exception in our notation is that we write Y_p for the ${}^4\text{He}$ mass fraction and this should not be confused with the ratio of number densities as defined in eq. (8).

We are interested in both hadronic and electromagnetic decays of the heavy particles X . We denote the electromagnetic branching ratio of X by $B_{\text{EM}} = \Gamma_{X \rightarrow \text{EM}}/\Gamma_X$. The abundance perturbations from electromagnetic decays, and thus the constraints on such decay modes, scale with the product of B_{EM} and the decay energy release per photon:

$$\zeta_X \equiv \frac{m_X n_X}{n_\gamma} = m_X Y_X \eta, \quad (10)$$

where the X abundance is evaluated prior to decay. As emphasized particularly by [22], electromagnetic decays inevitably accompany hadronic decays, and so both sets of decay products and interactions need to be included. Electromagnetic decays were discussed in detail in [29]; we include those processes here, incorporating the treatment described in [29]. However, the analysis there assumed that the electromagnetic decays occurred entirely after the usual BBN thermonuclear reactions have run to completion, i.e., the decays were treated as a “post-processing” modification after the usual light-element abundances had been established. Here, we supplement the previous treatment by including electromagnetic decay effects consistently throughout BBN.

We quantify generic decays $X \rightarrow h$ of a particle X into a hadronic species h as follows. We write the h production rate per unit volume, and daughter kinetic energy ϵ as $q_h(\epsilon)$. The total X decay rate per baryon is $\Gamma_X Y_X$ and the total X decay rate per volume is $q_{X,\text{tot}} = \Gamma_X Y_X n_B$. It will be convenient to isolate the h production per X decay as $Q_h(\epsilon) = q_h(\epsilon)/q_{X,\text{tot}}$, so that we have

$$q_h(\epsilon) \equiv \Gamma_X Y_X n_B Q_h(\epsilon). \quad (11)$$

We refer to $Q_h(\epsilon)$ as the spectrum of X decays, which gives the number of h particles produced per X decay per energy interval. The integral $B_h \equiv \int Q_h(\epsilon) d\epsilon$ gives the total number of h per X decay, and thus represents a multiplicity-weighted hadronic branching ratio. Gravitino decays are described in detail in the next Section.

3.1 Interactions with Background Nuclides

The dominant effect of hadronic decays on BBN is the addition of new interactions between hadronic shower particles and background nuclides. These act to alter the evolution and final values of the light-element abundances, as follows. For each light nuclide ℓ , the abundance per background baryon, $Y_\ell \equiv n_\ell/n_B$, changes according to

$$\partial_t Y_\ell = (\partial_t Y_\ell)_{\text{SBBN}} + (\partial_t Y_\ell)_{\text{EM}} + (\partial_t Y_\ell)_{\text{had}}, \quad (12)$$

where $(\partial_t Y_\ell)_{\text{SBBN}}$ denotes the usual rate of change of ℓ in standard BBN due to thermonuclear reactions. The second term on the right-hand side of (12) accounts for non-thermal electromagnetic interactions due to X decays, either directly from the decays of X to photons or leptons, or through electromagnetic secondaries in the hadronic showers. These are treated as in [20], but are not dominant when hadronic branchings are significant. The final term on the right-hand side of (12) represents the non-thermal hadronic interactions, which are a major focus of this paper.

The inclusion of hadronic decays in BBN thus requires a detailed evaluation of the rates for such interactions. For each background light nuclide species ℓ , we can write the hadronic contributions to $\partial_t Y_\ell$ as

$$(\partial_t Y_\ell)_{\text{had}} = -\Gamma_{\ell \rightarrow \text{inel}} Y_\ell + \sum_{hb} \Gamma_{hb \rightarrow \ell} Y_b. \quad (13)$$

The first term accounts for ℓ destruction by hadro-dissociation, where $\Gamma_{\ell \rightarrow \text{inel}}$ is the total rate (per unit of the species ℓ) of all inelastic interactions of shower particles with ℓ . The second term accounts for production due to hadro-dissociation of heavier background species (e.g., deuteron production via helium erosion $p_{\text{shower}} \alpha_{\text{bg}} \rightarrow d + \dots$). The sum of inelastic rates $\Gamma_{hb \rightarrow \ell}$ producing ℓ runs over shower species h and background targets b . In the particular case of lithium isotopes, production occurs via the interaction of energetic (i.e., non-thermal) mass-3 dissociation products with background ${}^4\text{He}$, e.g., ${}^3\text{He} + \alpha \rightarrow {}^{6,7}\text{Li} + \dots$.

The non-thermal reaction rates on light elements are themselves set by the abundance and energy distribution of non-thermal particles, which we quantify as follows. Consider a hadronic (non-thermal projectile) species h , with an energy spectrum $\frac{dn_h}{d\epsilon}(\epsilon, t)$ (particle number per unit volume per unit energy interval) and total number density $n_h = \int \frac{dn_h}{d\epsilon} d\epsilon$. It is convenient to define the energy spectrum of non-thermal h as $N_h \equiv \frac{dn_h}{d\epsilon}/n_X$, which is normalized such that $\int N_h(\epsilon) d\epsilon = n_h/n_X = n_h/Y_X n_B$ measures the number of propagated non-thermal h particles per X .

The rate for non-thermal production of species ℓ due to $hb \rightarrow \ell$ is

$$\Gamma_{hb \rightarrow \ell} = Y_X n_B \int N_h(\epsilon, t) \sigma_{hb \rightarrow \ell}(\epsilon) v_{\text{rel}}(\epsilon) d\epsilon \approx Y_X n_B \int N_h(\epsilon, t) [\sigma_{hb \rightarrow \ell} v](\epsilon) d\epsilon, \quad (14)$$

where $\sigma_{hb \rightarrow \ell}(\epsilon)$ is the cross section for this process. Here $v_{\text{rel}}(\epsilon) \approx v_h(\epsilon)$ is the relative velocity between the projectile and the background target, which in practice amounts to the projectile velocity. In a similar way, the inelastic-loss rate is just a sum over all inelastic channels removing ℓ , i.e., where the final state f does not include ℓ :

$$\Gamma_{\ell \rightarrow \text{inel}} \approx Y_X n_B \sum_f \int N_h(\epsilon, t) [\sigma_{h\ell \rightarrow f} v](\epsilon) d\epsilon. \quad (15)$$

The rates Γ_ℓ thus depend on the shower development and evolution of $N_h(\epsilon, t)$ in the background environment. A major effort of this paper is to calculate these spectra and their evolution.

3.2 Hadronic Showers

We wish to follow the evolution of the non-thermal spectra N_h over the multiple generations produced by the hadronic X decays. In the context of BBN, this problem of shower development has been approached via Monte Carlo computation of the multiple generations of shower particles [18, 19, 21, 22]. The final particle spectrum is obtained via iterating an initial decay spectrum, accounting for both energy losses as well as the energy distribution of collision products.

Here we introduce an alternative, but equivalent, approach based on a ‘‘cascade equation’’ treatment, that follows the well-studied treatment of the development of hadronic showers due to cosmic-ray interactions in the atmosphere. As we show, this approach offers new physical insight as well as computational advantages.

Once a hadron h is produced by X decay, it loses energy, interacts with background nuclei, and possibly decays if it is unstable (e.g., n, π^\pm). The spectrum of h evolves according to the energy-space ‘‘propagation equation’’:

$$\partial_t N_h(\epsilon) = J_h(\epsilon) - \Gamma_h(\epsilon) N_h(\epsilon) - \partial_\epsilon [b_h(\epsilon) N_h(\epsilon)], \quad (16)$$

where J_h is the sum of all source terms, Γ_h is the sum of all sink terms, and b_h is the energy-loss rate of particle-conserving processes. Note that inelastic interactions lead to secondary production of h , sometimes by other non-thermal species h' . For this reason, eq. (16) ultimately represents a set of coupled, integro-differential equations.

Details of eq. (16) and its numerical solution appear in Appendix A. In the next section, we summarize the key physics via an analytical description informed by the full numerical results.

3.3 Non-Thermalized Particle Spectra and Interactions: Analytical Model

To develop a physical intuition for the full numerical results used later, we first present a simplified analytical treatment of the propagation and interactions of non-thermalized hadrons.

A crucial feature of eq. (16) is that it contains both source and sink terms for h . The rates for energy loss in the cosmic plasma, and for scattering on the background nuclei, are always faster than the cosmic expansion rate H . Thus, redshift and expansion effects may safely be ignored in non-thermal particle propagation, and have been neglected in eq. (16). Moreover, the energy-loss and scattering rates are generally faster than the non-thermal source rate $\Gamma_X = 1/\tau_X$ set by the X decay time. Thus eq. (16) is *self-regulating*, with N_h tracking a quasi-static equilibrium set by the balance of source and sink terms. That is, at any cosmic epoch we have $\partial_t N_h(\epsilon) \approx 0$. This provides a crucial simplification and reduces the problem to a series of ordinary integro-differential equations, which one may solve at each epoch.

We thus begin with a simplified version of the full propagation equation, which neglects elastic and inelastic source terms:

$$0 = -\partial_\epsilon(b_h N_h) - (\Gamma_{h,sc} + \Gamma_\beta)N_h + \Gamma_X Q_h, \quad (17)$$

where $b_h = -d\epsilon_h/dt$ is the total energy-loss rate, and $\Gamma_{h,sc}$ is the total rate for inelastic and elastic scattering. For neutrons, $\Gamma_\beta = 1/\gamma_n \tau_n$ is the rate for the beta decay of a free neutron with Lorentz factor γ_n ; for protons $\Gamma_\beta = 0$.

Equation (17) is formally identical to the “leaky box” equation for the propagation of cosmic rays in our Galaxy. Indeed, our problem can be regarded as the injection of cosmic rays in the early universe plasma. The solutions to eq. (17) have been well-studied for the case of Galactic cosmic rays [97], and we adapt the solutions for our problem. We focus on the propagation of the primary species, i.e., the p and n , which have sources in the X decays themselves; in this case the decay term dominates the sources. Our full numerical treatment also includes primary π^\pm , but these are important only for short $\tau_X \lesssim 1$ sec.

On physical grounds, we expect that the hadronic spectra N_h at any given time should scale linearly with the X decay rate Γ_X . One can infer this formally from eq. (16), as outlined

in Appendix A. Thus we have the scaling $N_h \propto \Gamma_X$, and so the ratio N_h/Γ_X is independent of the decay rate Γ_X .

If we ignore secondary production of h , the exact solution to eq. (17) is known and appears in Appendix A. However, for our purposes it is useful to focus on two limiting cases. Generally, one of the sink terms is dominant and controls the resulting equilibrium. If the scattering term dominates the energy-loss term, $\Gamma N \gg \partial_\epsilon(bN)$ we refer to this as the *thin-target* limit. Physically, h particles interact catastrophically before they lose energy, i.e., the cosmic plasma is “thin” against stopping. The reverse case, $\Gamma N \ll \partial_\epsilon(bN)$, constitutes the *thick-target* limit, where particles lose energy before interacting. We can express the ratio of the two terms as $\partial_\epsilon(bN)/\Gamma N = (b/\epsilon\Gamma)\partial \ln(bN)/\partial \ln \epsilon$. We see that, as long as the logarithmic term is slowly varying, the dominant loss term is set by a comparison of scattering timescale Γ^{-1} with energy-loss timescale ϵ/b :

$$\Gamma_{\text{sc}} \gg \frac{b}{\epsilon} \Rightarrow \text{thin target}, \quad (18)$$

$$\Gamma_{\text{sc}} \ll \frac{b}{\epsilon} \Rightarrow \text{thick target}. \quad (19)$$

In the thin-target limit, scattering losses dominate, so that eq. (17) reduces to $-\Gamma_{h,\text{sc}}N_h + \Gamma_X Q_h \simeq 0$ and the solution becomes algebraic

$$N_h(\epsilon) \simeq \Gamma_X \frac{Q_h(\epsilon)}{\Gamma_{h,\text{sc}}(\epsilon)} = \Gamma_X \frac{Q_h(\epsilon)}{n_B Y_b v \sigma_{hb \rightarrow \text{inel}}(\epsilon)}. \quad (20)$$

Here the reaction on background species b dominates the scattering losses. Note the inverse scaling with baryon density n_B . Note also that we have implicitly assumed $\Gamma_\beta \ll \Gamma_{\text{sc}}$. In the case of neutrons, once $\Gamma_\beta > \Gamma_{\text{inel}}$ (which is indeed well into the thin-target regime), then neutrons decay before they interact. This occurs when $\Gamma_{\text{inel},n} \sim n_B v_n \sigma_{\text{inel}} < \Gamma_\beta$, which corresponds to $T \lesssim 0.4 \text{ keV } \gamma_n^{-1/3} (v_n/0.1c)^{-1/3}$ and $t \gtrsim 8 \times 10^6 \text{ s } \gamma_n^{2/3} (v_n/0.1c)^{2/3}$. At longer times, non-thermal protons and, more importantly, electromagnetic cascades, dominate light-element production.

Turning now to the thick-target limit, when energy losses dominate the sinks we have $0 \simeq -\partial_\epsilon(bN_h) + \Gamma_X Q_h$, and thus

$$N_h(\epsilon) \simeq \Gamma_X \frac{Q_h(> \epsilon)}{b(\epsilon)}, \quad (21)$$

where $Q_h(> \epsilon) = \int_\epsilon Q_h(\epsilon') d\epsilon'$ is the integral source spectrum above ϵ . Taking $b = b_{\text{coul}}$ for Coulomb losses, we have $b \sim 4\pi\alpha^2 \hbar^2 c^2 Y_{e^\pm} n_B / m_e v$, or

$$d\epsilon/dR = b/\rho_B v \sim 4\pi\alpha^2 \hbar^2 c^2 Y_{e^\pm} / m_e m_p v^2 \sim 1.5 \text{ MeV} / (\text{gcm}^{-2}) Y_{e^\pm} (100 \text{ MeV} / \epsilon). \quad (22)$$

Crucially, the electron/positron abundance Y_{e^\pm} per baryon is enormous before pair annihilation, so that $Y_{e^\pm} \sim 1/\eta \sim 10^9$ at $T \gtrsim 0.2$ MeV, and even afterwards the pairs dominate the baryons until $T \sim m_e/25 \sim 0.02$ MeV. Thus we write

$$N_h(\epsilon) \simeq \Gamma_X \frac{Q_h(> \epsilon)}{m_p n_B v(\epsilon) d\epsilon_h/dR(\epsilon)}, \quad (23)$$

where we use the energy loss per grammage $d\epsilon/dR = b/\rho_B v$, which is independent of background density. Here again we see that the spectrum scales inversely with background density, but also has an inverse dependence on the strongly-varying electron/positron abundance Y_{e^\pm} , contained in $d\epsilon/dR$.

3.4 Non-thermal Reaction Rates

Consider a reaction $hb \rightarrow \ell$ on a light background species b which produces a daughter species ℓ , e.g., $n\alpha \rightarrow d + \dots$. The rate for this reaction is

$$\Gamma_{hb \rightarrow \ell} = \int \phi_h(\epsilon) \sigma_{hb \rightarrow \ell}(\epsilon) d\epsilon \quad (24)$$

per background target b . Here the (angle-integrated) flux of non-thermal $h \in n, p$ is $\phi_h(\epsilon) = n_X N_h(\epsilon) v(\epsilon) = Y_X n_B N_h(\epsilon) v(\epsilon)$. Recalling that $N_h \propto 1/n_B$, we see that the non-thermal flux $\phi_h \propto n_B N_h$ and thus the reaction rate $\Gamma_{hb \rightarrow \ell}$ are both independent of the background baryon density. Also, since $N_h \propto \Gamma_X$, we have $\Gamma_{hb \rightarrow \ell} \propto \Gamma_X Y_X$.

We now examine the reaction rate for the two limiting cases of propagation. Using N_h in the two limits, we have

$$\Gamma_{hb \rightarrow \ell} = \begin{cases} \Gamma_X \frac{Y_X}{Y_k^{\text{bg}}} \int_{\epsilon_{\text{th}}} Q_h(\epsilon) \frac{\sigma_{hb \rightarrow \ell}(\epsilon)}{\sigma_{hk \rightarrow \text{inel}}} d\epsilon & \text{thin target,} \\ \Gamma_X Y_X \int_{\epsilon_{\text{th}}} Q_h(> \epsilon) \frac{\sigma_{hb \rightarrow \ell}(\epsilon)/m_p}{d\epsilon_h/dR} d\epsilon & \text{thick target,} \end{cases} \quad (25)$$

where the integral begins at the threshold energy ϵ_{th} (if any). Here we take the interaction $hk \rightarrow \text{inelastic}$ of the non-thermal particle h with background nuclide k to dominate the inelastic losses.

With these reaction rates in hand, we illustrate their importance by estimating below the perturbation on light-element abundances that arises in the CMSSM with a massive gravitino. Before doing this, we must first have an understanding of the gravitino decays and the resulting hadronic spectra.

4 Gravitino Decays

We work in the context of the CMSSM [46] which is described by four parameters: universal gaugino, scalar, and trilinear masses, $m_{1/2}, m_0, A_0$, and the ratio of the two Higgs vacuum expectation values, $\tan\beta$, along with the sign of the Higgs mixing parameter, μ . Motivated by $g_\mu - 2$ and $b \rightarrow s\gamma$, we restrict our attention to $\mu > 0$ and, for simplicity, we consider only $A_0 = 0$. We consider scenarios in which the lightest neutralino is the LSP, but the gravitino is not assumed necessarily to be the NLSP. For fixed values of $\tan\beta$, the regions of parameter space for which the relic density of neutralinos is computed to lie within the range $0.0975 < \Omega_{\text{CDM}} h^2 < 0.1223$ determined by WMAP [1] and other observations for cold dark matter form narrow strips that foliate the $(m_{1/2}, m_0)$ plane [45, 47]. These strips correspond to regions where there are enhanced annihilation cross sections that reduce the neutralino relic density to acceptable values. These strips occur when the neutralino is nearly degenerate with some other supersymmetric particle such as the partner of the tau lepton (coannihilation strip), when the neutrino is close to half the mass of the heavy Higgs scalar and pseudoscalar boson so that rapid s-channel annihilation occurs (the funnel region), or at large values of m_0 when the renormalization-group evolution drives the value of μ to low values so that the neutralino acquires a significant Higgsino component and new final-state channels become important (the focus-point strip). Our analysis is based on the WMAP strips for two representative values of $\tan\beta = 10, 50$. For $\tan\beta = 10$ one strip follows the coannihilation corridor, and for $\tan\beta = 50$ this strip also includes the funnel at larger values of $m_{1/2}$. We also consider the focus-point strips for both values of $\tan\beta$.

In the scenario under study the gravitino decays into lighter sparticles, including the neutralino LSP but also others in general. We take into account all the dominant decay channels of the gravitino into (s)particles, including the complete set of two-body decays of the gravitino into Standard Model particles and their spartners. These fall into the following main categories: $\tilde{G} \rightarrow \tilde{f} f$, $\tilde{G} \rightarrow \tilde{\chi}^+ W^-(H^-)$, $\tilde{G} \rightarrow \tilde{\chi}_i^0 \gamma(Z)$, $\tilde{G} \rightarrow \tilde{\chi}_i^0 H_i^0$ and $\tilde{G} \rightarrow \tilde{g} g$. Analytical expressions for these amplitudes can be found in Appendix B. In addition, we include the dominant three-body decays $\tilde{G} \rightarrow \tilde{\chi}_i^0 \gamma^* \rightarrow \tilde{\chi}_i^0 q\bar{q}$, $\tilde{G} \rightarrow \tilde{\chi}_i^0 W^+ W^-$, which are also discussed in Appendix B. In principle, one should also include $q\bar{q}$ pair production through the virtual Z -boson channel $\tilde{G} \rightarrow \tilde{\chi}_i^0 Z^* \rightarrow \tilde{\chi}_i^0 q\bar{q}$ [24] and the corresponding interference term. However, this process is suppressed by a factor of M_Z^4 with respect to $\tilde{G} \rightarrow \tilde{\chi}_i^0 \gamma^* \rightarrow \tilde{\chi}_i^0 q\bar{q}$, and the interference term is also suppressed by M_Z^2 . These contributions are therefore not very important, and we drop these amplitudes in our calculation. We also drop the corresponding amplitudes for Higgs and squark exchange. We calculate the lifetime of the gravitino by first

calculating the partial widths of its dominant relevant decay channels, and then summing them. Typical results are shown in Fig. 1, where we see that the lifetimes for $\tan\beta = 50$ (right panels) are typically longer than those for $\tan\beta = 10$ (left panels), particularly for larger $m_{1/2}$. On the other hand, the lifetimes in the coannihilation/funnel regions (top panels) are quite similar to those in the focus-point regions (bottom panels).

In order to calculate the resulting electromagnetic (EM) and hadronic (HD) spectra, we first calculate the EM and HD decay spectra of the different gravitino decay modes, and then weight them by the corresponding branching ratios. The decay products that yield EM energy obviously include directly-produced photons, but also indirectly-produced photons, charged leptons (electrons and muons) and neutral pions (π^0), which are produced via the secondary decays of unstable heavy particles such as gauge and Higgs bosons. Hadrons (nucleons and mesons such as the K_L^0 , K^\pm and π^\pm) are also usually produced through the secondary decays of heavy particles, as well as (for the mesons) via the decays of the heavy τ lepton. It is important to note that strange mesons and neutral pions decay before interacting with the hadronic background [19, 41, 42]. Hence they are relevant to BBN processes and to our analysis only via their decays into photons and charged leptons, which contribute to the EM component of the decay showers. Therefore, the HD injections that concern us are those that produce nucleons, via the decays of heavy particles such as gauge and Higgs bosons and quark-antiquark pairs and to a lesser extent charged pions.

After calculating the partial decay widths and branching ratios, we then employ the PYTHIA event generator [98] to model both the EM and the HD decays of the direct products of the gravitino decays. We first generate a sufficient number of spectra for the secondary decays of the gauge and Higgs bosons and the quark pairs. Then, we perform fits to obtain the relation between the injected energy of the decaying particle, that we call E_{inj} , and the quantity that characterizes the hadronic spectrum, namely Q_h , the number of produced nucleons as a function of the nucleon energy, for various values of the E_{inj} . We have performed fits that cover the range $200 \text{ GeV} < E_{inj} < 20 \text{ TeV}$. In Table 1 we present a representative set of fitting parameters for $E_{inj} = 1000 \text{ GeV}$. Then, using the equation

$$Q_h(\epsilon_h) = \frac{\epsilon_h}{E_{inj}^2} \frac{1}{x} \tilde{Q}_h(x), \quad (26)$$

the spectrum distribution $Q_h(\epsilon_h)$ is computed using the function $\tilde{Q}_h(x) = Q_h(\epsilon_h)d\epsilon_h/dx$, with $x = \sqrt{\epsilon_h^2 - m_h^2}/E_{inj}$. Some typical spectra for gravitino decays into protons are shown in Fig. 2. These spectra and the fraction of the energy of the decaying particle that is injected as EM energy are then used to calculate the light-element abundances. We stress that this procedure is repeated separately for each point sampled in the supersymmetric

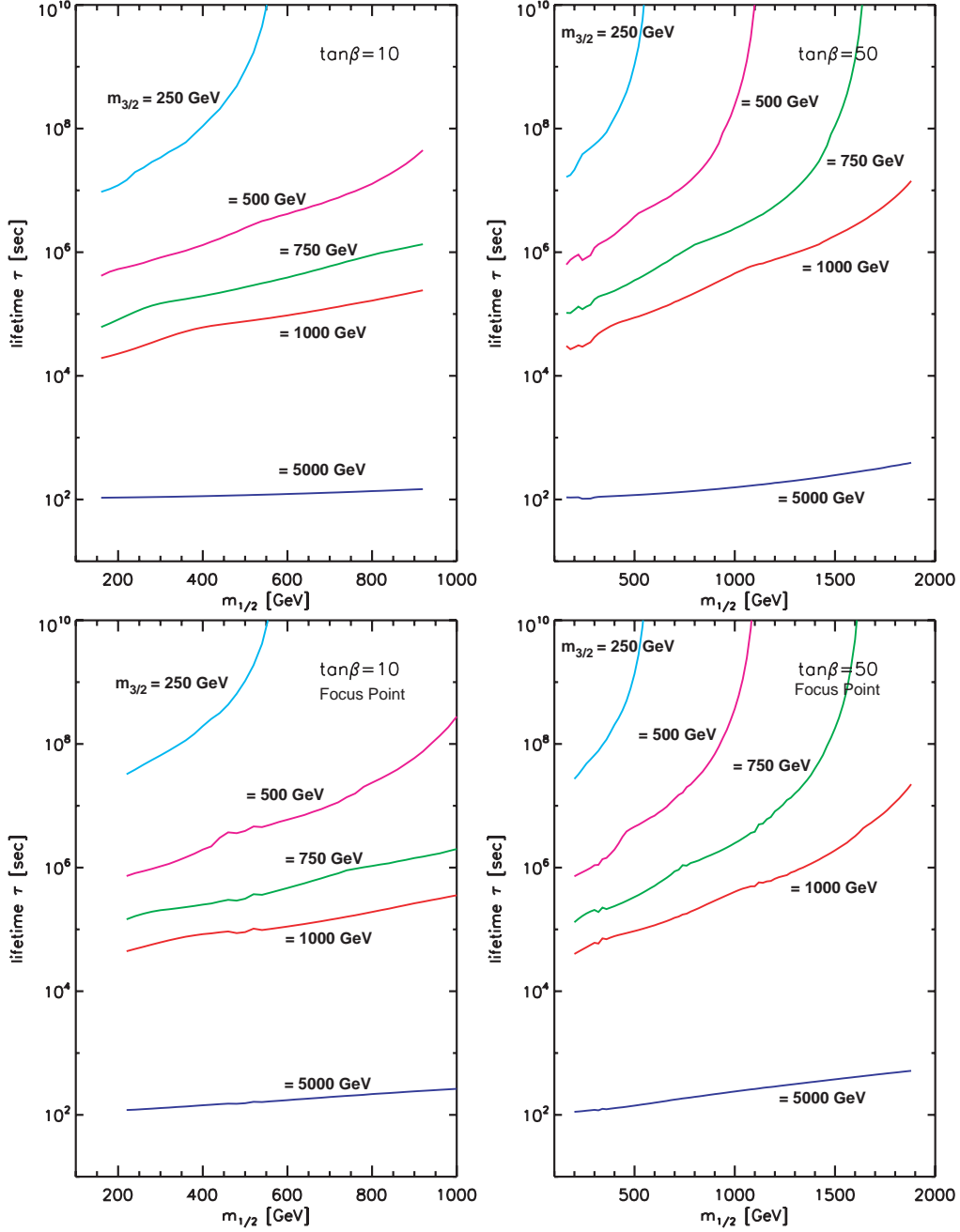


Figure 1: *The gravitino lifetime for representative values of $m_{3/2}$ as a function of $m_{1/2}$ for $\tan\beta = 10$ (left) and $\tan\beta = 50$ (right) along WMAP strips, in the coannihilation and funnel region (top) and the focus-point region (below).*

parameter space. That is, given a set of parameters $m_0, m_{1/2}, A_0, \tan\beta, \text{sgn}(\mu)$, and $m_{3/2}$, after determining the sparticle spectrum, all of the relevant branching fractions are computed,

and the hadronic spectra and the injected EM energy determined case by case. Thus, in our analysis, Q_p (Q_n) and hence the total number of protons (neutrons) per gravitino decay, B_p (B_n), varies between different points in the parameter space, and Fig. 3 illustrates this variation in B_p (and B_n) across the supersymmetric parameter space we sample.

Table 1: *The values of the parameters A , B , C , D and E used in fitting PYTHIA hadronic decay spectra. We use the function $Y \equiv \log_{10}(\tilde{Q}(x))$ parametrized via $Y = AX^4 + BX^3 + CX^2 + DX + E$, where $X \equiv \log_{10}(x)$, and the scaling parameter x is defined as $x = \sqrt{\epsilon_h^2 - m_h^2}/E_{inj}$. The values of this table correspond to $E_{inj} = 1$ TeV.*

decaying particles	inj. species	A	B	C	D	E
Z	p	0.000	0.000	-1.230	-4.823	-3.401
	n	0.000	0.000	-1.281	-4.917	-3.418
h	p	0.000	0.000	-1.011	-4.302	-3.071
	n	0.000	0.000	-0.850	-3.628	-2.499
H	p	0.000	0.000	-0.647	-3.398	-2.154
	n	0.000	0.000	-0.644	-3.414	-2.230
A	p	0.000	0.000	-0.633	-3.356	-2.133
	n	0.000	0.000	-0.637	-3.377	-2.179
$q\bar{q}$	p	-0.065	-0.551	-2.007	-4.326	-2.602
	n	-0.033	-0.195	-0.603	-2.039	-1.327
$W^+ W^-$	p	0.000	0.000	-1.146	-5.180	-4.036
	n	0.000	0.000	-1.107	-4.936	-3.742

The relative sizes of the gravitino partial widths and the locations of the various particle thresholds help us to understand the lifetime and the hadronic spectra curves. In general, the two-body channels $\tilde{G} \rightarrow \tilde{\chi}_i^0 \gamma$; $\tilde{f} f$; $\tilde{g} g$; $\tilde{\chi}^+ W^-$ dominate the \tilde{G} decays. In particular, the decay to $\tilde{\chi}_i^0 \gamma$ yields the bulk of the injected EM energy. However, the decays to sfermions, gluinos and charginos become of the same order of magnitude as the $\tilde{G} \rightarrow \tilde{\chi}_i^0 \gamma$ channel whenever they are kinematically possible. Also, when the \tilde{G} is heavy enough to decay into a real Z boson, the channel $\tilde{G} \rightarrow \tilde{\chi}_i^0 Z$ is the dominant channel for producing HD injections. When kinematically allowed, $\tilde{G} \rightarrow \tilde{\chi}^+ W^-$ and $\tilde{G} \rightarrow \tilde{g} g$ are also important in producing HD injections. The Higgs boson channels are smaller by a few orders of magnitude (due to couplings and kinematics) and, in particular, in the large- $m_{1/2}$ region, decays to heavy Higgs bosons (H , A) become kinematically accessible only for heavy \tilde{G} and are unimportant otherwise.

Turning to the three-body channels, the decay through the virtual photon to a $q\bar{q}$ pair

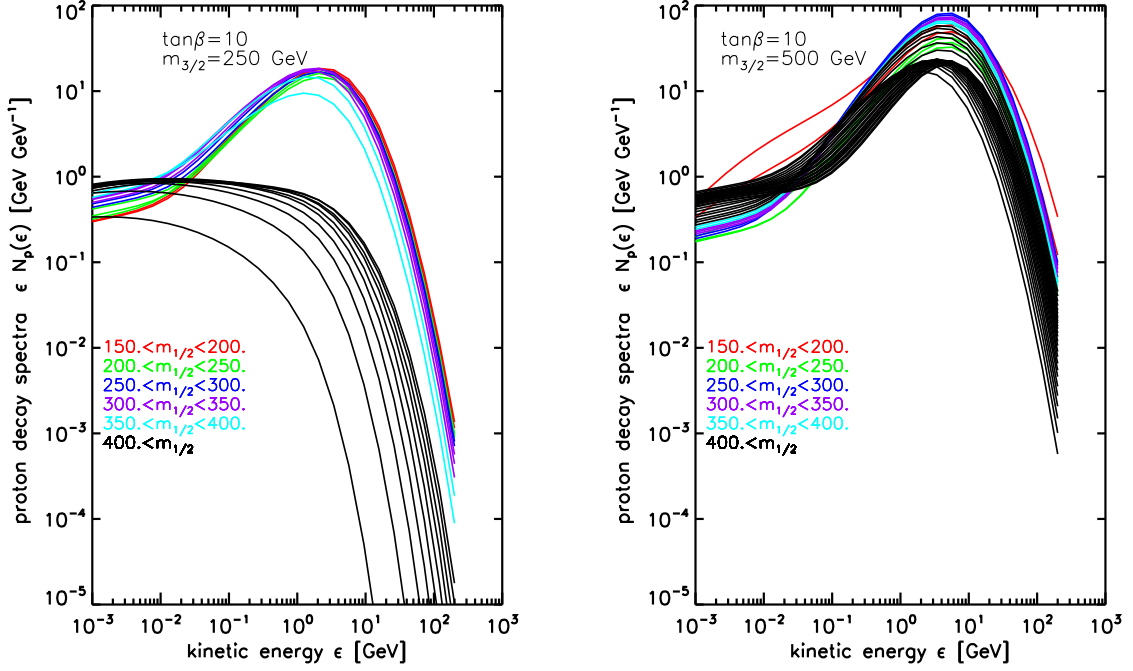


Figure 2: *Sample spectra for gravitino decays into protons. We plot values of the combination $\epsilon N_p(\epsilon)$, which gives the particle number per logarithmic energy range, for different representative values of the gaugino mass parameter $m_{1/2}$ along the coannihilation strip for $\tan\beta = 10$, assuming the indicated values of the gravitino mass $m_{3/2}$.*

can become comparable to the channel $\tilde{G} \rightarrow \tilde{\chi}_i^0 Z$, injecting nucleons even in the kinematical region $m_{3/2} < m_\chi + M_Z$, where direct on-shell Z -boson production is not possible. Finally, we note that the partial width of the three-body decay $\tilde{G} \rightarrow \tilde{\chi}_i^0 W^+ W^-$ is usually smaller by at least an order of magnitude relative to the dominant two-body decays, except when this three-body decay exhibits resonant behavior. For example, the subprocess $\tilde{G} \rightarrow \tilde{\chi}^{+*} W^- \rightarrow \tilde{\chi}_i^0 W^+ W^-$ can lift the contribution of the $\tilde{\chi}_i^0 W^+ W^-$ channel to the level of the dominant two-body decays in the threshold region where the chargino can be produced on-shell.

With these observations in mind, one can understand the gravitino lifetime curves along the WMAP strips for $\tan\beta = 10$ and 50 in Fig. 1. We recall that the funnel region is only present in the CMSSM for large $\tan\beta$. Since the relation $m_\chi \approx m_A/2$ is realized at large $m_{1/2}$, the WMAP strip extends to significantly higher values of $m_{1/2}$ for $\tan\beta = 50$ than for $\tan\beta = 10$. In the latter case (upper left panel), the WMAP strip shown consists only of a coannihilation region, which terminates around $m_{1/2} = 900$ GeV. We notice that the

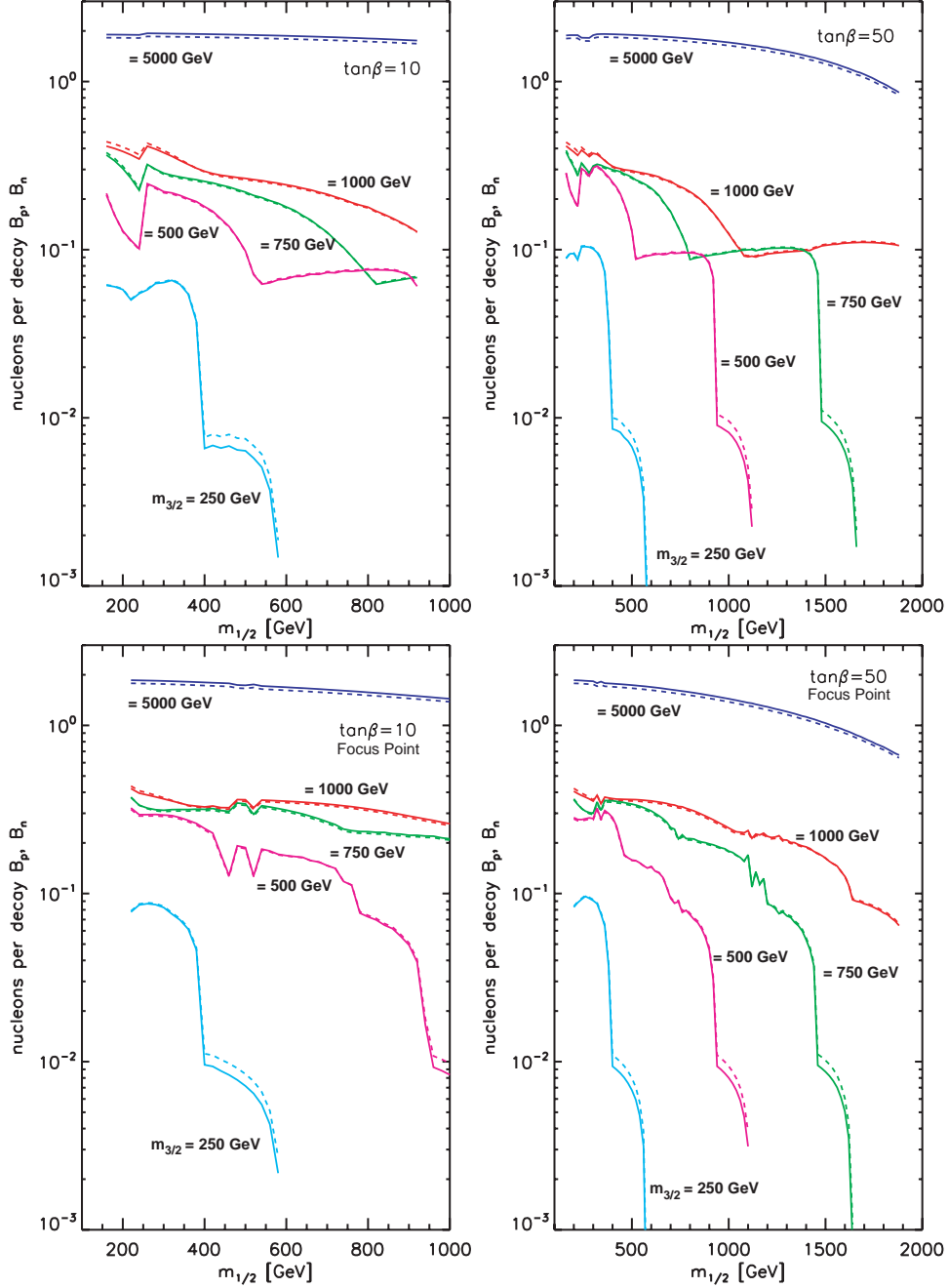


Figure 3: *The number of nucleons per gravitino decay, as a function of $m_{1/2}$ for $\tan\beta = 10$ (left) and $\tan\beta = 50$ (right). The upper panels are for WMAP strips in the coannihilation and rapid-annihilation regions, and the lower panels are for WMAP strips in the focus-point regions. Solid curves: number B_p of protons per decay. Broken curves: number B_n of neutrons per decay. We see that generally $B_p \approx B_n$ to a good approximation.*

gravitino lifetime is longer for $\tan\beta = 50$ than for $\tan\beta = 10$, for the same values of $m_{3/2}$ and $m_{1/2}$. Especially for the two upper panels, this is because for $\tan\beta = 50$ the WMAP strip, in the coannihilation region and (particularly) in the Higgs rapid-annihilation funnel region, occurs at larger m_0 and hence heavier squark and slepton masses, than in the $\tan\beta = 10$ case. This implies that the dominant two-body channels $\tilde{G} \rightarrow \tilde{f}f$ are very suppressed or even closed for $\tan\beta = 50$. Thus, the total gravitino decay width is smaller (and hence the lifetime longer) for $\tan\beta = 50$ than for $\tan\beta = 10$.

The lower panels in Fig. 1 correspond to the focus-point region. It is worth noticing that, unlike the coannihilation or the rapid-annihilation region, the focus-point strip extends to remarkably high values of m_0 and $m_{1/2}$. For example, for $\tan\beta = 50$ (lower right panel) $m_0 \sim 3$ TeV (5 TeV) at $m_{1/2} = 1000$ GeV (2000 GeV). As a result, the sfermion masses in this region are much larger than in the funnel or the coannihilation strip. Hence, for gravitino masses up to 1 TeV all the fermion-sfermion decay channels $\tilde{G} \rightarrow \tilde{f}f$ are closed, and the lifetime is larger than the upper panels. On the other hand, when $m_{3/2} = 5$ TeV the dominant decay channels $\tilde{g}g$, $\tilde{f}f$ and $\tilde{\chi}^+W^-$ are open along the WMAP strips also in the focus-point region, resulting in relatively flat lifetime curves as functions of $m_{1/2}$.

We note that for $m_{3/2} = 5$ TeV, the largest value shown, the gravitino lifetime $\sim \text{few} \times 10^2$ s in all the cases shown in in Fig. 1, which is comparable with the duration of BBN. Lighter gravitinos would decay after BBN is completed.

As $m_{1/2}$ increases for fixed $m_{3/2}$, the gaugino masses increase. Therefore, one by one the various gravitino decay channels are closed. The last to be closed are the two-body decay to $\tilde{\chi}_1^0\gamma$ and the three-body decay to light quark pairs $\tilde{\chi}_1^0q\bar{q}$. Eventually all the channels are closed when $m_{3/2} < m_\chi$. For $m_{3/2} = 250$ GeV this occurs for $m_{1/2} \sim 580$ GeV, as can be seen in Fig. 1. When the dominant channel for hadron production, $\tilde{\chi}_1^0Z$, closes we observe a significant decline in the nucleon spectra. This is the reason that in Fig. 3 in all the panels, for $m_{3/2} = 250$ GeV the value of B_p becomes smaller than 10^{-2} at $m_{1/2} = 400$ GeV, and the same at $m_{1/2} = 940$ GeV when $\tan\beta = 50$ and $m_{3/2} = 500$ GeV (right panels). Above these values of $m_{1/2}$, the only channel that produces some hadrons is $\tilde{G} \rightarrow \tilde{\chi}_1^0q\bar{q}$.

The importance of the channel $\tilde{G} \rightarrow \tilde{\chi}_i^0Z$ for producing nucleons can be seen in Fig. 2. There we plot the quantity $\epsilon N_p(\epsilon)$ for the case of protons for $\tan\beta = 10$ and $m_{3/2} = 250$ GeV (500 GeV) in the left (right) panel. The curves in these figures correspond to the various $m_{1/2}$ we sample along the WMAP coannihilation strip. The reason for the peaks in the GeV region is that the protons that are produced by on-shell hadronic decays of the Z boson have typical energies of a few GeV. As discussed earlier, for $\tan\beta = 10$ and $m_{3/2} = 250$ GeV the $\tilde{\chi}_i^0Z$ channel closes above $m_{1/2} = 400$ GeV. Therefore, we observe two

kinds of curves in Fig. 2 (left). These that peak in the GeV region are fed by the $\tilde{\chi}_1^0 Z$ channel, whereas these without the peak originate from the three-body channel $\tilde{\chi}_1^0 q\bar{q}$. For $\tan\beta = 10$ and $m_{3/2} = 500$ GeV, the decay $\tilde{G} \rightarrow \tilde{\chi}_1^0 Z$ is not closed anywhere along the WMAP strip, so all the curves in Fig. 2 (right) exhibit the Z -boson peak.

There are a few other features in Fig. 3 to be discussed. For $m_{1/2} \gtrsim 240$ GeV in the upper panels the lightest chargino can decay on-shell to $\tilde{\chi}_i^0 W^+$. The same happens in the lower left (right) panel for $m_{1/2} = 520$ GeV ($m_{1/2} = 360$ GeV). This causes a sudden increase in the number of the produced protons, that is more noticeable for $\tan\beta = 10$ (upper left panel), since there the relative importance of the decay channel $\tilde{G} \rightarrow \tilde{\chi}_1^{+*} W^- \rightarrow \tilde{\chi}_i^0 W^+ W^-$ is greater. This channel is closed for larger values of $m_{1/2}$ as the chargino becomes heavier, resulting in the shoulders we observe for $\tan\beta = 10$ (upper left panel) in the B_p curves at $m_{1/2} = 520$ GeV ($m_{3/2} = 500$ GeV) and $m_{1/2} = 800$ GeV ($m_{3/2} = 750$ GeV). The corresponding features appear also at the same points for $\tan\beta = 50$ in Fig. 3 (upper right panel). In the same figure, for $m_{3/2} \geq 500$ GeV, the additional wiggle seen at $m_{1/2} \sim 280$ GeV is due to the closing of the $\tilde{G} \rightarrow \tilde{\chi}_2^+ W^-$ channel. In the focus-point figures (lower panels), at $m_{1/2} = 400$ GeV and $m_{3/2} = 250$ GeV the $\tilde{\chi}_1^0 Z$ channel closes. The same occurs at $m_{1/2} = 960$ GeV ($m_{1/2} = 1460$ GeV) for $m_{3/2} = 500$ GeV ($m_{3/2} = 750$ GeV). After this point, B_p diminishes. Along the focus-point strip, we also can see in the B_p curves the effect of the closing of the $\tilde{\chi}_{1,2}^+ W^-$ channels. In particular, the $\tilde{\chi}_1^+ W^-$ channel closes at $m_{1/2} = 780$ GeV for $m_{3/2} = 500$ GeV, $\tan\beta = 10$, at $m_{1/2} = 1200$ GeV for $m_{3/2} = 750$ GeV, $\tan\beta = 50$, and at $m_{1/2} = 1640$ GeV for $m_{3/2} = 1000$ GeV, $\tan\beta = 50$. For $\tan\beta = 50$, the $\tilde{\chi}_2^+ W^-$ channel closes at $m_{1/2} = 440$ GeV for $m_{3/2} = 500$ GeV, at $m_{1/2} = 760$ GeV for $m_{3/2} = 750$ GeV, and at $m_{1/2} = 1040$ GeV for $m_{3/2} = 1000$ GeV. These thresholds produce distinctive features in the corresponding curves. For very heavy gravitino masses, such as the case $m_{3/2} = 5$ TeV considered here, the dominant two-body decay channels $\tilde{g}g$, $\tilde{t}t$, $\tilde{\chi}_i^0 Z$ and $\tilde{\chi}^+ W^-$ are kinematically available, even in the focus-point region, so no specific features are observed, and the nucleon fractions are similar in all the scenarios studied.

Finally, we note that various other channels close as $m_{1/2}$ increases, without producing any significant features in the B_p curves. For instance, for $\tan\beta = 10$ (upper left panel in Fig. 3), for $m_{3/2} = 250$ GeV, the $\tilde{\chi}_1^0 h$ channel closes at $m_{1/2} = 340$ GeV. The same occurs for the channels $\tilde{g}g$ and $\tilde{\chi}_1^+ H^-$ when $m_{3/2} = 500$ GeV at $m_{1/2} = 220$ GeV, and at $m_{1/2} = 300$ GeV for the channel $\tilde{\chi}_2^+ W^-$. Similarly, for $m_{3/2} = 750$ GeV at $m_{1/2} = 260$ GeV, the channel $\tilde{\chi}_2^+ H^-$ closes, and at $m_{1/2} = 340$ GeV the channels $\tilde{g}g$ and $\tilde{\chi}_1^+ H^-$ close. Just to complete the list for this gravitino mass, at $m_{1/2} = 400$ GeV the Higgs boson channels $\tilde{\chi}_1^0 A, H$ close and at $m_{1/2} = 520$ GeV the chargino channel $\tilde{\chi}_2^+ W^-$ closes.

5 Constraints on Metastable Particles

5.1 Generic Constraints on Abundances of Metastable Particles

Before discussing constraints on specific supersymmetric models with a metastable gravitino, we first discuss constraints on the possible abundance ζ_X of a generic metastable particle X , as a function of its possible lifetime τ_X . We discuss exclusively the constraints due to the effects of the electromagnetic and hadronic showers produced in X decays, postponing to a later paper discussion of the extra constraints that are imposed on the abundances of charged metastable particles by their catalytic effects on light-element abundances due to the formation of bound states. Thus, the constraints presented in this Section apply exclusively to *neutral* metastable particles including, but not limited to, the gravitino. Not wishing to commit to any specific model, we give results for two typical values of B_h , which are applicable also outside the context of specific supersymmetric models. Recall, however, that, as noted above, in specific supersymmetric models one may calculate B_h and it is *not*, in general, constant.

The hadronic decays of metastable particles X affect BBN in different ways, depending on the stage of BBN in which the non-thermal decay particles interact with the background thermal nuclei. This effectively divides the decay effects according to the decaying particle's lifetime τ_X .

- Decays much before weak freeze-out ($\tau_X \ll 1$ sec) produce showers that are thermalized before BBN commences. These decays thus have no impact on light-element abundances, and BBN offers no strong constraints on such short-lived decays.

- Decays during weak freeze-out ($1 \text{ sec} < \tau_X < 100 \text{ sec}$) introduce new interactions that may interconvert the neutrons and protons, e.g., via $n\pi^+ \rightarrow p\pi^0$. These interactions prolong the $n \leftrightarrow p$ equilibrium, and hence delay the freeze-out of the n/p ratio. In this regime the effect on the light elements is somewhat similar to the addition of relativistic species, with the dominant effect being that on ${}^4\text{He}$. However, because the upper limit on ${}^4\text{He}$ is weak [66], this effect does not induce a constraint on our particle properties.

- Finally, decays following weak freeze-out ($\tau_X \gg 100 \text{ sec}$) generate electromagnetic and hadronic showers that induce new (photo)nuclear interactions, which in turn may modify the light-element abundances established previously by BBN.

These processes lead to the constraints seen in Figs. 4–7. These plot abundance contours as a function of pre-decay X abundance ζ_X as in eq. (10) and lifetime τ_X , all for decay spectra corresponding to $(m_{1/2}, m_{3/2}, \tan\beta) = (300 \text{ GeV}, 500 \text{ GeV}, 10)$. In these and subsequent figures, the white regions in each panel are those allowed at face value by the light-element

abundances reviewed in Section 2.1. Specifically, these are: $D/H < 3.2 \times 10^{-5}$, ${}^3\text{He}/D < 1.0$ (also shown are dashed lines for ${}^3\text{He}/D < 0.3$), $Y_4\text{He} > 0.240$, ${}^6\text{Li}/{}^7\text{Li} < 0.05$, and ${}^7\text{Li}/H < 2.75 \times 10^{-10}$. The latter constraint comes from ${}^7\text{Li}$ in globular clusters, and we also demarcate by a dashed line the region within the white area where ${}^7\text{Li}/H < 1.91 \times 10^{-10}$ as inferred from field stars. The regions shaded yellow, red, and magenta regions correspond to progressively larger deviations from the central values of the abundances as noted on the figures. Fig. 4 shows the constraints when the effects of both hadronic and electromagnetic decays are included. To give a sense of how the various decay modes contribute, Fig. 5 shows constraints when hadronic effects are omitted, and only electromagnetic decays are included. Figs. 6 (Fig. 7) both omit effects of electromagnetic decays, and include only hadronic decays to neutrons (protons).

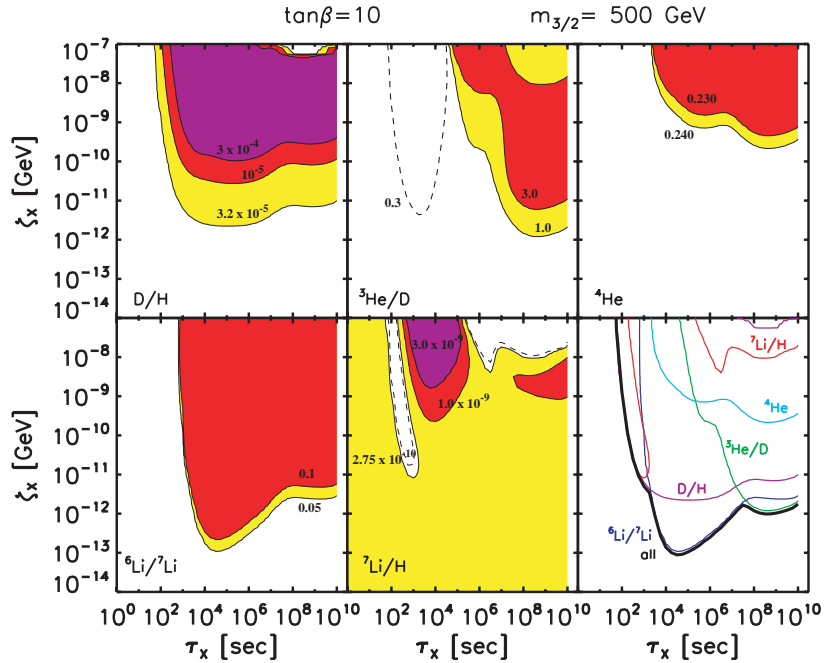


Figure 4: *Plots of abundance versus lifetime for metastable particles X with lifetimes τ_X between 1 and 10^{10} sec, assuming the decay spectra calculated for $(m_{1/2}, m_{3/2}, \tan \beta) = (300 \text{ GeV}, 500 \text{ GeV}, 10)$, in which case $B_p \approx 0.2$ and the electromagnetic branching is $B_{\text{EM}} m_{3/2} = 115 \text{ GeV}$. The X abundance before decay is given by $\zeta_X = m_X n_X / n_\gamma$ (eq. 10). The white regions in each panel are those allowed at face value by the ranges of the light-element abundances reviewed in Section 2.1, whilst the yellow, red and magenta regions correspond to progressively larger deviations from the central values of the abundances.*

The basic features of these plots are similar to those found in previous work, but for completeness we summarize them here. In all plots, we see that at low ζ_X , all constraints

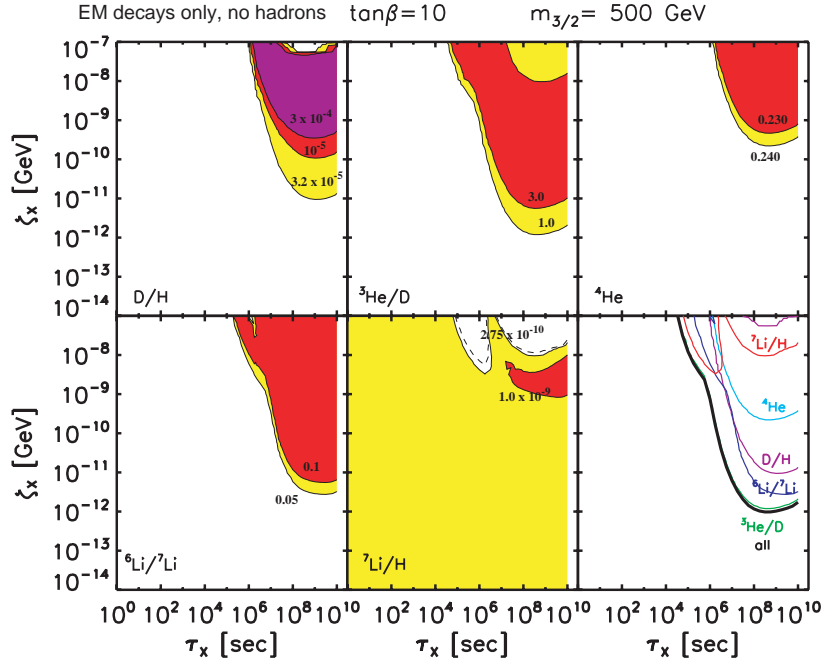


Figure 5: As in Fig. 4, but with electromagnetic decay products only. All hadronic showers and resulting interactions with light elements are ignored.

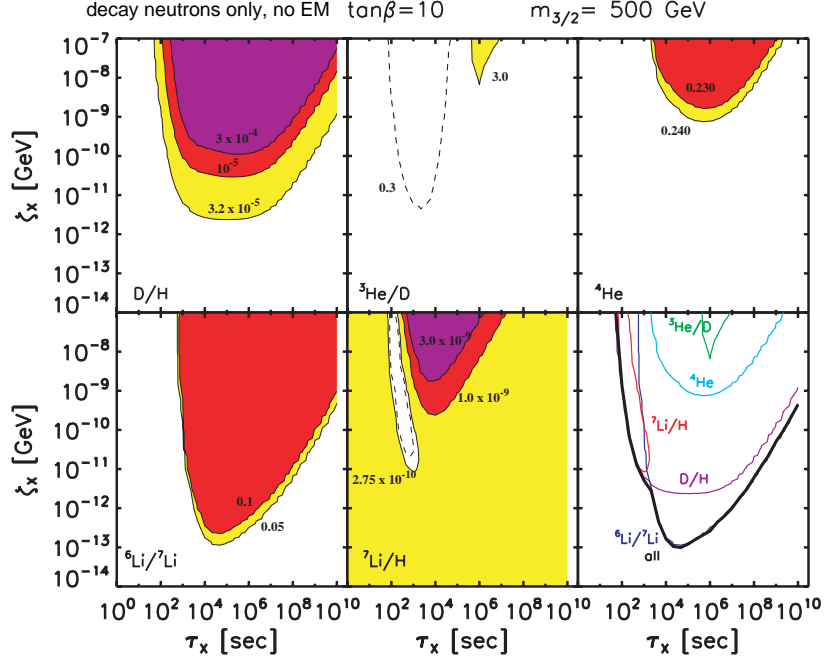


Figure 6: As in Fig. 4, but only with decay neutrons. Decay protons and electromagnetic particles are ignored.

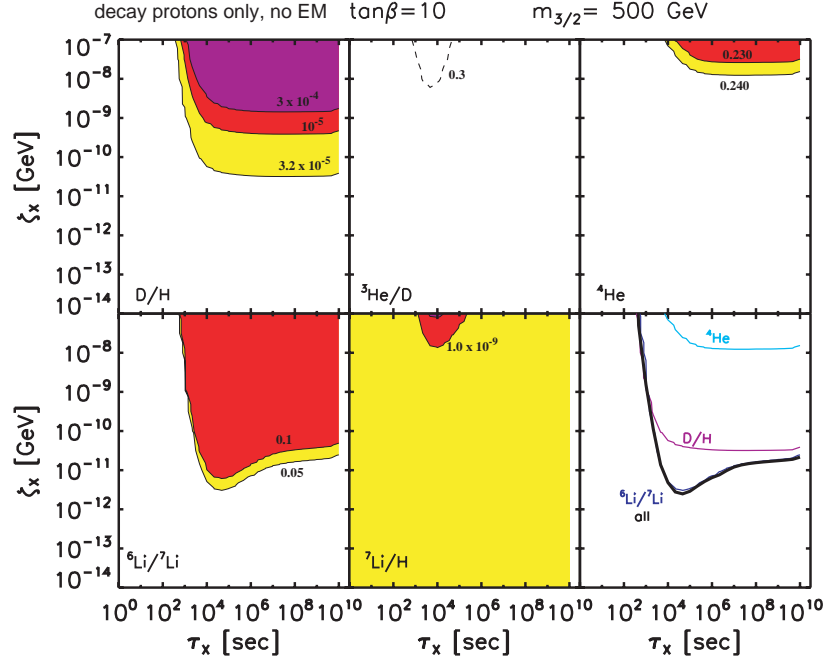


Figure 7: *As in Fig. 4, but only with decay protons. Decay neutrons and electromagnetic particles are ignored.*

are satisfied except for ${}^7\text{Li}$. This is reasonable, as in the limit of $\zeta_X \rightarrow 0$ we recover the standard BBN abundances, which agree well with observations except for the ${}^7\text{Li}$ problem which persists. Also, we see a similar behavior in all plots for small $\tau_X \lesssim 10^2$ sec. Here, the decays occur after weak freezeout but before light element formation occurs, and so for the most part the abundances are unaffected; the main exception is perturbations in ${}^4\text{He}$ due to pion interactions delaying $n \leftrightarrow p$ freezeout.

For several elements the basic trends at $\tau_X \gtrsim 10^2$ sec are relatively simple. We begin with ${}^4\text{He}$, which is the only species for which decays always lead to reduced abundances. This is physically reasonable, since ${}^4\text{He}$ is the most abundant complex species, and the non-thermal reactions represent sinks but not sources. That is, photoerosion and spallation destroy ${}^4\text{He}$, but X decays cannot produce it; hence ${}^4\text{He}$ drops as ζ_X increases. On the other hand, we see that decays increase the D/H abundance, which is readily understood physically. Destruction of ${}^4\text{He}$ produces deuteron fragments, some of which are thermalized before interacting and thus survive. Because ${}^4\text{He}$ is so abundant, even if only a small fraction of ${}^4\text{He}$ is destroyed, the resulting deuteron production can be significant. For ${}^6\text{Li}/{}^7\text{Li}$, the basic trend is also towards increasing production with increasing ζ_X . Here, not-yet-thermalized mass-3 fragments can interact with ambient ${}^4\text{He}$ to produce ${}^6\text{Li}$ via ${}^3\text{He}(\alpha, p){}^6\text{Li}$ and $t(\alpha, n){}^6\text{Li}$. Again, even if

only a small fraction of $A = 3$ nuclei interact this way, this can represent a substantial ${}^6\text{Li}$ abundance compared to observational limits. Moreover, while other secondary processes also contribute to ${}^7\text{Li}$, the much larger effect is for ${}^6\text{Li}$, so that the ${}^6\text{Li}/{}^7\text{Li}$ ratio increases with ζ_X .

By comparing the full constraints (Fig. 4) with those in the electromagnetic-only case of Fig. 5, we see illustrated the well-known result that the electromagnetic decays dominate at $\tau_X \gtrsim 10^6$ sec, but are ineffective at smaller times [29]. Again for D/H, ${}^7\text{Li}/\text{H}$, and ${}^3\text{He}/\text{D}$, we see that the hadronic effects from neutrons and protons (Figs. 6 and 7, respectively) are broadly similar, though the neutron constraints are generally more restrictive out to about $\tau_X \sim 10^6$ sec. As we will see in detail below, this is the timescale for neutron decay to outpace other neutron interactions.

The cases of ${}^7\text{Li}$ and ${}^3\text{He}/\text{D}$ are more complicated. Turning to ${}^7\text{Li}$ in Fig. 4, we see that at intermediate lifetimes ($\sim 10^4$ sec), decays lead to higher ${}^7\text{Li}/\text{H}$; this is due to secondary production from unthermalized mass-3 spallation products, ${}^3\text{He}(\alpha, \gamma){}^7\text{Be}$ and $t(\alpha, \gamma){}^7\text{Li}$. However, at lifetimes around $\tau_X \sim 10^2 - 10^3$ sec, there a narrow “valley” emerges in which ${}^7\text{Li}/\text{H}$ is *reduced*, indeed enough to come into agreement with observational limits. By comparing Figs. 6 and 7, we see that this effect is entirely due to injected neutrons, and is absent when only proton decays are included. This suggests that neutrons are destroying ${}^7\text{Be}$, and that is indeed the case. As noted already by Jedamzik and in subsequent work [21,22], thermalized neutrons can destroy ${}^7\text{Be}$ via ${}^7\text{Be}(n, p){}^7\text{Li}$ and followed by ${}^7\text{Li}(p, \alpha){}^4\text{He}$. We include this effect, but also, as we discuss below (Appendix A), we allow for further ${}^7\text{Be}$ destruction in which the same reactions are initiated by injected neutrons not yet thermalized. This addition slightly enhances the low- ${}^7\text{Li}/\text{H}$ “valley.” Notice that the left side of the “valley” coincides almost exactly with the constraint from D/H, so that we find $\text{D}/\text{H} > 3.2 \times 10^{-5}$ in essentially the entire region where ${}^7\text{Li}/\text{H} < 2.75 \times 10^{-10}$. However, along the left side of the “valley” in Fig. 4, there may be a marginal solution to the ${}^7\text{Li}$ problem, to which we return later in the context of the CMSSM.

Finally, turning to ${}^3\text{He}/\text{D}$ at low lifetimes, we also see a reduction in the ratio for large ζ_X , with a particularly large effect in the neutron-only case. As with ${}^7\text{Li}$ destruction, here the free neutrons preferentially capture on t and ${}^3\text{He}$. This leads to a small ${}^3\text{He}/\text{D}$ ratio as ζ_X increases. Specifically, we see that ${}^3\text{He}/\text{D} < 0.3$ in the narrow strip in Figs. 4 and 6 where the ${}^7\text{Li}$ may (almost) be solved.

For a more quantitative understanding we now apply the analytical model developed above.

5.2 Non-Thermal Abundance Perturbations: Analytical Model

For the reaction $hb \rightarrow \ell$, the rate of decrease of the abundance of the “target” background species b is equal and opposite to the rate of production of background species ℓ , namely

$$-\partial_t Y_b = +\partial_t Y_\ell = Y_b \Gamma_{hb \rightarrow \ell}, \quad (27)$$

where the reaction rate per target b is given in the thin- and thick-target limits in (25). The net change in these abundances due to this reaction is the time integral of the rate:

$$-\Delta Y_b = +\Delta Y_\ell = \int Y_b \Gamma_{hb \rightarrow \ell} dt \approx Y_b \Gamma_{hb \rightarrow \ell} \tau_X. \quad (28)$$

In the last expression we take the “exposure time” to be the X lifetime $\tau_X = 1/\Gamma_X$; this is the equivalent of the instantaneous-decay approximation used in the EM case. Since the non-thermal spectra, and thus non-thermal reaction rates, scale as $N_h \sim \Gamma_{hb \rightarrow \ell} \sim \Gamma_X$, the lifetime dependence drops out in the abundance changes.

For the thin-target case, we have

$$\Delta Y_\ell^{\text{bg}} \Big|_{hb \rightarrow \ell}^{\text{thin}} = Y_X \frac{Y_b^{\text{bg}}}{Y_k^{\text{bg}}} \int_{\epsilon_{\text{th}}} Q_h(\epsilon) \frac{\sigma_{hb \rightarrow \ell}(\epsilon)}{\sigma_{hk \rightarrow \text{inel}}} d\epsilon \quad (29)$$

$$= Y_X \frac{Y_b^{\text{bg}}}{Y_k^{\text{bg}}} Q_h(> \epsilon_{\text{th}}) \left\langle \frac{\sigma_{hb \rightarrow \ell}(\epsilon)}{\sigma_{hk \rightarrow \text{inel}}} \right\rangle, \quad (30)$$

where the spectrum-weighted average is

$$\langle \sigma_b / \sigma_k \rangle = \frac{\int_{\epsilon_{\text{th}}} Q_h(\epsilon) \sigma_b(\epsilon) / \sigma_k(\epsilon) d\epsilon}{\int_{\epsilon_{\text{th}}} Q_h(\epsilon) d\epsilon}. \quad (31)$$

We see that the abundance change is determined by several parameters. The scaling with Y_X is intuitively clear—the perturbation should be proportional to the number of non-thermal decays per baryon. Another important parameter is the number $Q_h(> \epsilon_{\text{th}}) \approx B_h$ of non-thermal h particles per decay above threshold, which is to an excellent approximation the total number of h particles per X decay, also an intuitive result. Finally, the cross-section factor is an analogue of a branching ratio for the reaction in question relative to all inelastic reactions.

For the thick-target case, we have

$$\Delta Y_\ell \Big|_{hb \rightarrow \ell}^{\text{thick}} = Y_X Y_b^{\text{bg}} \int_{\epsilon_{\text{th}}} Q_h(> \epsilon) \frac{\sigma_{hb \rightarrow \ell} / m_p}{d\epsilon_h / dR} d\epsilon \quad (32)$$

$$= Y_X Y_b^{\text{bg}} Q_h(> \epsilon_{\text{th}}) \langle R \rangle \langle \sigma_{hb \rightarrow \ell} / m_p \rangle \quad (33)$$

$$\approx 6 \times 10^{-4} Y_X Y_b^{\text{bg}} \left(\frac{B_h}{10^{-2}} \right) \left(\frac{\langle R \rangle}{1 \text{ g cm}^{-2}} \right) \left(\frac{\langle \sigma \rangle}{30 \text{ mbarn}} \right), \quad (34)$$

where we again define weighted averages of the cross section $\langle\sigma\rangle$ and stopping range $\langle R\rangle$ (with units $[\text{g}/\text{cm}^2]$) as

$$\langle\sigma\rangle = \frac{\int_{\epsilon_{\text{th}}} Q_h(>\epsilon) \sigma_{hb\rightarrow\ell} (d\epsilon_h/dR)^{-1} d\epsilon}{\int_{\epsilon_{\text{th}}} Q_h(>\epsilon) (d\epsilon_h/dR)^{-1} d\epsilon}, \quad (35)$$

$$\langle R\rangle = \frac{\int_{\epsilon_{\text{th}}} Q_h(>\epsilon) (d\epsilon_h/dR)^{-1} d\epsilon}{Q_h(>\epsilon_{\text{th}})}. \quad (36)$$

Recall that $\langle R\rangle \propto Y_{e^\pm}^{-1}$ and the fiducial value we choose is appropriate for $Y_{e^\pm}^{-1} \sim 1$. We see that the abundance perturbations for hadronic decays scale with—and thus constrain—the *number* of pre-decay X particles (gravitinos, in the present study) per baryon (or equivalently per photon or per unit entropy). However, to show hadronic as well as electromagnetic results on the same plot, it is useful to introduce $\zeta_X = m_X Y_X \eta$ as in eq. (10), so that $Y_X = \zeta_X / \eta m_X$. We now apply the observed abundance constraints and express them in terms of ζ_X .

Consider some light-element abundance constraint Y_ℓ^{lim} . The perturbation saturates this constraint when $\Delta Y_\ell = \delta Y_\ell^{\text{obs}} \equiv Y_\ell^{\text{lim}} - Y_\ell^{\text{std}}$, where Y_ℓ^{std} is the standard BBN result (see e.g. [6]). This abundance will be reached for some value of Y_X and thus ζ . Namely, we have

$$\begin{aligned} \zeta_{X,\text{lim}}^{\text{thin}} &\simeq m_X \eta \delta Y_\ell^{\text{obs}} \frac{Y_k^{\text{bg}}}{Y_b^{\text{bg}}} B_h^{-1} \left\langle \frac{\sigma_{hb\rightarrow\ell}}{\sigma_{hk\rightarrow\text{inel}}} \right\rangle^{-1} \\ &= 10^{-11} \text{ GeV} \left(\frac{\delta Y_\ell^{\text{obs}}}{0.4 \times 10^{-5}} \right) \left(\frac{m_X}{500 \text{ GeV}} \right) \left(\frac{0.2}{B_h} \right) \left(\frac{Y_k^{\text{bg}}}{Y_b^{\text{bg}}} \right) \left(\frac{0.5}{\langle\sigma_{hb\rightarrow\ell}/\sigma_{hk\rightarrow\text{inel}}\rangle} \right), \end{aligned} \quad (37)$$

where the fiducial values are appropriate for constraints based on D/H, produced mostly via ${}^4\text{He}$ spallation. Here we take the total inelastic interactions $hk \rightarrow \text{inel}$ to be dominated by interactions with background ${}^4\text{He}$, so that $Y_k^{\text{bg}}/Y_b^{\text{bg}} = 1$; this is the case for nucleons up to $\epsilon \sim 10$ GeV, and beyond this the smaller NN inelastic cross sections change the result by no more than about a factor of 2.

We compare our analytical estimates to numerical results for the production of deuterium obtained using our codes, as shown in Figs. 4–7. We see that for short lifetimes, our prediction from eq. (37) agrees with the D/H abundance constraints for $Y_{\text{D}} = 3.2 \times 10^{-5}$ to within a factor of 3. In particular, our thin-target estimate is a good description of the neutron-only results (Fig. 6). This was to be expected as neutron propagation is, for these X lifetimes, well within the thin-target regime.

For the thick-target case, putting $\Delta Y_\ell = \delta Y_\ell^{\text{obs}}$ gives

$$\zeta_{X,\text{lim}}^{\text{thick}} \simeq m_X \eta \frac{\delta Y_\ell^{\text{obs}}}{Y_b^{\text{bg}}} B_h^{-1} \frac{m_p / \langle \sigma_{hb \rightarrow \ell} \rangle}{\langle R \rangle} \quad (38)$$

$$= 10^{-9} \text{ GeV} \quad (39)$$

$$\times \left(\frac{\delta Y_\ell^{\text{obs}}}{0.4 \times 10^{-5}} \right) \left(\frac{m_X}{500 \text{ GeV}} \right) \left(\frac{0.2}{B_h} \right) \left(\frac{0.1}{Y_b^{\text{bg}}} \right) \left(\frac{100 \text{ mb}}{\langle \sigma_{hb \rightarrow \ell} \rangle} \right) \left(\frac{1 \text{ g cm}^{-2}}{\langle R \rangle} \right),$$

where again we use fiducial values that are appropriate for constraints based on D/H, produced mostly via ^4He spallation and $Y_{e^\pm} = 1$. We see that the thick-target limits are about a factor ~ 100 weaker than the thin-target limits. This is reasonable, as the thick-target limit is less efficient in light-element production. Again comparing Figs. 4-7, we see that the proton-only results (Fig. 7) lie between the thin- and thick-target estimates. This is also as expected: for the X lifetimes of interest, the proton propagation is partially within the thick-target regime.

Given our success in understanding of D/H, it is worth extending the analysis to ^6Li , which should be due to secondary production of non-thermalized mass-3 nuclides via $^3\text{He}(\alpha, p)^6\text{Li}$ and $t(\alpha, n)^6\text{Li}$. If this is the case, then the ^6Li abundance should be given by the product of the non-thermal mass-3 abundance ΔY_3 and the probability that the mass-3 nuclide interacts before it stops. But for the thin-target case, the probability is small, and is just given by the product of the mass-3 interaction rate $\Gamma_{3\alpha} = Y_\alpha^{\text{bg}} n_B \sigma_{3\alpha} v$ times its stopping time $\tau_{3,\text{stop}} = (\int b^{-1} d\epsilon) \approx (m_p n_B v / R_3)^{-1}$, with R_3 the mass stopping grammage. Thus we have

$$\Delta Y(^6\text{Li}) = \Delta Y_3 Y_\alpha^{\text{bg}} R_3 \frac{\sigma(^3A\alpha \rightarrow N^6\text{Li})}{m_p}, \quad (40)$$

with $Y_\alpha^{\text{bg}} \sim 0.1$. Using the above thin-target expression for ΔY_d (eq. 29), and taking $(^3\text{He}/\text{D})_{\text{spall}} \sim 1$ for spallation production, this becomes

$$\Delta Y(^6\text{Li}) \approx \frac{\zeta_X}{\eta m_X} B_h \left\langle \frac{\sigma_{hb \rightarrow \ell}}{\sigma_{hk \rightarrow \text{inel}}} \right\rangle Y_\alpha^{\text{bg}} R_3 \frac{\sigma(^3A\alpha \rightarrow N^6\text{Li})}{m_p}. \quad (41)$$

Assuming the ^7Li perturbation is small, so that $Y(^7\text{Li}) \approx Y(^7\text{Li})_{\text{BBN, std}} \sim 3 \times 10^{-10}$, we solve for ζ_X in terms of the observed limit on $^6\text{Li}/^7\text{Li} = Y(^6\text{Li})/Y(^7\text{Li})$:

$$\zeta_{X,\text{lim}}^{\text{thin}}(^6\text{Li}) \simeq \eta m_X (^6\text{Li}/^7\text{Li})_{\text{obs}} \frac{Y(^7\text{Li})}{Y_\alpha^{\text{bg}}} B_h^{-1} \left\langle \frac{\sigma_{hb \rightarrow \ell}}{\sigma_{hk \rightarrow \text{inel}}} \right\rangle^{-1} \frac{m_p}{R_3 \sigma(^3A\alpha \rightarrow N^6\text{Li})} \quad (42)$$

$$\sim 2.5 \times 10^{-14} \text{ GeV} \left(\frac{^6\text{Li}/^7\text{Li}|_{\text{obs}}}{0.05} \right) \left(\frac{1 \text{ g/cm}^2}{R_3} \right) \left(\frac{30 \text{ mb}}{\sigma(^3A\alpha \rightarrow N^6\text{Li})} \right), \quad (43)$$

where the fiducial values not shown are the same as in eq. (37). This result within a factor of 3 the strongest ${}^6\text{Li}/{}^7\text{Li}$ constraints around $\tau_X \sim 10^4$ sec, where the neutrons have time to interact before they decay.

The agreement between our order-of-magnitude estimates and full numerical results serves as a strong check on our analysis and gives us confidence in both approaches.

5.3 Constraints on the Abundance of a Massive Gravitino

We now apply the above analysis to the specific class of supersymmetric scenarios with a metastable massive gravitino and a neutralino LSP χ .

We recall that neutralino LSP scenarios are characterized by narrow strips along which the relic χ density lies within the range $0.0975 < \Omega_{\text{CDM}} h^2 < 0.1223$ that is favored by WMAP and other observations [1]. Since this range is relatively narrow (namely only a few %), within any specific supersymmetric scenario it determines some combination of the model parameters also to within $\mathcal{O}(\text{few})$ %. A more detailed discussion is given in [47], where some explicit parameterizations of such WMAP strips are given. In the examples given there, the value of m_0 is tightly determined in CMSSM scenarios as a function of $m_{1/2}$ for fixed values of $\tan\beta$ and A_0 . Many properties of these supersymmetric models change little as one varies m_0 across such a narrow WMAP strip. Specifically, the branching ratios for massive gravitino decay and hence B_h vary little across a strip, and one may usefully represent the cosmological constraints on such CMSSM scenarios as functions of $m_{1/2}$ alone, using a representative value of B_h that is calculated as a function of $m_{1/2}$.

One representative example is shown in Fig. 8: the first five panels, with shadings, display the effects of the decays of a gravitino with a mass $m_{3/2} = 250$ GeV on the different light-element abundances (D/H, ${}^3\text{He}/\text{D}$, ${}^4\text{He}$, ${}^6\text{Li}/{}^7\text{Li}$ and ${}^7\text{Li}/\text{H}$) as functions of $m_{1/2}$ along the WMAP strip in the coannihilation region for a CMSSM scenario with $\tan\beta = 10$, $A_0 = 0$. As in Fig. 4 - 7, the white regions in each panel are those allowed at face value by the ranges of the light-element abundances reviewed in Section 2.1, and the yellow, red, and magenta regions correspond to progressively larger deviations from the central values of the abundances. The final panel (bottom right), shows the strongest constraints from each abundance, as labeled, and from these one infers the strongest overall constraint, shown by the thick black curve.

We first note that all constraints weaken abruptly as $m_{1/2} \rightarrow 600$ GeV. This corresponds to the limiting case when $m_\chi \sim 0.42m_{1/2} \rightarrow m_{3/2} = 250$ GeV. In this limit, the energies in the EM and HD showers vanish, and the effects of gravitino decay disappear. Note

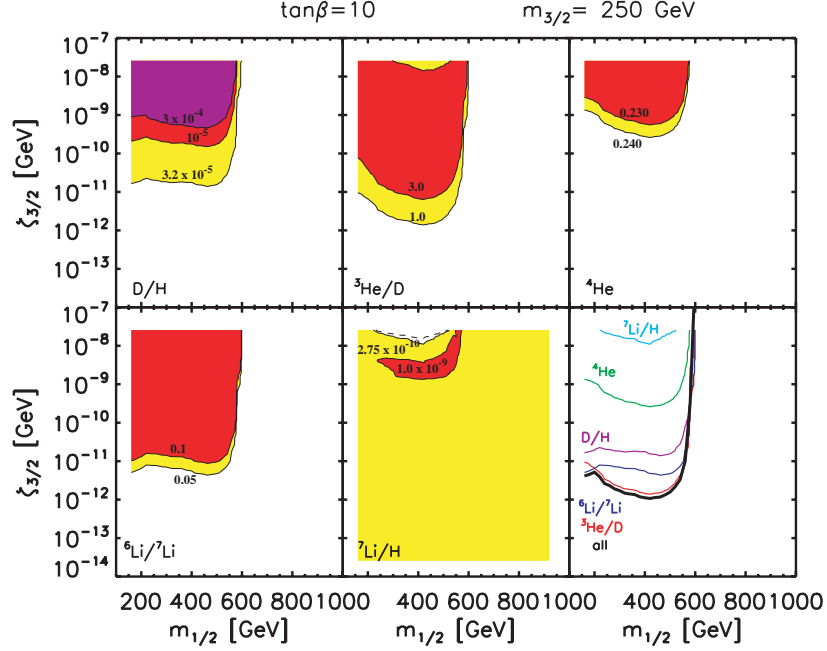


Figure 8: *The effects of the decays of a gravitino with a mass $m_{3/2} = 250$ GeV on the different light-element abundances (D/H , ${}^3\text{He}/D$, ${}^4\text{He}$, ${}^7\text{Li}/H$ and ${}^6\text{Li}/{}^7\text{Li}$) as a function of $m_{1/2}$ along the WMAP coannihilation strip for a CMSSM scenario with $\tan\beta = 10$, $A_0 = 0$. As in Figs. 4, the white regions in each panel are those allowed at face value by the light-element abundances reviewed in Section 2.1, and the yellow, red, and magenta regions correspond to progressively larger deviations from the central values of the abundances.*

that $m_{1/2} = 250$ GeV is the smallest value we consider; for larger values this effect is less important.

Consider now the D/H constraints in the region $m_{1/2} \lesssim 600$ GeV in the top left panel of Fig. 8. We see that the lowest contour, at $D/H = 3.2 \times 10^{-5}$, lies at about $\zeta_{3/2} \simeq 10^{-11}$ GeV between $m_{1/2} = 180$ GeV and just under 600 GeV¹. To understand this behavior, we recall from Fig. 1 that for $m_{1/2} = 180 - 580$ GeV, the gravitino lifetime grows from about 10^7 sec to 10^{10} sec, and in Fig. 3 we see that the nucleon branching ratios $B_p \approx B_n \sim 6 \times 10^{-2}$ for $m_{1/2} \lesssim 400$ GeV. Combining these with the generic lifetime dependence in Fig. 4, we see that for $B_p \approx B_n \sim 2 \times 10^{-1}$, the lowest D/H contour for $\tau \gtrsim 10^7$ sec is roughly constant at $\zeta_{3/2} \sim 3 \times 10^{-12}$ GeV. In our case, these constraints weaken due to the lower branching ratios by a factor ~ 3 , yielding the value $\zeta_{3/2} \sim 10^{-11}$ GeV seen in Fig. 8. The higher D/H contours in Fig. 8 can be understood in a similar manner.

As another example, consider the ${}^7\text{Li}/H$ panel in the bottom middle panel of Fig. 8.

¹We recall that the gravitino becomes the LSP for $m_{1/2} \gtrsim 600$ GeV, in which case a different analysis is necessary.

There we see, for $m_{1/2} \lesssim 600$ GeV, an “island” of the lowest constraint where $\zeta_{3/2} \sim 10^{-10} - 10^{-8}$ GeV. As $\zeta_{3/2}$ drops, ${}^7\text{Li}/\text{H}$ then grows, peaking to highest level where $\zeta_{3/2} \sim 3 \times 10^{-9}$ GeV. Then as $\zeta_{3/2}$ continues to decrease, ${}^7\text{Li}/\text{H}$ continues drops down to its standard BBN level. From the generic plot Fig. 4, we see that for $\tau \gtrsim 10^7$ sec and with $B_p \sim 0.2$, the ${}^7\text{Li}/\text{H}$ constraint forms an island around $\zeta_{3/2} \sim 10^{-9}$ GeV, with a width that grows with τ . Scaling down to the lower branching, we again can understand the behavior in Fig. 8.

The fact that this qualitative analysis works so well indicates that the generic results are a good approximation to the full ones, modulo changes in branching ratios. However, the generic results are for a particular decay spectrum whereas, as we have seen, there are significant variations in the decay spectrum. Thus we infer that our results are not strongly dependent on the detailed shapes of the decay spectra beyond the sensitivity to the branching ratios. This also makes sense in terms of our analytic approximations, which suggest that the decay spectra enter principally via their integral properties and particularly their branching ratios.

This understanding of the non-thermal particle effects leading to our constraints gives confidence in our results, and thus to their implications for supersymmetry. Namely, again in the case of Fig. 8 where $\tan\beta = 10$ and $m_{3/2} = 250$ GeV, the fact that the observed abundances generally agree with the standard BBN calculations implies that the allowed (white) regions are generally at low gravitino abundance. The exception is the bottom middle panel, where the observational discrepancy with the standard BBN calculation of the ${}^7\text{Li}$ abundance is reflected in the fact that the yellow region extends from a vanishing gravitino abundance up to quite large values, and the “preferred” white region appears only when $\zeta_{3/2} > 10^{-9}$ GeV and $m_{1/2}$ is not too large ². It is clear that this “preferred” region for ${}^7\text{Li}/\text{H}$ is incompatible with the allowed regions for the other light-element abundances shown in the other panels. Thus, there is no value of $m_{1/2}$ in this particular CMSSM scenario that solves the ${}^7\text{Li}/\text{H}$ problem. As already mentioned, we disregard the ${}^7\text{Li}/\text{H}$ problem in the compilation of constraints shown in the bottom right panel of Fig. 8, and in the following discussion.

The weakening of the constraints as $m_{1/2} \rightarrow 600$ GeV implies that a large abundance is allowed for $m_{3/2} = 250$ GeV if $m_{1/2} \sim 600$ GeV, apart from the issue of the ${}^7\text{Li}$ abundance. We recall that if $m_{1/2} > 600$ GeV with fixed $m_{3/2} = 250$ GeV, the gravitino becomes the LSP and the lightest neutralino becomes the NLSP. In this case, the constraint due to the cosmological relic density should be applied to the gravitino, the WMAP strip is no longer

²We also note the existence of a more disfavored (red) region in the bottom middle panel showing the ${}^7\text{Li}/\text{H}$ ratio, appearing when $\zeta_{3/2} > 10^{-9}$ GeV and $m_{1/2} \sim 500$ GeV.

relevant, and a different analysis would be required.

In the final, summary panel of Fig. 8 (bottom right), we see explicitly that the ${}^7\text{Li}$ constraint (light blue) is incompatible with the other constraints due to ${}^4\text{He}$ (green), D/H (magenta), ${}^3\text{He}/\text{D}$ (red) and ${}^6\text{Li}/{}^7\text{Li}$ (dark blue). The weakest of these constraints is that due to ${}^4\text{He}$, the two strongest constraints at smaller and larger $m_{1/2}$, respectively, are those due to ${}^6\text{Li}/{}^7\text{Li}$ and ${}^3\text{He}/\text{D}$, and the combined constraint is shown in black. We see that it hovers in the range $\zeta_{3/2} = m_{3/2}n_{3/2}/n_\gamma \sim 3 \times 10^{-12}$ to 10^{-12} GeV, corresponding to $n_{3/2}/n_\gamma \sim 10^{-14}$, except in the limit as $m_{1/2} \rightarrow 600$ GeV.

Figs. 9, 10, 11, and 12 show the correspondingly coloured regions of varying discomfort for the different light-element abundances for the larger values of $m_{3/2} = 500$ GeV, 750 GeV, 1000 GeV and 5000 GeV, respectively. The constraints are shown for the full length of the WMAP strip up to $m_{1/2} \sim 900$ GeV, along which $m_\chi < m_{3/2}$ for all the displayed values of $m_{3/2}$. For $m_{3/2} \leq 1000$ GeV, we see that the D/H constraint (top left panel in each plot) and the ${}^4\text{He}$ constraint (top right in each plot) are relatively stable, reflecting the rough constancy of the D/H results for long lifetimes (see Fig. 4), and the rough constancies of the branching ratios (see Fig. 3). For $m_{3/2} = 5000$ GeV, the short lifetimes (see Fig. 1) severely weaken the constraints for all elements (cf. Fig. 4), with D/H surviving as the strongest for all $m_{1/2}$. We discuss later the case of large $m_{3/2}$.

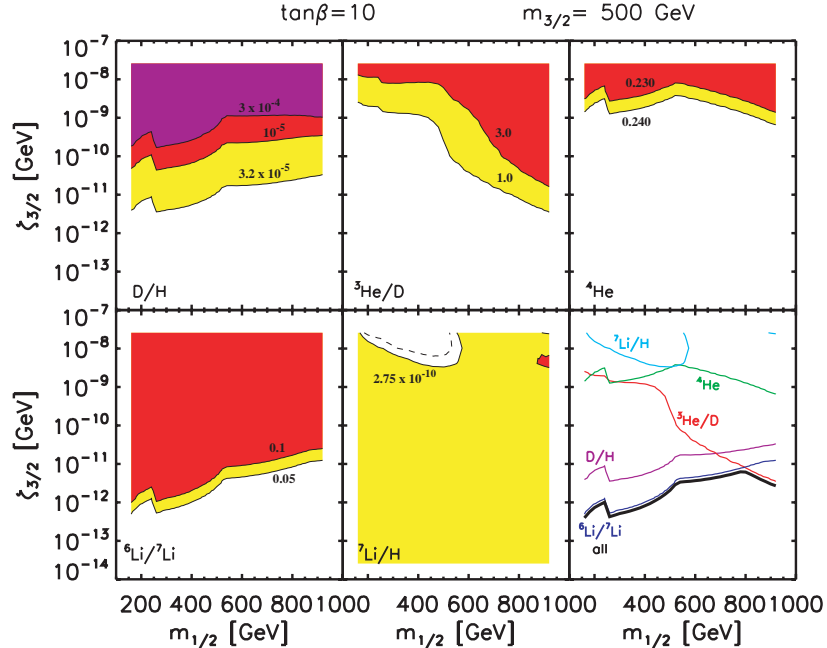


Figure 9: As for Fig. 8, with $m_{3/2} = 500$ GeV but unchanged values for the CMSSM parameters.

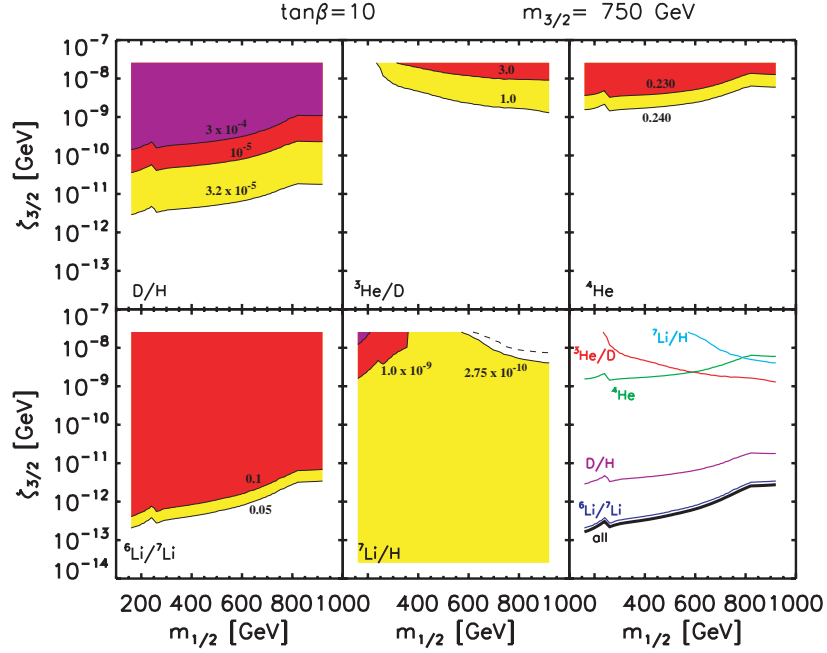


Figure 10: As for Fig. 8, with $m_{3/2} = 750 \text{ GeV}$ but unchanged values for the CMSSM parameters.

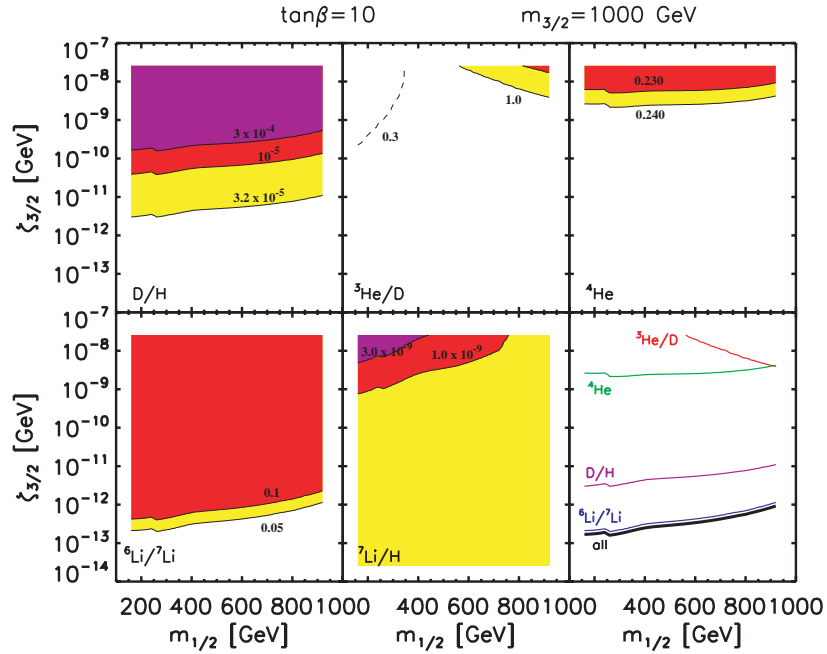


Figure 11: As for Fig. 8, with $m_{3/2} = 1000 \text{ GeV}$ but unchanged values for the CMSSM parameters.

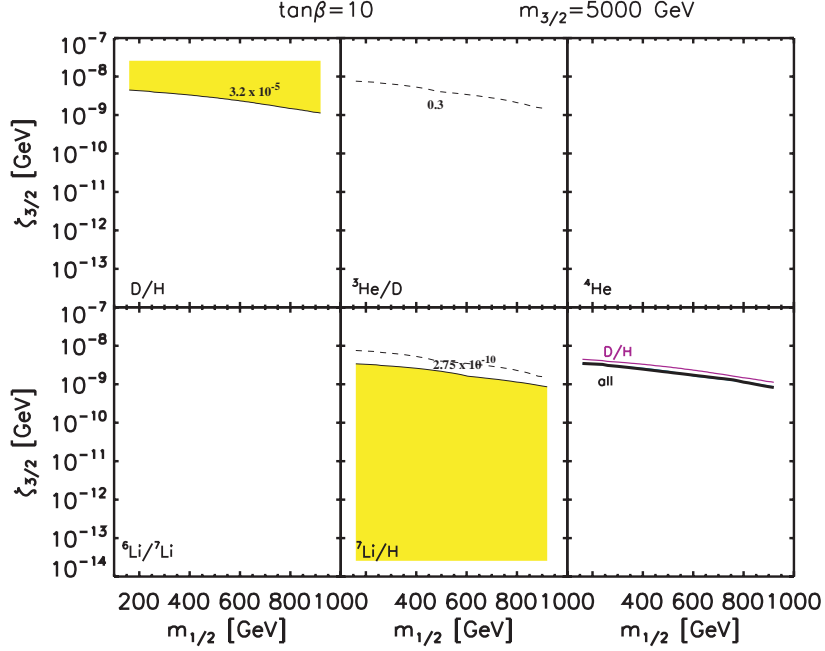


Figure 12: As for Fig. 8, with $m_{3/2} = 5000$ GeV but unchanged values for the CMSSM parameters.

In the case of ${}^7\text{Li}/\text{H}$ (bottom middle panels), the “preferred” white region changes position as $m_{3/2}$ increases, moving to larger $m_{1/2}$ for $m_{3/2} = 500, 750$ GeV, but reverting to low $m_{1/2}$ at high $m_{3/2}$. The $m_{1/2}$ mass ranges are those which have lifetimes near $\sim 3 \times 10^6$ sec (see Fig. 4), whereas the ${}^7\text{Li}$ constraint is strongest for long lifetimes. However, there is no overlap between the white regions in this and the other panels, implying that the ${}^7\text{Li}$ problem cannot be solved for any value of $m_{3/2}$ for the particular values of $\tan\beta$ and A_0 chosen here. As stated previously, we do not include the ${}^7\text{Li}$ constraint in our compilation. As ${}^7\text{Li}$ is problematic in standard BBN, the inclusion of this constraint would give the false impression that nearly every supersymmetric model with a decaying gravitino is excluded. We are therefore implicitly assuming that there is another solution for the ${}^7\text{Li}$ problem, e.g., due to observational or astrophysical uncertainties as discussed in Section 2.1. In contrast, the constraints from the other light elements perturb the previous concordance of BBN with respect to those elements.

Finally, we note that for $m_{3/2} = 500$ to 1000 GeV, the ${}^6\text{Li}/{}^7\text{Li}$ constraint is significantly stronger than for $m_{3/2} = 250$ GeV, becoming progressively stricter. This reflects the stronger limits arising when the gravitino lifetime is shorter (see Fig. 4). In all cases the ${}^6\text{Li}/{}^7\text{Li}$ ratio provides the most restrictive limit on $\zeta_{3/2}$, and strengthens by a factor ~ 10 as $m_{1/2}$ increases from 250 to 1000 GeV. Specifically, we find $\zeta_{3/2} \lesssim 10^{-12} - 10^{-11}$ GeV for $m_{3/2} = 500$ GeV,

$\zeta_{3/2} \lesssim 3 \times 10^{-13} - 3 \times 10^{-12}$ GeV for $m_{3/2} = 750$ GeV, and $\zeta_{3/2} \lesssim 10^{-13} - 10^{-12}$ GeV for $m_{3/2} = 1000$ GeV.

In the case of Fig. 12, we see that the most significant upper limit on the gravitino abundance is that from D/H. Comparing this with the *lower* limit on the gravitino abundance coming from ${}^7\text{Li}/\text{H}$, we see that they are marginally compatible over essentially the full range of $m_{1/2}$ displayed. However, this conclusion is crucially dependent on the precise implementations of the D/H and ${}^7\text{Li}/\text{H}$ constraints: for example, if the upper limit on the ${}^7\text{Li}/\text{H}$ abundance is strengthened to 1.91×10^{-10} , as suggested by field stars and indicated by the dashed line in the middle lower panel of Fig. 12, compatibility becomes more difficult.

Figs. 13–17 are the same as Figs. 8–12, but for $\tan\beta = 50$. Similar trends emerge as for the $\tan\beta = 10$ results, with some differences of detail due to the more rapid rise in lifetimes with $m_{1/2}$ (Fig. 1). The range in $m_{1/2}$ is extended to almost 1.9 TeV and includes the rapid annihilation funnel in addition to the coannihilation region. We again see that no regions allow for a solution to the ${}^7\text{Li}$ problem while simultaneously satisfying the other light-element constraints. The constraints on $\zeta_{3/2}$ are again dominated by the ${}^6\text{Li}/{}^7\text{Li}$ ratio, and are weak for $m_{3/2} = 5000$ GeV. As in the $\tan\beta = 10$ case, the ${}^7\text{Li}/\text{H}$ constraint is incompatible with the others for $m_{3/2} \leq 1000$ GeV, but may be marginally compatible for $m_{3/2} = 5000$ GeV.

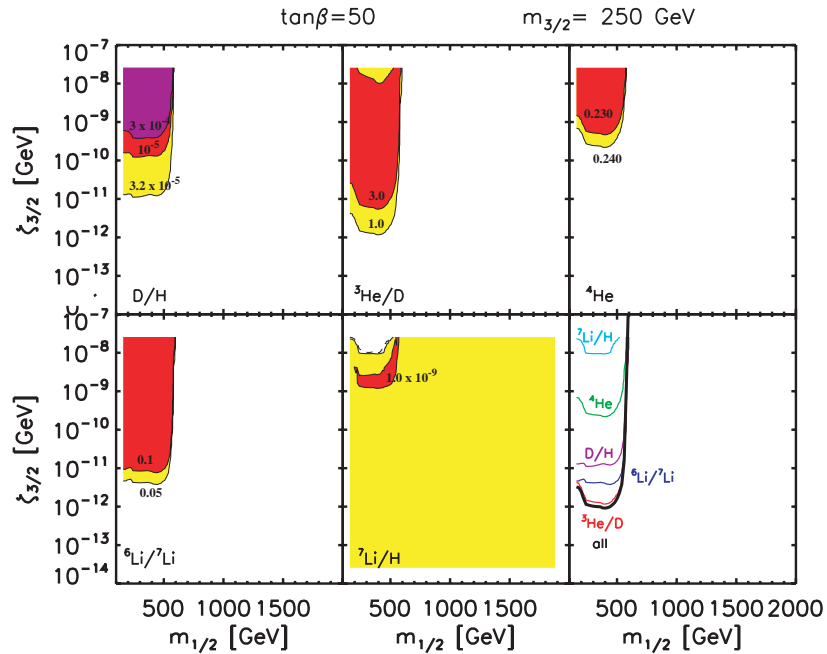


Figure 13: As for Fig. 8, with $m_{3/2} = 250$ GeV but $\tan\beta = 50$ and unchanged values for the CMSSM parameters.

Figs. 18–22 present a similar analysis to that in Figs. 8–12, but for the focus-point region

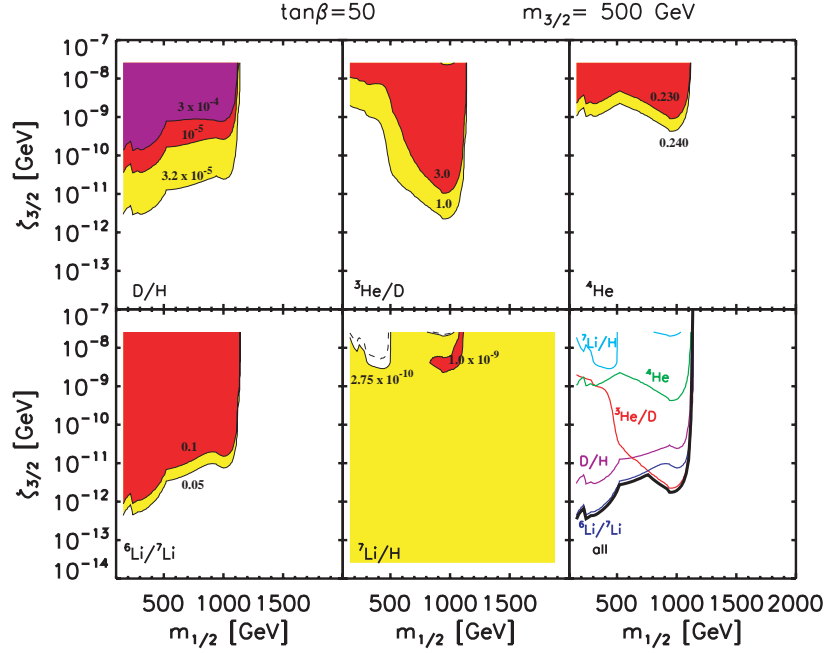


Figure 14: As for Fig. 8, with $m_{3/2} = 500 \text{ GeV}$, but $\tan\beta = 50$ and unchanged values for the CMSSM parameters.

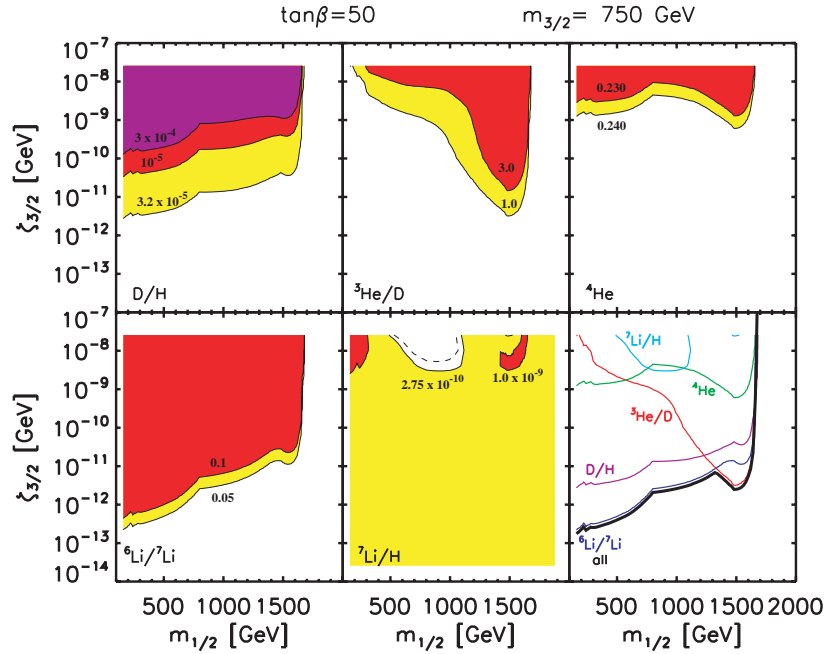


Figure 15: As for Fig. 8, with $m_{3/2} = 750 \text{ GeV}$, but $\tan\beta = 50$ and unchanged values for the CMSSM parameters.

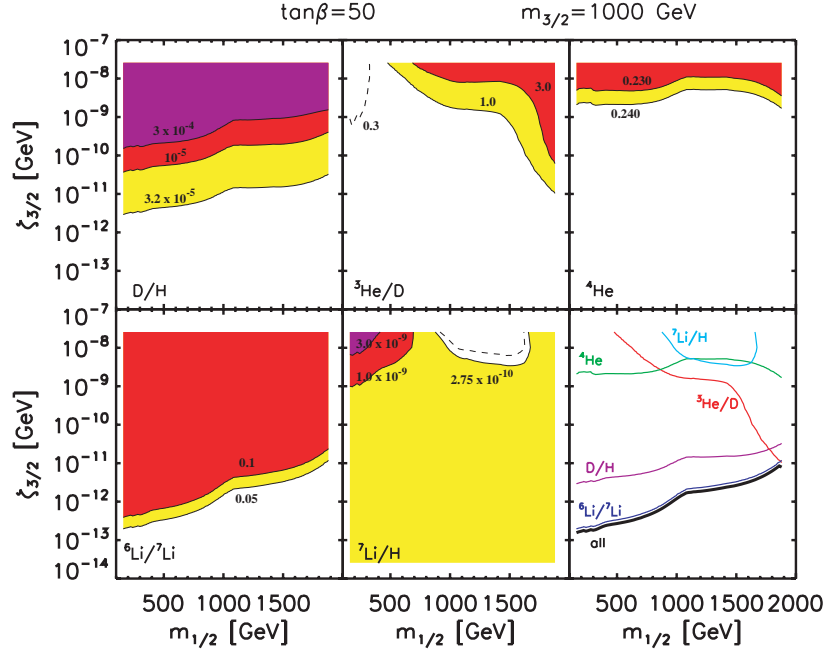


Figure 16: As for Fig. 8, with (top left) $m_{3/2} = 1000$ GeV, but $\tan\beta = 50$ and unchanged values for the CMSSM parameters.

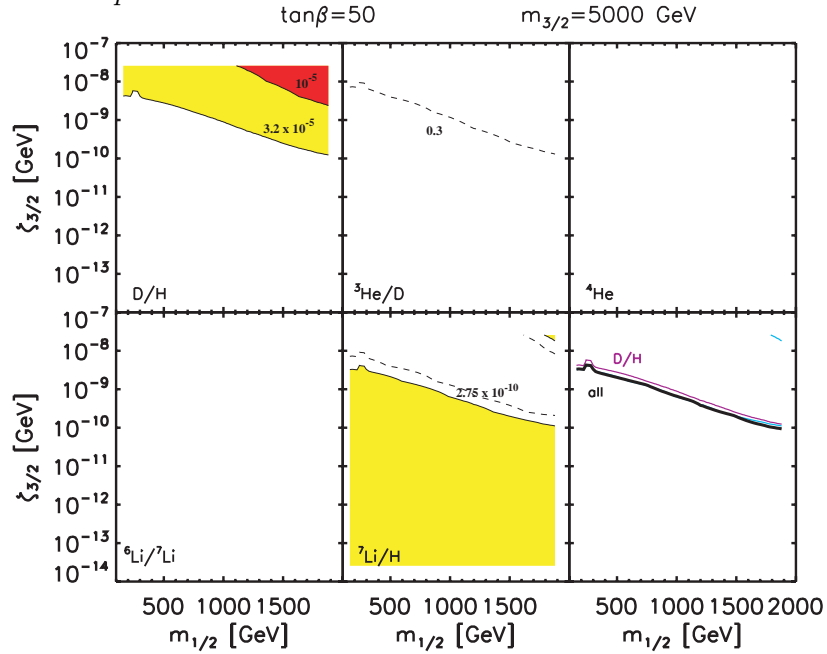


Figure 17: As for Fig. 8, with $m_{3/2} = 5000$ GeV, but $\tan\beta = 50$ and unchanged values for the CMSSM parameters.

of the CMSSM with $\tan\beta = 10$. The results are also largely similar to those for the previous cases. The same is true for the focus-point region of the CMSSM with $\tan\beta = 50$, shown in Fig. 23–27. As in the previous cases, the ${}^7\text{Li}/\text{H}$ constraint is incompatible with all the other constraints, except possibly for $m_{3/2} = 5000$ GeV.

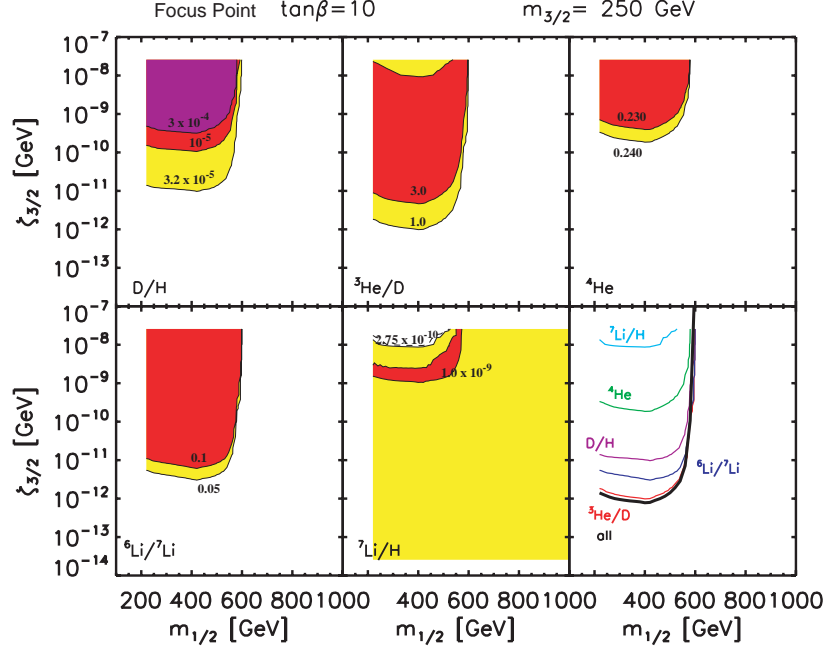


Figure 18: As for Fig. 8, with $m_{3/2} = 250$ GeV, but $\tan\beta = 10$ and CMSSM parameters appropriate for the WMAP strip in the focus-point region.

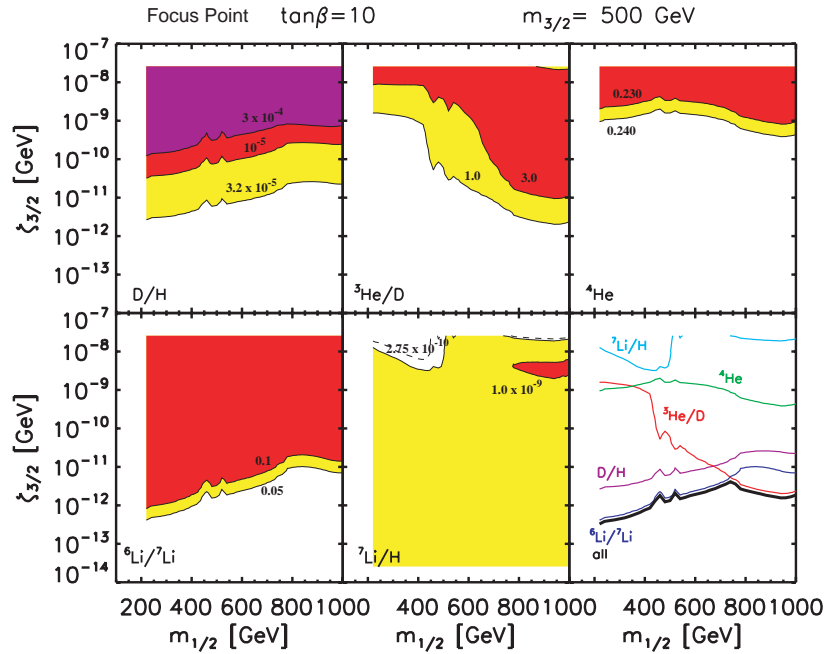


Figure 19: As for Fig. 8, with $m_{3/2} = 500$ GeV, but $\tan\beta = 10$ and CMSSM parameters appropriate for the WMAP strip in the focus-point region.

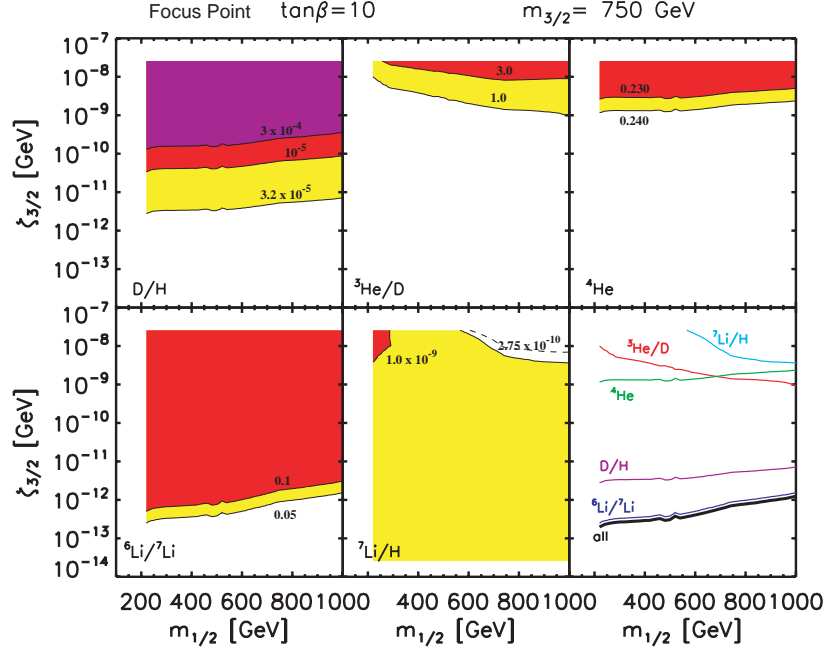


Figure 20: As for Fig. 8, with $m_{3/2} = 750$ GeV, but $\tan\beta = 10$ and CMSSM parameters appropriate for the WMAP strip in the focus-point region.

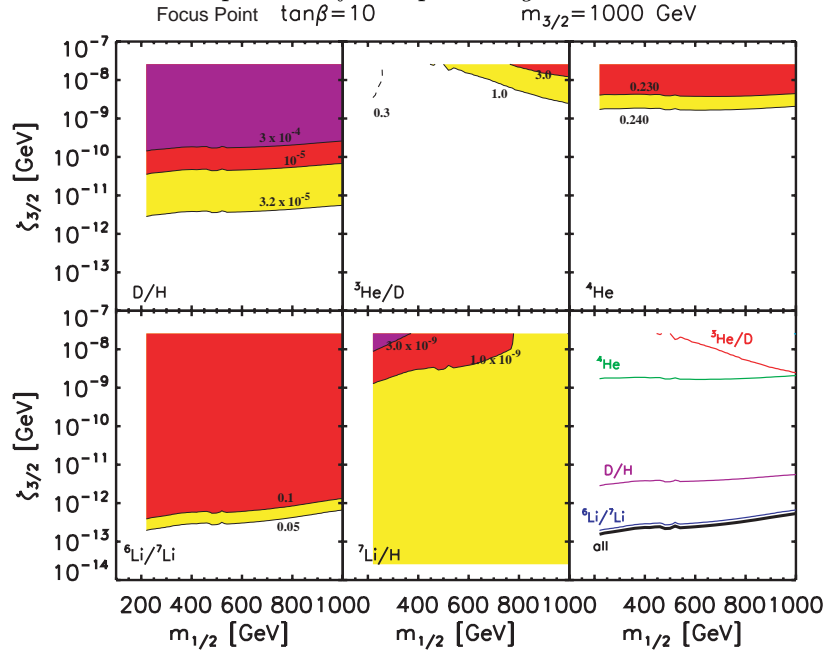


Figure 21: As for Fig. 8, with $m_{3/2} = 1000$ GeV, but $\tan\beta = 10$ and CMSSM parameters appropriate for the WMAP strip in the focus-point region.

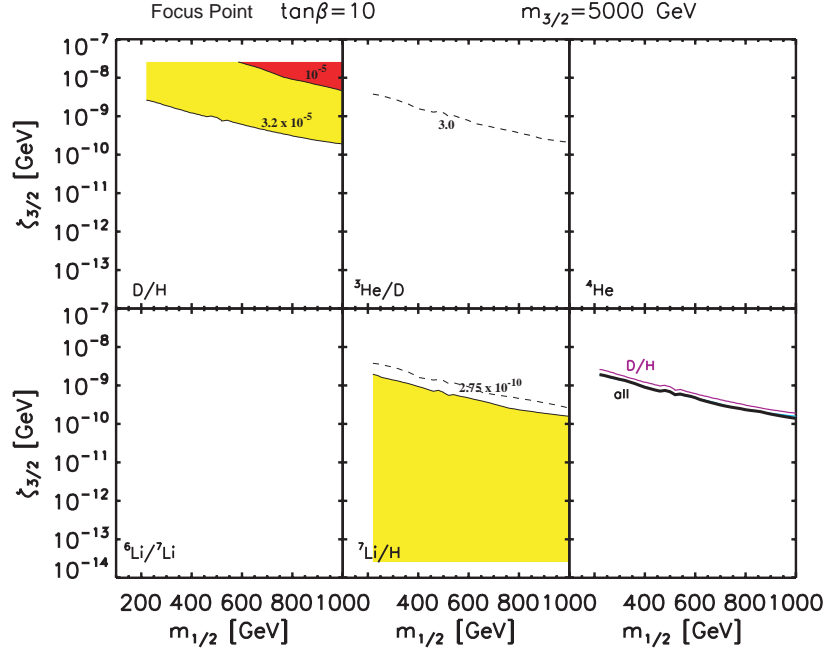


Figure 22: As for Fig. 8, with $m_{3/2} = 5000 \text{ GeV}$, but $\tan\beta = 10$ and CMSSM parameters appropriate for the WMAP strip in the focus-point region.

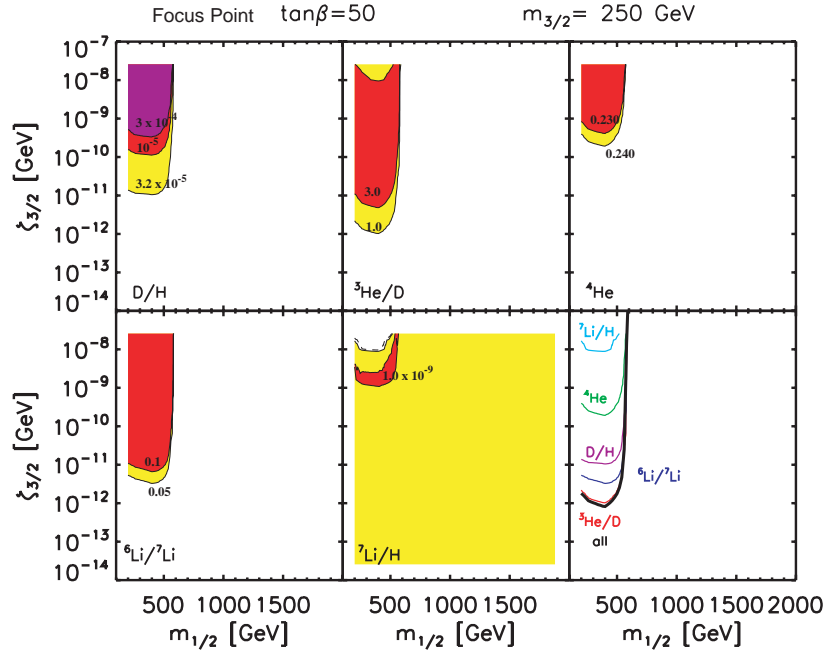


Figure 23: As for Fig. 8, with $m_{3/2} = 250 \text{ GeV}$, but $\tan\beta = 50$ and CMSSM parameters appropriate for the WMAP strip in the focus-point region.

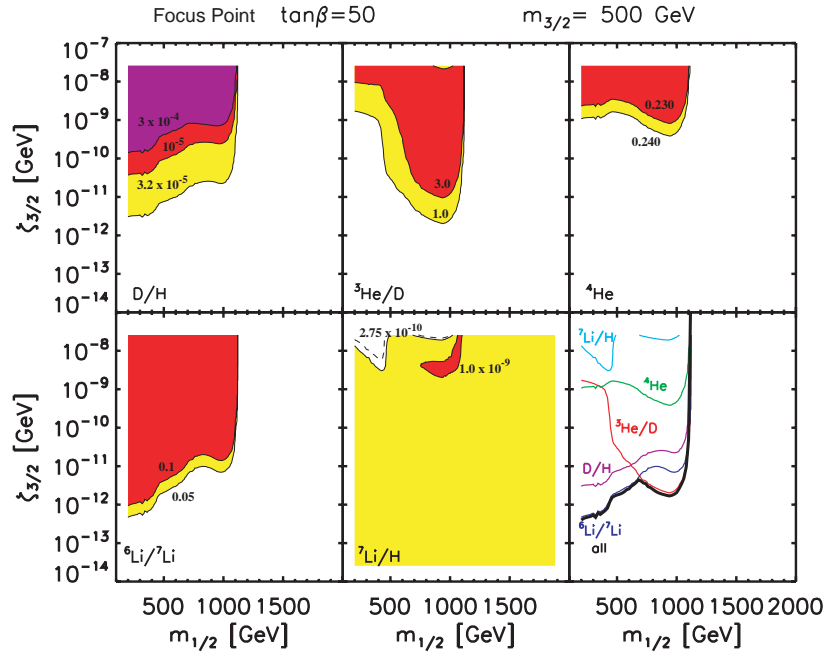


Figure 24: As for Fig. 8, with $m_{3/2} = 500$ GeV, but $\tan\beta = 50$ and CMSSM parameters appropriate for the WMAP strip in the focus-point region.

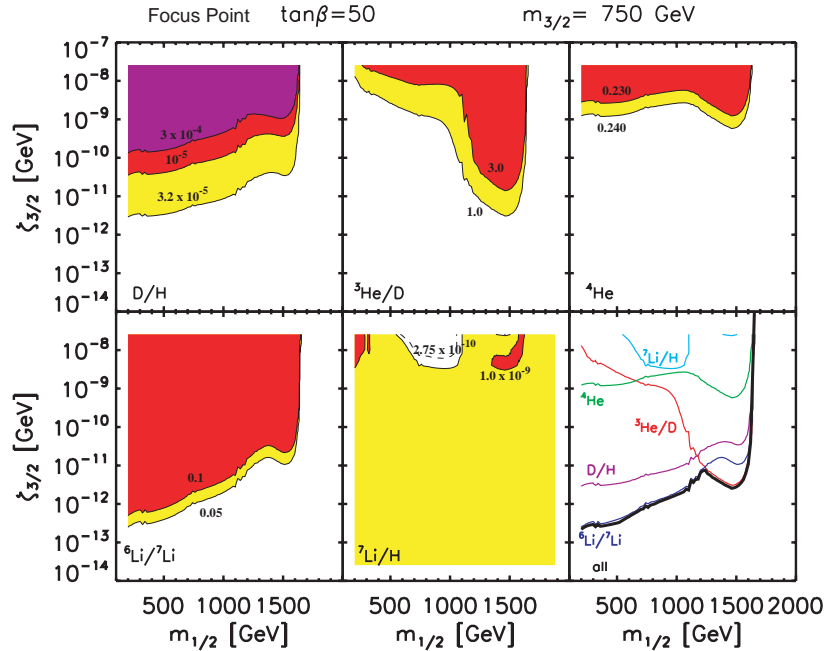


Figure 25: As for Fig. 8, with $m_{3/2} = 750$ GeV, but $\tan\beta = 50$ and CMSSM parameters appropriate for the WMAP strip in the focus-point region.

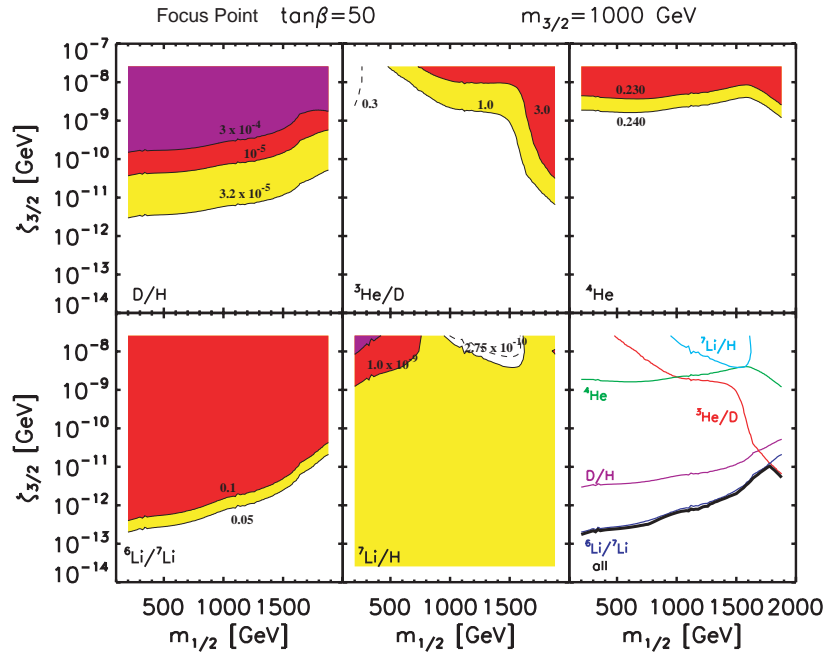


Figure 26: As for Fig. 8, with $m_{3/2} = 1000$ GeV, but $\tan\beta = 50$ and CMSSM parameters appropriate for the WMAP strip in the focus-point region.

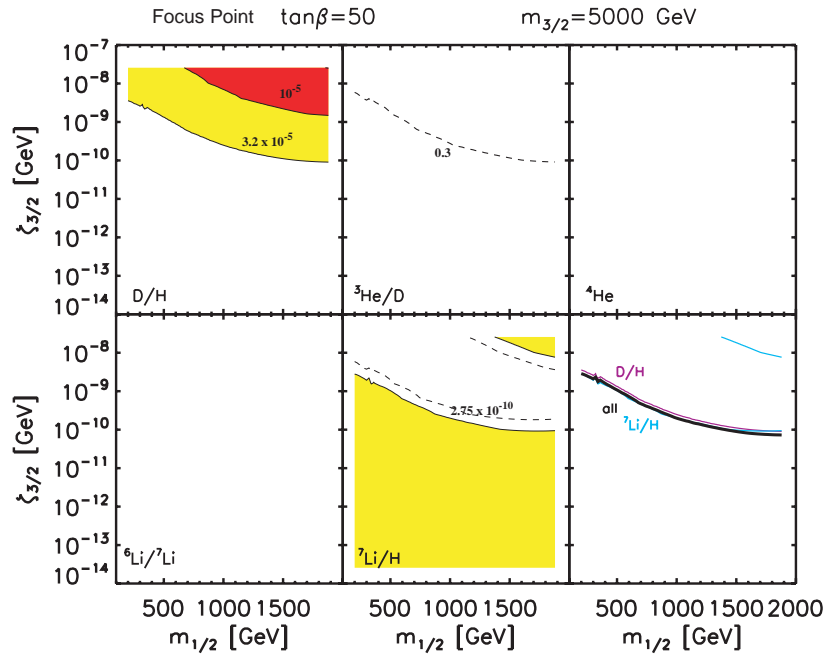


Figure 27: As for Fig. 8, with $m_{3/2} = 5000$ GeV, but $\tan\beta = 50$ and CMSSM parameters appropriate for the WMAP strip in the focus-point region.

5.4 Varying $m_{3/2}$ and the ${}^7\text{Li}$ Problem

The previous plots displayed the gravitino constraints along WMAP strips in the $(m_{1/2}, m_0)$ planes for a few discrete choices of $m_{3/2}$. We now display some results as continuous functions of $m_{3/2}$ for a few WMAP-compatible points with certain discrete values of $m_{1/2}$. Fig. 28 shows our first choice, $m_{1/2} = 400$ GeV and $\tan\beta = 10$, in which case the WMAP point is essentially benchmark point C defined in [47]. As expected from the previous figures, we see that the other light-element constraints are incompatible with the ${}^7\text{Li}/\text{H}$ constraint for low $m_{3/2}$. Disregarding the ${}^7\text{Li}$ problem, we find, e.g., an upper limit on $\zeta_{3/2} \sim 10^{-13}$ when $m_{3/2} \sim 1.4$ TeV. However, marginal compatibility with the cosmological ${}^7\text{Li}$ abundance is approached for $m_{3/2} \gtrsim 3$ TeV with $\zeta_{3/2} > 10^{-11}$ GeV, as was to be expected from Fig. 12. This is a realization within the CMSSM of the marginal compatibility between the ${}^7\text{Li}$ abundance and the D/H ratio that was noted earlier in the context of Fig. 4.

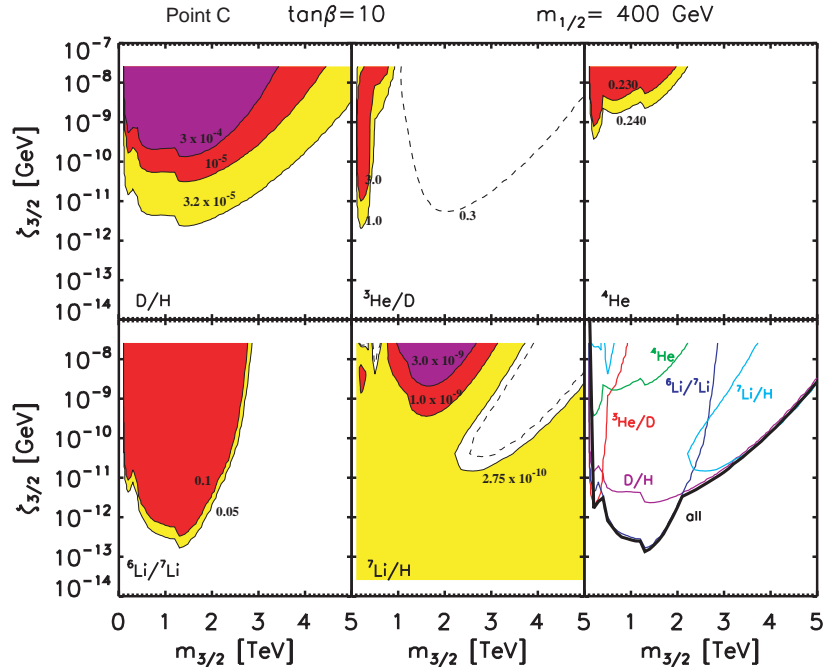


Figure 28: *The effects of the decays of a gravitino with variable mass $m_{3/2}$ on the different light-element abundances for a specific point (benchmark C) with $m_{1/2} = 400$ GeV on the WMAP coannihilation strip for a CMSSM scenario with $\tan\beta = 10$, $A_0 = 0$. As in previous figures, the white regions in each panel are those allowed at face value by the light-element abundances reviewed in Section 2.1, and the yellow, red, and magenta regions correspond to progressively larger deviations from the central values of the abundances. We see marginal compatibility between the ${}^7\text{Li}$ constraint (light blue) and the other constraints for $m_{3/2} \gtrsim 3$ TeV.*

Figs 29, 30 and 31 display similar features for other choices of WMAP-compatible benchmark points [47]. In the case of Fig. 29, we choose benchmark point L with $m_{1/2} = 460$ GeV and $\tan\beta = 50$, which is also in a coannihilation strip. We see very similar features to Fig. 28, e.g., an upper limit on $\zeta_{3/2} \sim 2 \times 10^{-13}$ GeV when $m_{3/2} \sim 1.6$ TeV if the ${}^7\text{Li}$ constraint is disregarded, and a marginal solution of the ${}^7\text{Li}$ problem for $m_{3/2} \gtrsim 3$ TeV with $\zeta_{3/2} > 10^{-11}$ GeV. Fig. 30 is based on benchmark point M with $m_{1/2} = 1840$ GeV and $\tan\beta = 50$, which is in a rapid-annihilation funnel. The features seen in the previous figures shift to higher $m_{3/2}$, e.g., we see an upper limit on $\zeta_{3/2} \sim 10^{-12}$ GeV when $m_{3/2} \sim 2.4$ TeV if the ${}^7\text{Li}$ constraint is disregarded, and a marginal solution of the ${}^7\text{Li}$ problem for $m_{3/2} \gtrsim 4$ TeV with $\zeta_{3/2} > 5 \times 10^{-11}$ GeV. Finally, Fig. 31 is based on benchmark point E with $m_{1/2} = 300$ GeV and $\tan\beta = 10$, which is in a focus-point region. We see in general results that are very similar to those for benchmark point C shown in Fig. 28.

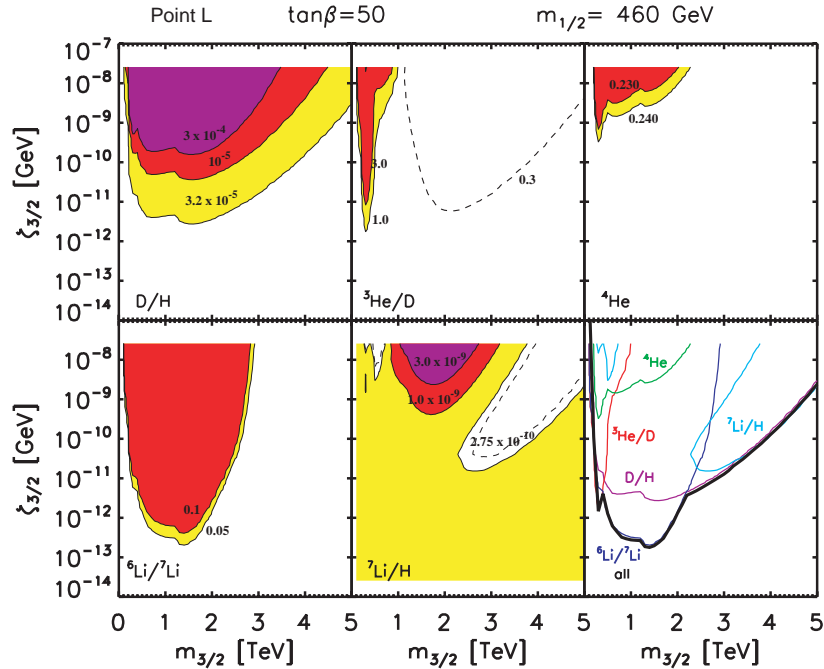


Figure 29: As for Fig. 28, for CMSSM benchmark point L with $m_{1/2} = 460$ GeV and $\tan\beta = 50$, on the WMAP strip in the coannihilation region.

The stability of the marginal “solution” of the ${}^7\text{Li}$ problem reflects the fact that the gravitino lifetime $\sim 10^2 - 10^3$ s and the number of nucleons per decay are relatively stable for heavy gravitino masses as $m_{1/2}$ and $\tan\beta$ are varied: see Figs 1 and 3. The underlying physics of this marginal “solution”, as discussed in [21,22], is that for this range of gravitino lifetimes, thermalized neutrons can destroy ${}^7\text{Be}$ via ${}^7\text{Be}(n,p){}^7\text{Li}$, following which ${}^7\text{Li}$ is destroyed by

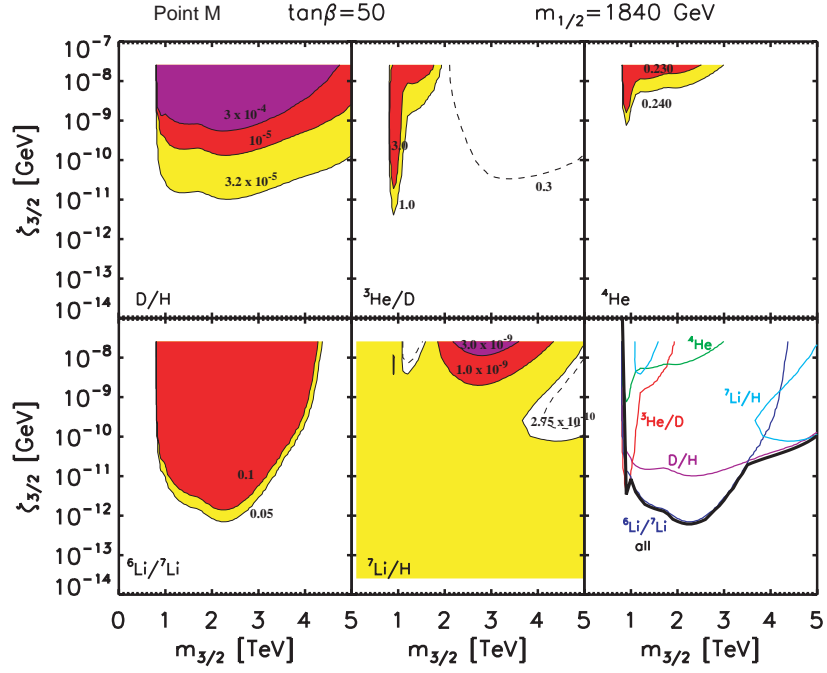


Figure 30: As for Fig. 28, for CMSSM benchmark point M with $m_{1/2} = 1840$ GeV and $\tan\beta = 50$, on the WMAP strip in the rapid-annihilation funnel region.

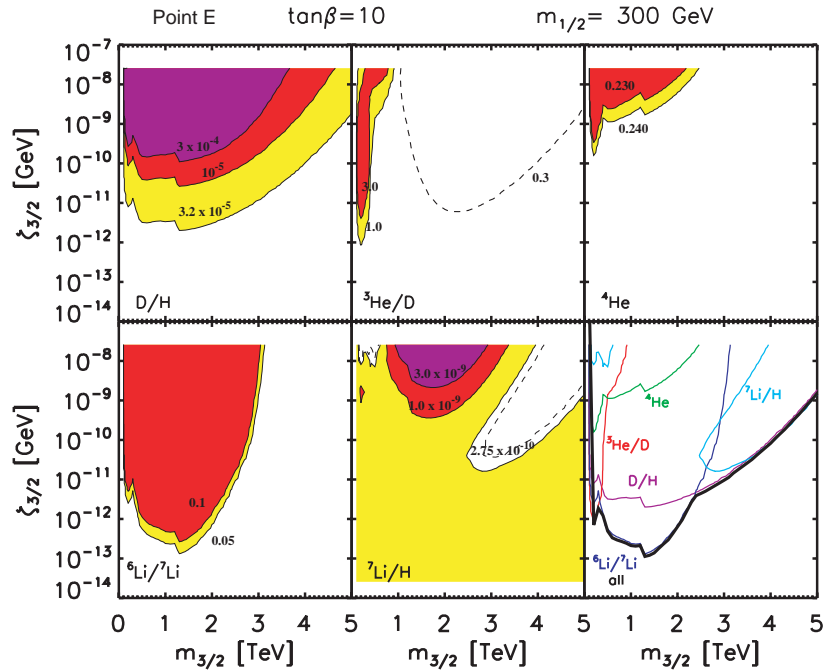


Figure 31: As for Fig. 28, for CMSSM benchmark point E with $m_{1/2} = 300$ GeV and $\tan\beta = 10$, on the WMAP strip in the focus-point region.

the ${}^7\text{Li}(p, \alpha){}^4\text{He}$ reaction. Here, as discussed in Appendix A, we also allow for supplementary ${}^7\text{Be}$ destruction by non-thermalized neutrons.

6 Conclusions

The first objective of this paper has been to document a new suite of codes for the development of non-thermal particle showers in the early universe. These codes treat both electromagnetic and hadronic components of showers, and can be applied to the decays of unstable particles within a wide range of possible lifetimes, that may decay either during or subsequent to standard BBN. We have also shown how this suite of codes may be used to analyze the possible effects of generic particles with typical decay modes.

As a specific application of this suite of codes, we have re-examined the cosmological constraints on unstable gravitinos in R -conserving CMSSM scenarios with a neutralino LSP arising from their effects on the light-element abundances. The first step in this re-examination was the recalculation of some two-body gravitino decay modes and the calculation of some important three-body decay modes. The next step was the simulation of the electromagnetic and hadronic products of these decays using PYTHIA. We have then used our new suite of codes to simulate the interactions of these decay products with the cosmological plasma, including both energy losses and interactions with the nuclei of light elements that affect their abundances. Generally, we find that details of the decay spectra are less important than the overall fractions of baryons produced in the gravitino decays. These fractions are model-dependent, and vary considerably with the gravitino mass and the CMSSM parameters. In addition to the baryon fractions, the constraints on the gravitino abundance inferred from the observed light-element abundances depend sensitively on the gravitino lifetime, and are generally weaker in scenarios with a shorter-lived gravitino.

For $m_{3/2} < 3$ TeV, none of the CMSSM scenarios we study solves the cosmological ${}^7\text{Li}$ problem. Accordingly, one must either reject these CMSSM scenarios, or re-evaluate the observational data on ${}^7\text{Li}$, or postulate some other mechanism for bringing the ${}^7\text{Li}$ abundance into line with standard BBN predictions, or find some way to modify these predictions. Setting the ${}^7\text{Li}$ problem aside, we find that the strongest constraints are usually those imposed by the ${}^6\text{Li}/{}^7\text{Li}$ ratio, with weaker limits coming from the D/H, ${}^3\text{He}/\text{D}$ and ${}^4\text{He}$ constraints. We have evaluated these constraints along WMAP strips in the $(m_{1/2}, m_0)$ plane where the relic neutralino density falls within the expected range for cold dark matter, for $m_{3/2} = 250, 500, 750, 1000$ and 5000 GeV, $A_0 = 0$ and two representative choices $\tan\beta = 10, 50$. There are two strips for each choice of $\tan\beta$: one in the coannihilation and

funnel region, and one in the focus-point region.

We find that the upper limits on $\zeta_{3/2} = m_{3/2}n_{3/2}/n_\gamma$ are quite similar along these WMAP strips, that they weaken as $m_{1/2}$ increases for fixed $m_{3/2}$ (particularly for $\tan\beta = 50$), that they strengthen by about an order of magnitude as $m_{3/2}$ increases from 250 GeV towards 1000 GeV, and that the constraints are significantly weaker for $m_{3/2} = 5000$ GeV. The constraints also weaken considerably as the neutralino mass approaches $m_{3/2}$ from below, as the phase space for gravitino decay disappears. For larger values of $m_{1/2}$, the neutralino is no longer the LSP, and the WMAP strips are inapplicable.

Extending these studies to larger $m_{3/2}$, we find that the D/H and ${}^7\text{Li}/\text{H}$ constraints may become marginally compatible for $m_{3/2} \gtrsim 3$ TeV and a very narrow range of gravitino abundance that increases with $m_{3/2}$. In this region, both thermal and non-thermal neutrons destroy ${}^7\text{Be}$ via the ${}^7\text{Be}(n,p){}^7\text{Li}$ reaction, which is followed by ${}^7\text{Li}$ destroyed via the ${}^7\text{Li}(p,\alpha){}^4\text{He}$ reaction [21, 22] for a finely-tuned range of lifetimes around $\tau_X \sim 10^3$ sec. We use here the recently updated ${}^3\text{He}(\alpha,\gamma){}^7\text{Be}$ rate [99] which makes the ${}^7\text{Li}$ problem worse, since it requires ${}^7\text{Be}$ destruction by a larger factor. We find that the competing upward perturbations to D/H and ${}^3\text{He}/\text{D}$ drive these species away from their observed levels in the regimes where the ${}^7\text{Li}$ problem is solved. This highlights the continued importance of the nuclear reaction data, particularly at energies beyond the $\lesssim 1$ MeV range important for standard, thermal BBN reactions. Additional data extending from ~ 3 MeV to higher energies ~ 30 MeV are urgently needed, particularly for reactions such as ${}^3\text{He}(\alpha,\gamma){}^7\text{Be}$, and for ${}^7\text{Be} + n \rightarrow \text{anything}$. Further studies of both the light-element abundances as well as the relevant nuclear reactions is required in order to verify whether this possible “solution” to the ${}^7\text{Li}$ problem is viable and, if so, how finely one must tune the gravitino abundance within the CMSSM.

The extension of this analysis to the case of a gravitino LSP depends on the nature of the NLSP. If the NLSP is neutral, much of the suite of codes developed here would be directly applicable. On the other hand, if the NLSP is charged, e.g., the lighter stau or some other slepton, it may form electromagnetic bound states before decaying, and catalyze nuclear interactions that are not included in the codes developed here. We will return to this issue in a future publication.

Acknowledgments

We would like to thank M. Pospelov and M. Voloshin for helpful discussions. The work of R.H.C. was supported by the U.S. National Science Foundation Grants No. PHY-01-

10253 (NSCL) and Nos. PHY-02-016783 and PHY-08-22648 (JINA). B.D.F. is grateful to acknowledge the hospitality of CERN TH group, and of the NASA Goddard Space Flight Center, where some of this work was completed. The work of K.A.O. and F.L. is supported in part by DOE grant DE-FG02-94ER-40823 at the University of Minnesota. The work of V.C.S. was supported by Marie Curie International Reintegration grant SUSYDM-PHEN, MIRG-CT-2007-203189 and Marie Curie Excellence grant MEXT-CT-2004-014297.

Appendices

A Propagation of Non-Thermalized Particles in the Cosmic Plasma

We wish to find the non-thermal spectra N_h which are solutions of the propagation equation (16). As discussed in Section 3.2, the equation is self-regulating, with N_h adjusting itself so that sources come into equilibrium with sinks, and hence that $\partial_t N_h = 0$. In this case, the equation we wish to solve is

$$J_h(\epsilon) - \Gamma_h(\epsilon)N_h(\epsilon) - \partial_\epsilon [b_h(\epsilon)N_h(\epsilon)] = 0. \quad (\text{A-1})$$

The sink term has two contributions, due to elastic and inelastic scattering:

$$\Gamma_h(\epsilon) = \sum_b n_b [\sigma v]_{hb \rightarrow h}(\epsilon) + \sum_{h' \neq h, b} n_b [\sigma v]_{hb \rightarrow h'}(\epsilon). \quad (\text{A-2})$$

The source term has three contributions, due to direct injection, elastic down-scattering and inelastic down-scattering, respectively, given by:

$$\begin{aligned} J_h(\epsilon) &= J_{X,h}(\epsilon) + J_{\text{elastic},h}(\epsilon) + J_{\text{inelastic},h}(\epsilon) \\ &= \Gamma_X Q_h(\epsilon) + \sum_b n_b \int_\epsilon^\infty N_h \frac{d[\sigma v]_{hb \rightarrow h}(\epsilon', \epsilon)}{d\epsilon} d\epsilon' \\ &\quad + \sum_{h' \neq h, b} n_b \int_\epsilon^\infty N_{h'} \frac{d[\sigma v]_{h'b \rightarrow h}(\epsilon', \epsilon)}{d\epsilon} d\epsilon', \end{aligned} \quad (\text{A-3})$$

where $Q_h(\epsilon)$ gives the number of hadron of type h per X decay as discussed in Section 3, so that $J_{X,h} = \Gamma_X Q_h$ gives the h injection rate per X particle. The second term in eq. (A-3) gives the rate at which h particles at energy ϵ are produced by elastic scatterings of other h particles, integrated over initial energies ϵ' . The third term in eq. (A-3) gives the rate at which h particles at energy ϵ are produced via inelastic processes $h'b \rightarrow h$, integrated over

initial energies ϵ' . Note that the elastic and inelastic sources in eq. (A-3) are both integrals over proton and neutron spectra N_p and N_n . Thus, in the cascade equation eq. (16), there is one factor of a hadronic spectrum N_h in every term except the decay injection term. Thus, on dividing the cascade equation by Γ_X , one infers an equation for $\tilde{N}_h = N_h/\Gamma_X$ which has the same energy losses and scattering sources and sinks, but whose decay injection term is $Q_h(\epsilon)$, which is independent of Γ_X . In other words, we find that the physical spectrum depends in the following way on the decay properties: $N_h(\epsilon) = \Gamma_X \tilde{N}_h(\epsilon)$, i.e., the scaling separates $N_h(\epsilon)$ into two factors: the X decay rate, and the branching and spectral shapes of the h daughters.

We now look at each of the source terms in detail.

A.1 Elastic- and Inelastic-Scattering Terms

Hadronic processes are described in (A-2) and (A-3) by the differential cross section $d\sigma_{h_i b \rightarrow h_j}(\epsilon_i, \epsilon_j)/d\epsilon_j$ for hadron h_i with energy ϵ_i to produce h_j with energy ϵ_j . The corresponding total cross section for the process is

$$\sigma_{h_i b \rightarrow h_j}(\epsilon_i) = \int d\epsilon_j d\sigma_{h_i b \rightarrow h_j}(\epsilon_i, \epsilon_j)/d\epsilon_j. \quad (\text{A-4})$$

We find it useful to split the collisional loss terms into the rates for inelastic collisions with background nuclei: $\lambda_h^{\text{inel}} = \sum_b n_b \sigma_{hb}^{\text{inel}}(\epsilon)$ and elastic collisions: $\lambda_h^{\text{el}} = \sum_b n_b \sigma_{hb \rightarrow hb}(\epsilon)$, where h loses energy. Similarly, we have divided the source terms into a double sum over all inelastic processes $j_{\text{shower}} k_{\text{bg}} \rightarrow i$ and a sum over elastic scatterings.

The kinematics of the final state particles are treated as in [22].

A.2 Energy Losses

A decay particle loses energy not only loses discontinuously (in time and in energy space) through two-body scatterings, but also continuously (in time and energy space) through collective electromagnetic interactions with the background plasma. These are the analogs of the usual ionization energy losses of particles in laboratory matter, but modified to reflect the fully-ionized state of the thermal plasma in the early universe. The collective interactions amount to a sum of soft, long-range two-body interactions with the surrounding particles, which occur out to some screening radius. As a result, the energy-loss rates are linearly proportional to the density of the background species in question, and to the electromagnetic coupling for the interaction in question.

Table 2: *Nuclear reactions used in this analysis.*

Reactions used in non-thermal propagation	
Reaction	Reference
$NN \rightarrow NN$ (elastic)	Kawasaki et al. [22]
$NN \rightarrow NN$ (total)	Kawasaki et al. [22]
$p^4\text{He} \rightarrow p^4\text{He}$ (elastic)	Meyer [100]
$n^4\text{He} \rightarrow p^4\text{He}$ (elastic)	Meyer [100]
$np \rightarrow$ (inelastic)	Meyer [100]; Ando, Cyburt, Hong, and Hyun [101]
$p^4\text{He} \rightarrow$ (inelastic)	Meyer [100]
$p^4\text{He} \rightarrow d^3\text{He}$	Meyer [100]
$p^4\text{He} \rightarrow np^3\text{He}$	Meyer [100]
$p^4\text{He} \rightarrow ddp$	Meyer [100]
$p^4\text{He} \rightarrow dnpp$	Meyer [100]
$p^4\text{He} \rightarrow nnppp$	Meyer [100]
$p^4\text{He} \rightarrow N^4\text{He}\pi$	Meyer [100]
$n^4\text{He} \rightarrow$ (inelastic)	Meyer [100]
$n^4\text{He} \rightarrow npt$	Meyer [100]
$n^4\text{He} \rightarrow ddn$	Meyer [100]
$n^4\text{He} \rightarrow dnnp$	Meyer [100]
$n^4\text{He} \rightarrow nnppp$	Meyer [100]
$n^4\text{He} \rightarrow N^4\text{He}\pi$	Meyer [100]

Additional reactions with background nuclides	
Reaction	Reference
$pn \rightarrow d\gamma$	Ando, Cyburt, Hong, and Hyun [101]
$pd \rightarrow$ (inelastic)	Kawasaki et al. [22]
$pd \rightarrow {}^3\text{He}\gamma$	Cyburt et al. [20]
$pt \rightarrow n^3\text{He}$	Cyburt [5]
$pt \rightarrow$ (inelastic)	Kawasaki et al. [22]
$p^3\text{He} \rightarrow$ (inelastic)	Kawasaki et al. [22]
$p^6\text{Li} \rightarrow {}^7\text{Be}\gamma$	Cyburt et al. [20]
$p^7\text{Li} \rightarrow {}^4\text{He}^4\text{He}\gamma$	Cyburt [5]
$p^7\text{Be} \rightarrow {}^8\text{B}\gamma$	this work
$d^4\text{He} \rightarrow {}^6\text{Li}\gamma$	Mohr [102]
$t^4\text{He} \rightarrow {}^6\text{Li}n$	Cyburt et al. [20]
$t^4\text{He} \rightarrow {}^7\text{Li}\gamma$	Cyburt [5]
${}^3\text{He}^4\text{He} \rightarrow {}^6\text{Li}p$	Cyburt et al. [20]
${}^3\text{He}^4\text{He} \rightarrow {}^7\text{Be}\gamma$	Cyburt and Davids [99]
$nd \rightarrow$ (inelastic)	Kawasaki et al. [22]
$nd \rightarrow t\gamma$	Cyburt et al. [20]
$nt \rightarrow$ (inelastic)	Kawasaki et al. [22]
$n^3\text{He} \rightarrow$ (inelastic)	Kawasaki et al. [22]
$n^6\text{Li} \rightarrow {}^7\text{Li}\gamma$	Cyburt et al. [20]

Thus, the energy-loss rate $b_h(\epsilon) = -(d\epsilon_h/dt)_{\text{background}}$ of hadron species h sums over the non-thermal particle's electromagnetic interactions with the background plasma:

$$b_h(\epsilon) = b_{h,e}(\epsilon) + b_{h,\gamma}(\epsilon) + b_{h,\text{pair}}(\epsilon), \quad (\text{A-5})$$

where the terms account for interactions with background electrons, positrons and photons, as well as pair-production. Before going into the details of the energy dependences of these terms, some general effects are important to note.

The dominant electromagnetic losses for both protons and neutrons are due to interaction with the background electrons and positrons, which are the most mobile and abundant charged species. Consequently, the key loss rates are proportional to the total number density $n_{e,\text{tot}} = n_{e^-} + n_{e^+}$ of background electrons and positrons, itself set by the plasma temperature and the excess $n_{e,\text{net}} = n_{e^-} - n_{e^+} = \langle Z \rangle_B n_B \approx (Y_{\text{proton}} + 2Y_{4\text{He}})n_B$ of electrons over positrons required by charge balance with background protons and nuclei. As the universe undergoes pair annihilation, the electron/positron abundance and thus the electromagnetic losses change drastically, and pass through three regimes [103]. At $T \gtrsim m_e$, pairs are relativistic and have numbers comparable to photons: $n_{e,\text{tot}} \approx 3n_\gamma/2 \gg n_{e,\text{net}}$. At $m_e \gtrsim T \gtrsim m_e/25$, electrons are nonrelativistic but pairs remain much more abundant than baryons, though less than photons, with $n_{e,\text{tot}} \approx \sqrt{n_{e,\text{net}}^2 + (2n_{e^+})^2}$ and $n_{e^+} = 2(m_e T/2\pi)^{3/2} e^{-m_e/T}$. At $T \lesssim m_e/25$, pairs are nonrelativistic, the positron density is vanishingly small, and the electron density is set by charge balance: $n_{e,\text{tot}} = n_{e,\text{net}}$.

Non-thermal ions suffer all of the losses represented by the terms of eq. (A-5), while neutrons see only the term that accounts for interactions via their magnetic moment. A consequence of this distinction is that charged decay hadrons have a qualitatively different energy-loss behavior from that of neutrons; we thus discuss the two cases separately.

For non-thermal ions, the dominant energy losses are due to Coulomb interactions with the background electrons and positrons. Such losses of fast ions in plasmas have a large literature of dedicated study [104–106] in addition to calculations made in support of early-universe applications [11, 27]. Following the general approach of [105], we write Coulomb losses for an ion with energy γM and charge Z in the form

$$b_{h,e} = - \left(\frac{d\epsilon_h}{dt} \right)_{\text{Coulomb}} \equiv \frac{Z^2 e^2 \omega_p^2}{v} B(\gamma), \quad (\text{A-6})$$

where ω_p is the plasma frequency for non-relativistic electrons:

$$\omega_p^2 = \frac{4\pi e^2 n_e}{m_e} \Big|_{\text{cgs}} = \frac{4\pi \alpha \hbar c n_e}{m_e c^2}. \quad (\text{A-7})$$

For a relativistic electron plasma, where $T_e > m_e$, then [104, 105]

$$\omega_{\text{p,rel}}^2 \rightarrow \frac{4\pi e^2 n_e}{3kT_e} = \frac{m_e}{3T_e} (\omega_{\text{p}}^{\text{nonrel}})^2. \quad (\text{A-8})$$

The dimensionless function $B(v)$ or $B(\gamma)$ encodes the effects of different physical regimes. We are interested in various limits, specifically ion speed $v \sim 1$ versus $v \ll 1$, and relativistic $T_e \gg m_e$ versus non-relativistic $T_e \ll m_e$ plasmas. The B function generally features a Coulomb logarithm, which is roughly $\Lambda \sim \ln(q_{\text{max}}/q_{\text{min}})$, where q is the momentum transfer from the fast particle to a plasma electron. For example, in the non-relativistic case, $q_{\text{max}} \sim 2m_e\gamma v$, and $q_{\text{min}} \sim \hbar\omega_p/v$, so that $\Lambda \sim \ln(2m_e\gamma v^2/\hbar\omega_p)$. Then, for $T_e \ll m_e$, i.e., $n_e \ll T_e^3$, we put

$$B(\gamma) = \ln\left(\frac{2\gamma m_e v^2}{\hbar\omega_p}\right) \left[\text{erf}\left(\frac{v}{v_T}\right) - \frac{2}{\sqrt{\pi}} \frac{v}{v_T} \left(1 + \frac{m}{M}\right) e^{-(v/v_T)^2} \right], \quad (\text{A-9})$$

where $v_T^2 = 2T_e/m_e$. The term in square brackets $\rightarrow 1$ for relativistic nuclides, but gives the appropriate reduction in losses for non-relativistic particles.

At high energies $\gtrsim 1$ GeV, two other loss mechanisms are important, and our treatment here closely follows that of [22]. Photo-pair production, e.g., $p\gamma \rightarrow pe^+e^-$, becomes important for $\epsilon_p \gtrsim 3$ GeV ($T/0.1$ MeV) [107]. We include this using the procedure outlined in [108]. Energy losses due to photopion production, e.g., $p\gamma \rightarrow p\pi^0$, become important at energies $\epsilon_p \gtrsim 500$ GeV ($T/0.1$ MeV). We include these following [109].

For neutrons, Coulomb scattering is of course absent, but magnetic-moment interactions with the ambient radiation background do act to slow the non-thermal neutrons [11, 110]. We adopt the loss rate of [111]:

$$b_n = -\frac{d\epsilon_n}{dt} = \frac{2\pi e^4 g_n^2 n_e}{m_e} \left(\frac{m_e}{m_n}\right)^2 v^2 (1 - v^2) \gamma^2, \quad (\text{A-10})$$

where m_n is the neutron mass and $g_n = -1.91$ is the magnetic moment of the neutron in units of the nuclear magneton. This expression is similar to the result of [27], except that the latter has a numerical prefactor $3/2$ compared to that in eq. (A-10) and omits the factor $(1 + v^2)$. These differences are not dramatic, and for mildly relativistic speeds these factors compensate to give very similar loss rates.

A.3 Solution of the Propagation Equation

All the non-thermal species h evolve according to cascade equations of the form (16), and together these constitute a coupled set of partial differential equations (PDEs) in energy and

time. Because the source term includes the elastic term with N_h inside the integral, these equations are of integro-differential form.

Fortunately, major simplifications occur due to the hierarchy of timescales in the problem. The equation is self-regulating, and the timescale to reach quasi-steady equilibrium is much faster than the decay time or the expansion timescale. Hence one can treat the spectrum as quasi-steady, so that the coupled PDEs in energy and time become coupled ordinary differential equations (ODEs) at each time step, a great simplification. Moreover, redshift and expansion effects can safely be ignored.

Despite these considerable improvements, the equation is still of integro-differential form, and the integration is therefore not immediate. We follow the usual procedure to solve such integral equations, namely iteration. We begin with a zeroth-order approximate solution, in which we neglect the elastic and inelastic source terms. In this approximation, eq. (16) becomes

$$\partial_t N_h(\epsilon) = J_{X,h}(\epsilon) - \Gamma_h(\epsilon)N_h(\epsilon) - \partial_\epsilon(b_h(\epsilon)N_h(\epsilon)). \quad (\text{A-11})$$

For secondary nuclear species not present in the original decays, (i.e., all but nucleons), the solution of eq. (A-11) can be written in terms of the following quadrature

$$N_h(\epsilon, t) = \frac{1}{b(\epsilon)} \int_\epsilon^\infty d\epsilon' J_{X,h}(\epsilon', t) e^{-\tau(\epsilon', t)}, \quad (\text{A-12})$$

where the exponential ‘‘optical depth’’ factor

$$\tau(\epsilon', t) = \int_\epsilon^{\epsilon'} d\epsilon'' \frac{\Gamma(\epsilon'', t)}{b(\epsilon'')} \quad (\text{A-13})$$

is a measure of the average number of inelastic interactions over the time taken to lose energy electromagnetically from ϵ' to ϵ . The secondary and tertiary cascades can then be treated iteratively, correcting the initial omission of these terms:

$$N_h^{(0)}(\epsilon, t) = \frac{1}{b_h(\epsilon, t)} \int_\epsilon^\infty d\epsilon' J_{X,h}(\epsilon', t) e^{-\tau(\epsilon', t)}, \quad (\text{A-14})$$

$$N_h^{(1)}(\epsilon, t) = \frac{1}{b_h(\epsilon, t)} \int_\epsilon^\infty d\epsilon' J_h^{(0)}(\epsilon', t) e^{-\tau(\epsilon', t)}, \quad (\text{A-15})$$

$$\vdots \quad (\text{A-16})$$

$$N_h^{(i)}(\epsilon, t) = \frac{1}{b_h(\epsilon, t)} \int_\epsilon^\infty d\epsilon' J_h^{(i-1)}(\epsilon', t) e^{-\tau(\epsilon', t)}, \quad (\text{A-17})$$

where $J_h^{(i)}$ is the source term from eq. (A-3), replacing N_h with $N_h^{(i)}$.

Once these distributions converge, one can insert them into equation (13) and solve for the hadro-dissociation rate. This iterative procedure generalizes the procedure adopted in

some previous studies [22]. Rather than including the exponent in the integral, they treat the exponential R term as a δ function, evaluated at ϵ_* , defined as the energy at which the optical depth is unity: $\tau(\epsilon_*, \epsilon, t) = 1$.

We plot the resulting non-thermal neutron and proton spectra in Fig. 32. The thick solid black curve gives (in arbitrary units) the shape of the source spectra $\epsilon Q_p(\epsilon)$ and $\epsilon Q_n(\epsilon)$. The colored curves give the corresponding propagated spectra for a wide range of cosmic epochs, labeled by the temperature. The highest temperature, $T = 2.5$ MeV, corresponds to the lowest (red) curve, while the lowest temperature, $T = 6 \times 10^{-5}$ MeV, corresponds to the highest (bluegreen) curve in each plot. Note that we plot $\epsilon N_h(\epsilon)/\Gamma_X$: (1) we use the product $\epsilon N_h(\epsilon)$ so that one can best assess the particle number per logarithmic interval; and (2) as noted above in Section 3.3, the propagated spectra are proportional to the decay rate Γ_X , and so by dividing by this factor we remove this dependence.

Most striking in Fig. 32 is the enormous dynamic range in the spectra amplitudes as the cosmic environment evolves. Indeed, the highest and lowest curves in the plots are separated by more than 20 orders of magnitude! This can be understood as a combination of two factors. First, the propagated spectra scale inversely with the cosmic baryon density, either directly via $N_{h,\text{thin}} \propto 1/n_B$ (eq. 20), or indirectly via the density dependence of energy losses, $N_{h,\text{thick}} \propto 1/b \propto 1/Y_{e^\pm} n_B$ (eq. 21). This inverse density dependence leads to the steady rise in the spectral amplitudes at late times. Since the temperature range shown in Fig. 32 varies over a factor $T_{\text{hi}}/T_{\text{low}} = 4 \times 10^4$, the baryon density varies by a factor $(T_{\text{hi}}/T_{\text{low}})^3 = 6 \times 10^{13}$. For neutrons at $\epsilon \lesssim 100$ MeV, the spectra are dominated by thin-target interactions and this factor gives the range over which these spectral amplitudes vary.

It is important to note that while the density changes lead to enhanced spectra amplitudes at low temperatures and densities, the non-thermal interaction rates scale as the product of the non-thermal flux times the density of background targets. This compensating factor of density means that the overall interaction rates do not directly vary with density (though the spectral shapes vary with cosmic epoch).

For neutrons at $\epsilon \gtrsim 100$ MeV, and for protons at all energies, there is an additional evolutionary effect on the spectral amplitudes. Namely, these particles are dominated by thick-target propagation, where the spectral amplitudes are inversely proportional to energy losses which are themselves dependent on the e^\pm density and thus the total lepton per baryon ratio Y_{e^\pm} : $N_{h,\text{thick}} \propto 1/b \propto 1/Y_{e^\pm} n_B$ (eq. 21). Before pair annihilation, pairs are comparable in number to photons, $Y_{e^\pm} \sim Y_\gamma \sim 1/\eta \sim 10^9$; after annihilation is complete, the remaining electrons provide charge balance and thus $Y_{e^\pm} = Y_{e^-} \sim 1$. Thus as pairs annihilate and energy losses are greatly reduced, the propagated spectra rise dramatically. The pair number

changes most when temperature drops from $T \sim 0.1$ MeV down to ~ 0.02 MeV, which leads to the large increases in the neutron spectral amplitudes at $\epsilon \gtrsim 100$ MeV and in the proton amplitudes at all energies. This additional annihilation factor contributes on top of the baryon density effect and leads to the full variation seen in the spectral amplitudes. Note that since the thin-target neutrons are responsible for most of the abundance perturbations, and since we are interested in times $\gtrsim 10^3$ sec, this annihilation effect is not very important for our results, though it is included in all of our calculations.

Beyond the overall spectral amplitudes, the spectral shapes versus energy are set by the combination of the source shape and the energy dependence of the dominant loss curve. For example, in the case of neutrons at $\epsilon \lesssim 100$ MeV, the losses are dominated by inelastic scattering which is nearly energy-independent, and thus the nearly flat source shape $\epsilon Q_n(\epsilon)$ leads to a nearly flat propagated shape. On the other hand, for protons at late times and at $\epsilon \lesssim 1$ GeV, losses are dominated by Coulomb interactions, with $N_p \propto Q_p(> \epsilon)/b_{\text{coul}}$. We have $b_{\text{coul}} \propto 1/v \propto 1/\epsilon^{1/2}$, and for this decay spectrum $Q_p(> \epsilon) \simeq \epsilon Q_p(\epsilon) \sim \text{constant}$. Thus we have $\epsilon N_p(\epsilon) \propto \epsilon^{3/2}$, which is exactly the scaling behavior in Fig. 32 for $\lesssim 1$ GeV protons at late times and low temperatures.

A.4 Rates for Non-Thermal Reactions on Background Light Nuclei

As non-thermal particles propagate in the cosmic plasma they interact with background nuclides and change light element abundances. As shown in eq. (14), the rates for these processes depend on the non-thermal spectra we calculate, but also on the cross sections for the processes. The largest such rates are between the non-thermal nucleons and the most abundant background species—nucleons and ^4He nuclei; these rates are important in determining the non-thermal spectra themselves, and are included in the propagation calculations. Reactions with less abundant background nuclei are neglected in the non-thermal propagation calculations. All of the non-thermal production and rates on background nuclei are evaluated as a function of cosmic time and environment, and are incorporated as additional channels in the usual (thermal) nucleosynthesis code.

Table 2 lists the nuclear reactions we use in our analysis, as well as the references for the cross sections we adopt. We show the reactions used in the propagation calculations as well as in the non-thermal rate evaluations, and reactions only used for non-thermal rates.

Several reactions have been updated since previous studies or were not present. We adopt the recent revised fit to $^3\text{He}(\alpha, \gamma)^7\text{Be}$ from Cyburt and Davids [99]. The cross section

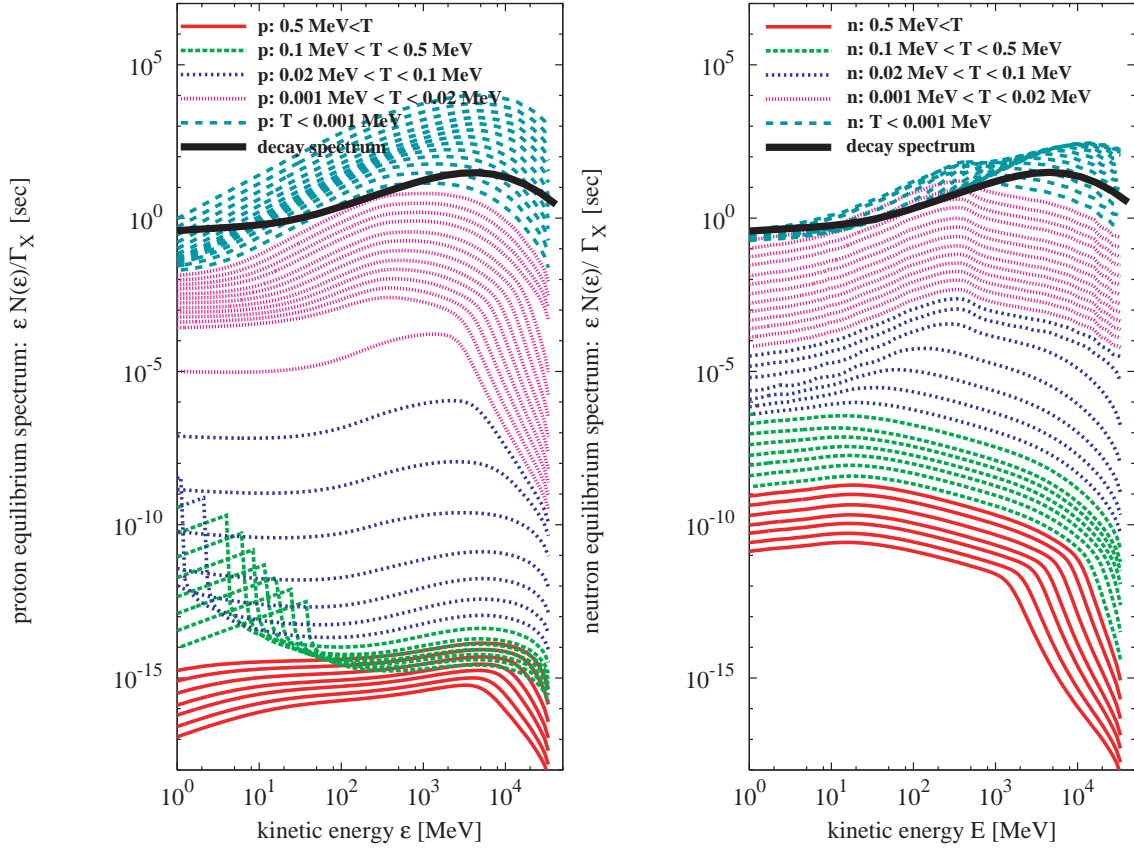


Figure 32: Spectra of non-thermal hadrons after propagation in the cosmic plasma; we plot $\epsilon N_h(\epsilon)$, which indicates the particle number per logarithmic energy interval. Results are shown for a large range of cosmic epochs (i.e., temperatures, densities, background abundances). Propagated spectra scale with the decay rate Γ_X , so we plot N_h/Γ_X . The decay injection spectra are for $(m_{1/2}, m_{3/2}, \tan \beta) = (120\text{GeV}, 500\text{GeV}, 50)$.

is somewhat higher than in previous assessments, leading to larger non-thermal production of ${}^7\text{Be}$ as well as a boosted thermal production and thus a higher standard (unperturbed) BBN value [6]. All else being equal, this change increase worsens the ${}^7\text{Li}$ problem, and also somewhat reduces the ${}^6\text{Li}/{}^7\text{Li}$ ratio at where the ${}^7\text{Li}$ level remains dominated by the primordial production.

We have also added non-thermal reactions not present in our previous treatments, and as far as we are aware, also not present in those of other groups. Namely, we have included new channels for non-thermal $A = 7$ destruction: ${}^7\text{Be}(n, p){}^7\text{Li}$, ${}^7\text{Be}(n, \alpha){}^4\text{He}$, and ${}^7\text{Li}(p, \alpha){}^4\text{He}$. Of these, by far the largest cross section is for ${}^7\text{Be}(n, p){}^7\text{Li}$, which as a thermal rate is important in standard BBN. This reaction leads to $A = 7$ reduction when followed by ${}^7\text{Li}(p, \alpha){}^4\text{He}$ which has a reduced Coulomb barrier relative to ${}^7\text{Be} + p$. As noted above (Section 5) and in refs. [21, 22], $A = 7$ destruction via ${}^7\text{Be}(n, p){}^7\text{Li}$ with *thermalized* decay neutrons is responsible for the “valley” of concordant ${}^7\text{Li}/\text{H}$ at lifetimes $10^2 - 10^3$ sec as seen in Fig. 4. It thus is reasonable to include the same process due to *non-thermal* neutrons. In fact, we find that these rates do not appreciably change the final ${}^7\text{Li}/\text{H}$ abundance.

B Gravitino Decay Amplitudes

In calculating the relevant gravitino decay rates, we use the interaction Lagrangian given in [112]:

$$\begin{aligned} \mathcal{L}_{\text{int}} = & -\frac{i}{\sqrt{2}M_P} \left[\mathcal{D}_\mu \phi^{*(C)} \bar{\psi}_\nu \gamma^\mu \gamma^\nu \chi_L^{(C)} - \mathcal{D}_\mu \phi^{(C)} \bar{\chi}_L^{(C)} \gamma^\nu \gamma^\mu \psi_\nu \right] \\ & - \frac{i}{8M_P} \bar{\psi}_\mu [\gamma^\rho, \gamma^\sigma] \gamma^\mu \lambda^{(G)} F_{\rho\sigma}^{(G)}, \end{aligned} \quad (\text{A-18})$$

where ψ_μ is gravitino field, ϕ and χ are chiral matter fields, $F_{\rho\sigma}$ is the field strength of a gauge boson field, and λ is the corresponding gaugino field. We denote $\chi_L = P_L \chi$ and $\bar{\chi}_L = \bar{\chi} P_R$, where P_L and P_R are the usual chiral projectors. The indices (C) and (G) denote chiral and gauge multiplets, respectively, and M_P is the reduced Planck mass defined as $M_P = 1/\sqrt{8\pi G_N}$, where G_N is the Newton gravitational constant. The Feynman rules derived from this Lagrangian are given in Appendix B of [112].

We use the relations

$$\begin{aligned} P_L \tilde{W} &= P_L (V_{11}^* \tilde{\chi}_1 + V_{21}^* \tilde{\chi}_2), \quad P_L \tilde{H} = P_L (V_{12}^* \tilde{\chi}_1 + V_{22}^* \tilde{\chi}_2), \\ P_R \tilde{W} &= P_R (U_{11} \tilde{\chi}_1 + U_{21} \tilde{\chi}_2), \quad P_R \tilde{H} = P_R (U_{12} \tilde{\chi}_1 + U_{22} \tilde{\chi}_2), \end{aligned} \quad (\text{A-19})$$

to transform the interaction-eigenstate charged wino \tilde{W}^+ and charged Higgsino \tilde{H}^+ to the mass-eigenstate charginos $\tilde{\chi}_j^+$, where U and V are the unitary matrices used to diagonalize

the chargino mass matrix. We note that all the fields in the above relations are positively charged. To get the transformation relations for negatively charged conjugate states of the positively charged fields, one needs to exchange U and V in the above relations, e.g.,

$$P_L \tilde{W}^c = P_L (U_{11}^* \tilde{\chi}_1^c + U_{21}^* \tilde{\chi}_2^c). \quad (\text{A-20})$$

For neutralinos, the transformation from the interaction eigenstates $\tilde{H}_{1,2}$, \tilde{W}_3 and \tilde{B} to the neutralino mass eigenstates $\tilde{\chi}_i^0$ is given by the relations

$$\begin{aligned} P_L \tilde{H}_i &= P_L N_{j,i+2}^* \tilde{\chi}_j^0, \quad P_L \tilde{B} = P_L N_{j1}^* \tilde{\chi}_j^0, \quad P_L \tilde{W}_3 = P_L N_{j2}^* \tilde{\chi}_j^0, \\ P_R \tilde{H}_i &= P_R N_{j,i+2} \tilde{\chi}_j^0, \quad P_R \tilde{B} = P_R N_{j1} \tilde{\chi}_j^0, \quad P_R \tilde{W}_3 = P_R N_{j2} \tilde{\chi}_j^0, \end{aligned} \quad (\text{A-21})$$

where the repeated index j is summed over from 1 to 4, and the unitary matrix N diagonalizes the neutralino mass matrix. To obtain the mass eigenstates of the Higgs bosons, we use the relations [113]

$$\begin{aligned} H_2^1 &= H^+ \cos \beta, \quad H_1^2 = H^- \sin \beta, \\ H_1^1 &= v_1 + \frac{1}{\sqrt{2}} (H_1^0 \cos \alpha - H_2^0 \sin \alpha + i H_3^0 \sin \beta), \\ H_2^2 &= v_2 + \frac{1}{\sqrt{2}} (H_1^0 \sin \alpha + H_2^0 \cos \alpha + i H_3^0 \cos \beta), \end{aligned} \quad (\text{A-22})$$

where the H^\pm are the charged Higgs fields, H_1^0 and H_2^0 are the CP-even neutral Higgs fields, and H_3^0 is the CP-odd neutral Higgs field. We denote by v_1 and v_2 the vacuum expectation values of the two neutral Higgs fields, $\tan \beta$ is defined as $\tan \beta = v_2/v_1$, and α is the mixing angle which leads to the two CP-even mass eigenstates. Together with the relation $m_W^2 = \frac{1}{2} g^2 (v_1^2 + v_2^2)$, one gets $v_1 = \frac{\sqrt{2} m_W}{g} \cos \beta$ and $v_2 = \frac{\sqrt{2} m_W}{g} \sin \beta$, where g is the gauge coupling for $SU(2)_L$ and m_W is the mass of the W boson. For squarks and sleptons, we do not consider mixing between generations, and we take into account only left-right mixing for the third generation. This simplification is sufficient within the CMSSM framework we consider. The relation between the mass eigenstates $\tilde{t}_{1,2}$ and the interaction eigenstates $\tilde{t}_{L,R}$ is

$$\begin{pmatrix} \tilde{t}_L \\ \tilde{t}_R \end{pmatrix} = \begin{pmatrix} U_{\tilde{t}1L} & U_{\tilde{t}2L} \\ U_{\tilde{t}1R} & U_{\tilde{t}2R} \end{pmatrix} \begin{pmatrix} \tilde{t}_1 \\ \tilde{t}_2 \end{pmatrix}, \quad (\text{A-23})$$

where the transformation matrix is unitary. There are similar interaction/mass-eigenstate transformations for \tilde{b} and $\tilde{\tau}$. We treat the neutrinos as in the Standard Model, i.e., as massless, purely left-handed neutrinos (and right-handed anti-neutrinos) only. For details of the above transformations, we direct the reader to [113].

We now list the amplitudes for all the two-body gravitino decay channels. We denote by m_b and m_f the masses of the final-state bosons and fermions, respectively. For $\tilde{G} \rightarrow \tilde{\chi}_i^0 \gamma$ and $\tilde{G} \rightarrow \tilde{g} g$, we have:

$$\overline{|\mathcal{M}|^2} = \frac{1}{6 m_{3/2}^2 M_P^2} |B|^2 (3 m_{3/2}^2 + m_f^2) (m_{3/2}^2 - m_f^2)^2, \quad (\text{A-24})$$

where $B = N'_{i1}$ for the $\tilde{\chi}_i^0$ final states, with $N'_{i1} = N_{i1} \cos \theta_W + N_{i2} \sin \theta_W$, and θ_W is the weak mixing angle, and $B = 1$ for the \tilde{g} final state. For $\tilde{G} \rightarrow \tilde{\chi}_j^\pm W^\mp$ and $\tilde{G} \rightarrow \tilde{\chi}_i^0 Z$, we have:

$$\begin{aligned} \overline{|\mathcal{M}|^2} &= \frac{1}{12 m_{3/2}^2 M_P^2} \left\{ 12 (C D + C^* D^*) m_{3/2}^3 m_b^2 m_f \right. \\ &+ (|C|^2 + |D|^2) \left[3 m_{3/2}^6 - m_{3/2}^4 (5 m_f^2 + m_b^2) + m_{3/2}^2 (m_f^4 - m_b^4) + (m_f^2 - m_b^2)^3 \right] \left. \right\} \\ &+ \frac{G^2}{24 m_{3/2}^2 m_b^2 M_P^2} \left\{ \left[m_{3/2}^4 - 2 m_{3/2}^2 (m_f^2 - 5 m_b^2) + (m_f^2 - m_b^2)^2 \right] \right. \\ &\times \left[2 (E F + E^* F^*) m_{3/2} m_f + (|E|^2 + |F|^2) (m_{3/2}^2 + m_f^2 - m_b^2) \right] \left. \right\} \\ &+ \frac{G}{6 m_{3/2} M_P^2} \left\{ (D E^* + E D^* + C F^* + F C^*) \right. \\ &\times \left[-2 m_{3/2}^4 + m_{3/2}^2 (m_f^2 + m_b^2) + (m_f^2 - m_b^2)^2 \right] \\ &\left. - 3 (C E + D F + C^* E^* + D^* F^*) m_{3/2} m_f (m_{3/2}^2 - m_f^2 + m_b^2) \right\}, \quad (\text{A-25}) \end{aligned}$$

where $C = V_{j1}$, $D = U_{j1}$, $E = -v_1 U_{j2}$, $F = -v_2 V_{j2}$ and $G = g$ for the $\tilde{\chi}_j^\pm$ final states; and $C = D = N'_{i2}$, with $N'_{i2} = -N_{i1} \sin \theta_W + N_{i2} \cos \theta_W$, $E = F = \frac{1}{\sqrt{2}} (-v_1 N_{i3} + v_2 N_{i4})$ and $G = g / \cos \theta_W$ for the $\tilde{\chi}_i^0$ final states. In the above expression, the first and second lines come from the gauge part of eq. (A-18) (the second line), the third and fourth lines come from the matter part of eq. (A-18) (the first line), with the gauge bosons coming from the covariant derivative and the Higgs field ϕ taking its vacuum expectation value (see eq. (A-22)), and the fifth and sixth lines come from the interference of these two parts. For $\tilde{G} \rightarrow \tilde{f} f$, $\tilde{G} \rightarrow \tilde{\chi}_j^\pm H^\mp$ and $\tilde{G} \rightarrow \tilde{\chi}_i^0 H_{1,2,3}^0$, we have:

$$\begin{aligned} \overline{|\mathcal{M}|^2} &= \frac{1}{12 m_{3/2}^2 M_P^2} \left[(|H|^2 + |K|^2) (m_{3/2}^2 + m_f^2 - m_b^2) - 2 (H K + H^* K^*) m_{3/2} m_f \right] \\ &\times \left[m_{3/2}^4 - 2 m_{3/2}^2 (m_f^2 + m_b^2) + (m_f^2 - m_b^2)^2 \right], \quad (\text{A-26}) \end{aligned}$$

where $H = K = \frac{1}{\sqrt{2}} (N_{i4} \sin \alpha + N_{i3} \cos \alpha)$ for the H_1^0 final state; $H = K = \frac{1}{\sqrt{2}} (N_{i4} \cos \alpha - N_{i3} \sin \alpha)$ for the H_2^0 final state; $H = -K = \frac{1}{\sqrt{2}} (N_{i4} \cos \beta + N_{i3} \sin \beta)$ for the H_3^0 final state;

$H = U_{j_2} \sin \beta$ and $K = V_{j_2} \cos \beta$ for the H^\pm final state; $H = U_{\tilde{t}_k R}^*$ and $K = U_{\tilde{t}_k L}$ for the \tilde{t}_k final state (and similarly for \tilde{b}_k and $\tilde{\tau}_k$ with their corresponding mixing matrices $U_{\tilde{b}_k}$ and $U_{\tilde{\tau}_k}$, respectively); $H = 0$ and $K = 1$ for all the \tilde{f}_L and $\tilde{\nu}$ final states; and $H = 1$ and $K = 0$ for all the \tilde{f}_R final states. To get the partial widths, one need to multiply (A-26) by the phase-space factor:

$$\frac{N_c}{16 \pi m_{3/2}^3} \sqrt{\left[m_{3/2}^2 - (m_f - m_b)^2 \right] \left[m_{3/2}^2 - (m_f + m_b)^2 \right]}, \quad (\text{A-27})$$

where N_c is the color factor (3 for $q \tilde{q}$ channels, 8 for the $g \tilde{g}$ channel, and 1 otherwise).

The amplitude for the three-body decay $\tilde{G} \rightarrow \tilde{\chi}_i^0 \gamma^* \rightarrow \tilde{\chi}_i^0 q \bar{q}$ is

$$\begin{aligned} |\overline{\mathcal{M}}|^2 &= \frac{g^2 \sin^2 \theta_W Q_q^2}{3 s^2 m_{3/2}^2 M_P^2} \left\{ 4 s m_{\tilde{\chi}_i^0} m_{3/2}^3 (N_{i1}'^2 + N_{i1}^{*2}) (s + 2 m_q^2) \right. \\ &+ |N_{i1}'|^2 \left[3 m_{3/2}^6 (s + 2 m_q^2) + m_{3/2}^4 (-3 s (s + 2 t) + m_{\tilde{\chi}_i^0}^2 (s - 10 m_q^2)) \right] \\ &+ m_{3/2}^2 (6 s m_q^4 + 2 m_q^2 (-3 s (s + 2 t) + 2 s m_{\tilde{\chi}_i^0}^2 + m_{\tilde{\chi}_i^0}^4)) \\ &+ s (s^2 + 8 s t + 6 t^2 - 4 m_{\tilde{\chi}_i^0}^2 (s + 2 t) + 3 m_{\tilde{\chi}_i^0}^4) - (s - m_{\tilde{\chi}_i^0}^2) (2 s m_q^4 - 2 m_q^2 \\ &\left. \times (2 s t + s m_{\tilde{\chi}_i^0}^2 - m_{\tilde{\chi}_i^0}^4) + s (s^2 + 2 s t + 2 t^2 - 2 m_{\tilde{\chi}_i^0}^2 (s + t) + m_{\tilde{\chi}_i^0}^4)) \right] \Big\}, \quad (\text{A-28}) \end{aligned}$$

where s and t are the invariant masses of the $q \bar{q}$ and $q \tilde{\chi}_i^0$ systems, respectively, $m_{\tilde{\chi}_i^0}$ is the mass of the neutralino $\tilde{\chi}_i^0$, where the LSP corresponds to $i = 1$, and $Q_q = 2/3$ or $-1/3$ for the corresponding quarks. The differential decay rate is

$$\frac{d\Gamma}{ds dt} = \frac{N_c}{256 \pi^3 m_{3/2}^3} |\overline{\mathcal{M}}|^2. \quad (\text{A-29})$$

These three-body and two-body analytic expressions were also given in [24] and [42].

For $\tilde{G} \rightarrow \tilde{\chi}_i^0 W^+ W^-$, there are contributions from four generically different diagrams: contact, γ/Z exchange, $\tilde{\chi}_j^\pm$ exchange and H_1^0/H_2^0 exchange diagrams. The amplitude is too long to be listed here, so we just write the matrix elements for each of these diagrams (suppressing the polarization indices):

$$i\mathcal{M}_{\text{contact}} = \frac{i}{4M_P} g \bar{u}(q') (P_R N_{i2} + P_L N_{i2}^*) \gamma^\mu [\gamma_\rho, \gamma_\sigma] \psi_\mu(p) \epsilon^{\rho*}(k) \epsilon^{\sigma*}(k'),$$

$$\begin{aligned} i\mathcal{M}_{\tilde{G} \rightarrow \tilde{\chi}_i^0 \gamma^* \rightarrow \tilde{\chi}_i^0 W^+ W^-} &= \frac{i}{4M_P} \frac{1}{(k + k')^2} g^{\alpha\beta} g \sin \theta_W \bar{u}(q') (P_R N_{i1}' + P_L N_{i1}^{*'}) \gamma^\mu [k^\beta + k'^\beta, \gamma_\alpha] \psi_\mu(p) \\ &\times \left[(2k + k')_\sigma g_{\beta\rho} + (k' - k)_\beta g_{\rho\sigma} - (k + 2k')_\rho g_{\sigma\beta} \right] \epsilon^{\rho*}(k) \epsilon^{\sigma*}(k'), \end{aligned}$$

$$\begin{aligned}
i\mathcal{M}_{\tilde{G} \rightarrow \tilde{\chi}_i^0 Z^* \rightarrow \tilde{\chi}_i^0 W^+ W^-} &= \frac{i}{4M_P} \frac{1}{(k+k')^2 - m_Z^2 + im_Z \Gamma_Z} \left(g^{\alpha\beta} - \frac{(k+k')^\alpha (k+k')^\beta}{m_Z^2} \right) g \cos \theta_W \\
&\times \bar{u}(q') \left\{ (P_R N'_{i2} + P_L N'_{i2}^*) \gamma^\mu [\not{k} + \not{k}', \gamma_\alpha] \right. \\
&+ \left. \frac{\sqrt{2}g}{\cos \theta_W} \left[P_R (-v_1 N_{i3} + v_2 N_{i4}) + P_L (-v_1 N_{i3}^* + v_2 N_{i4}^*) \right] \gamma^\mu \gamma_\alpha \right\} \psi_\mu(p) \\
&\times \left[(2k+k')_\sigma g_{\beta\rho} + (k'-k)_\beta g_{\sigma\rho} - (k+2k')_\rho g_{\beta\sigma} \right] \epsilon^{\rho*}(k) \epsilon^{\sigma*}(k'),
\end{aligned}$$

$$\begin{aligned}
i\mathcal{M}_{\tilde{G} \rightarrow W^+ \tilde{\chi}_j^{+*} \rightarrow \tilde{\chi}_i^0 W^+ W^-} &= \frac{i}{4M_P} \frac{1}{(p-k)^2 - m_{\tilde{\chi}_j^\pm}^2 + im_{\tilde{\chi}_j^\pm} \Gamma_{\tilde{\chi}_j^\pm}} g \bar{u}(q') \gamma_\sigma [P_R O_{ij}^R + P_L O_{ij}^L] \\
&\cdot \left(\not{p} - \not{k} + m_{\tilde{\chi}_j^\pm} \right) \left\{ (P_R V_{j1} + P_L U_{j1}^*) \gamma^\mu [\gamma_\rho, \not{k}] \right. \\
&+ \left. 2g (P_R v_2 V_{j2} + P_L v_1 U_{j2}^*) \gamma^\mu \gamma_\rho \right\} \psi_\mu(p) \epsilon^{\rho*}(k) \epsilon^{\sigma*}(k'),
\end{aligned}$$

$$\begin{aligned}
i\mathcal{M}_{\tilde{G} \rightarrow W^- \tilde{\chi}_j^{+*} \rightarrow \tilde{\chi}_i^0 W^+ W^-} &= -\frac{i}{4M_P} \frac{1}{(p-k')^2 - m_{\tilde{\chi}_j^\pm}^2 + im_{\tilde{\chi}_j^\pm} \Gamma_{\tilde{\chi}_j^\pm}} g \bar{u}(q') \gamma_\rho [P_L O_{ij}^{R*} + P_R O_{ij}^{L*}] \\
&\cdot \left(\not{p} - \not{k}' + m_{\tilde{\chi}_j^\pm} \right) \left\{ (P_L V_{j1}^* + P_R U_{j1}) \gamma^\mu [\gamma_\sigma, \not{k}'] \right. \\
&+ \left. 2g (P_L v_2 V_{j2}^* + P_R v_1 U_{j2}) \gamma^\mu \gamma_\sigma \right\} \psi_\mu(p) \epsilon^{\rho*}(k) \epsilon^{\sigma*}(k'),
\end{aligned}$$

$$\begin{aligned}
i\mathcal{M}_{\tilde{G} \rightarrow \tilde{\chi}_i^0 H_1^0 \rightarrow \tilde{\chi}_i^0 W^+ W^-} &= \frac{i}{2M_P} \frac{1}{(k+k')^2 - m_{H_1^0}^2 + im_{H_1^0} \Gamma_{H_1^0}} g m_W \cos(\beta - \alpha) g_{\rho\sigma} \\
&\times \bar{u}(q') \left[P_R (\sin \alpha N_{i4} + \cos \alpha N_{i3}) - P_L (\sin \alpha N_{i4}^* + \cos \alpha N_{i3}^*) \right] \gamma^\mu \\
&\cdot (\not{k} + \not{k}') \psi_\mu(p) \epsilon^{\rho*}(k) \epsilon^{\sigma*}(k'),
\end{aligned}$$

$$\begin{aligned}
i\mathcal{M}_{\tilde{G} \rightarrow \tilde{\chi}_i^0 H_2^0 \rightarrow \tilde{\chi}_i^0 W^+ W^-} &= \frac{i}{2M_P} \frac{1}{(k+k')^2 - m_{H_2^0}^2 + im_{H_2^0} \Gamma_{H_2^0}} g m_W \sin(\beta - \alpha) g_{\rho\sigma} \\
&\times \bar{u}(q') \left[P_R (\cos \alpha N_{i4} - \sin \alpha N_{i3}) - P_L (\cos \alpha N_{i4}^* - \sin \alpha N_{i3}^*) \right] \gamma^\mu \\
&\cdot (\not{k} + \not{k}') \psi_\mu(p) \epsilon^{\rho*}(k) \epsilon^{\sigma*}(k'), \tag{A-30}
\end{aligned}$$

where $\psi_\mu(p)$ represents the decaying gravitino with momentum p , $\bar{u}(q')$ represents the produced neutralino with momentum q' , $\epsilon^{\rho*}(k)$ and $\epsilon^{\sigma*}(k')$ are the polarization four-vectors for the two W bosons with momenta k and k' , respectively, $g^{\alpha\beta}$ is the flat-space Lorentz metric tensor, the Γ factors in the propagators are the total widths of the exchanged particles and $O_{ij}^L = N_{i2}V_{j1}^* - \frac{1}{\sqrt{2}}N_{i4}V_{j2}^*$ and $O_{ij}^R = N_{i2}^*U_{j1} + \frac{1}{\sqrt{2}}N_{i3}^*U_{j2}$. The Feynman rules for the vertices $W^+W^-H_{1,2}^0$ and $\tilde{\chi}_j^\pm \tilde{\chi}_i^0 W^\mp$ are given in [113, 114]. The sum of the polarization states for gravitino is

$$\sum_{s=\pm\frac{3}{2}, \pm\frac{1}{2}} \psi_\mu^s(p)\bar{\psi}_\nu^s(p) = -(\not{p} + m_{3/2}) \left(g_{\mu\nu} - \frac{p_\mu p_\nu}{m_{3/2}^2} \right) - \frac{1}{3} \left(\gamma_\mu + \frac{p_\mu}{m_{3/2}} \right) (\not{p} - m_{3/2}) \left(\gamma_\nu + \frac{p_\nu}{m_{3/2}} \right),$$

and the phase space is the same as given in eq. (A-29).

A remark is in order for the process $\tilde{G} \rightarrow \tilde{\chi}_i^0 W^+W^-$. Because of the $1/m_W$ factors in the longitudinal polarization states of the W boson, one might worry that this process might have bad high-energy behavior. Correspondingly, if one restored the electroweak symmetry to make m_W vanish, then this process would diverge if there were still some terms proportional to negative powers of m_W in the final result. However, upon expanding the parameters in terms of m_W , that is, expanding the elements of chargino and neutralino mixing matrices N , U , V , the masses $m_{\tilde{\chi}_i^0}$, $m_{\tilde{\chi}_j^\pm}$, and the angle α etc. (for the m_W dependence of these parameters, see, for example [115]), in the total amplitude, we have verified that all terms with negative powers of m_W cancel. As a result, this process has good high energy behavior. This is a highly non-trivial check on our calculation of the process $\tilde{G} \rightarrow \tilde{\chi}_i^0 W^+W^-$, verifying the relative magnitudes, signs and phases of all the individual contributions to the decay amplitudes.

We conclude by commenting on the differences between the amplitudes obtained and used this paper and those given [24] and [42], which are based on the gravitino interaction Lagrangian given in eq. (4.58) of [37]. This Lagrangian is different from that given in eq. (2.82) of [112], which we follow here. The latter reference uses the transformation from the two-component gravitino Lagrangian given in Wess and Bagger [116] to the four-component Lagrangian which, as pointed out at the footnote on page 205 of [114], requires a factor of i when one defines the Majorana spinors. This factor results in a sign difference when one writes down the Feynman rules using the matter part of the Lagrangian. We also note that our result for gravitino $\rightarrow Z + \chi$ differs from [42], in that it includes the Higgsino contribution.

References

- [1] J. Dunkley *et al.* [WMAP Collaboration], *Astrophys. J.* accepted [arXiv:0803.0586 astro-ph].
- [2] R. H. Cyburt, B. D. Fields and K. A. Olive, *New Astron.* **6** (2001) 215 [arXiv:astro-ph/0102179].
- [3] R. H. Cyburt, B. D. Fields and K. A. Olive, *Astropart. Phys.* **17** (2002) 87 [arXiv:astro-ph/0105397].
- [4] R. H. Cyburt, B. D. Fields and K. A. Olive, *Phys. Lett.* **B567**, 227 (2003); A. Coc, E. Vangioni-Flam, P. Descouvemont, A. Adahchour and C. Angulo, *Astrophys. J.* **600** (2004) 544 [arXiv:astro-ph/0309480]; A. Cuoco, F. Iocco, G. Mangano, G. Miele, O. Pisanti and P. D. Serpico, *Int. J. Mod. Phys. A* **19** (2004) 4431 [arXiv:astro-ph/0307213]; B.D. Fields and S. Sarkar in: C. Amsler *et al.* [Particle Data Group], *Phys. Lett. B* **667**, 1 (2008); P. Descouvemont, A. Adahchour, C. Angulo, A. Coc and E. Vangioni-Flam, *ADNDT* **88** (2004) 203 [arXiv:astro-ph/0407101].
- [5] R. H. Cyburt, *Phys. Rev. D* **70**, 023505 (2004) [arXiv:astro-ph/0401091].
- [6] R. H. Cyburt, B. D. Fields and K. A. Olive, *JCAP* **0811** (2008) 012. [arXiv:0808.2818 [astro-ph]].
- [7] D. Lindley, *Astrophys. J.* **294** (1985) 1.
- [8] J. R. Ellis, D. V. Nanopoulos and S. Sarkar, *Nucl. Phys. B* **259** (1985) 175.
- [9] D. Lindley, *Phys. Lett. B* **171** (1986) 235.
- [10] R. J. Scherrer and M. S. Turner, *Astrophys. J.* **331** (1988) 19.
- [11] M. H. Reno and D. Seckel, *Phys. Rev. D* **37** (1988) 3441.
- [12] S. Dimopoulos, R. Esmailzadeh, L. J. Hall and G. D. Starkman, *Astrophys. J.* **330**, 545 (1988); S. Dimopoulos, R. Esmailzadeh, L. J. Hall and G. D. Starkman, *Nucl. Phys. B* **311** (1989) 699.
- [13] J. Ellis *et al.*, *Nucl. Phys. B* **337**, 399 (1992).
- [14] M. Kawasaki and T. Moroi, *Prog. Theor. Phys.* **93** (1995) 879 [arXiv:hep-ph/9403364].

- [15] M. Kawasaki and T. Moroi, *Astrophys. J.* **452**, 506 (1995).
- [16] E. Holtmann, M. Kawasaki, K. Kohri and T. Moroi, *Phys. Rev. D* **60**, 023506 (1999) [arXiv:hep-ph/9805405].
- [17] K. Jedamzik, *Phys. Rev. Lett.* **84**, 3248 (2000) [arXiv:astro-ph/9909445].
- [18] M. Kawasaki, K. Kohri and T. Moroi, *Phys. Rev. D* **63** (2001) 103502 [arXiv:hep-ph/0012279].
- [19] K. Kohri, *Phys. Rev. D* **64** (2001) 043515 [arXiv:astro-ph/0103411].
- [20] R. H. Cyburt, J. R. Ellis, B. D. Fields and K. A. Olive, *Phys. Rev. D* **67** (2003) 103521 [arXiv:astro-ph/0211258].
- [21] K. Jedamzik, *Phys. Rev. D* **70** (2004) 063524 [arXiv:astro-ph/0402344]; K. Jedamzik, *Phys. Rev. D* **70** (2004) 083510 [arXiv:astro-ph/0405583].
- [22] M. Kawasaki, K. Kohri and T. Moroi, *Phys. Lett. B* **625** (2005) 7 [arXiv:astro-ph/0402490]; *Phys. Rev. D* **71** (2005) 083502 [arXiv:astro-ph/0408426].
- [23] J. R. Ellis, K. A. Olive and E. Vangioni, *Phys. Lett. B* **619**, 30 (2005) [arXiv:astro-ph/0503023].
- [24] K. Kohri, T. Moroi and A. Yotsuyanagi, *Phys. Rev. D* **73**, 123511 (2006) [arXiv:hep-ph/0507245].
- [25] D. G. Cerdeno, K. Y. Choi, K. Jedamzik, L. Roszkowski and R. Ruiz de Austri, *JCAP* **0606**, 005 (2006) [arXiv:hep-ph/0509275].
- [26] K. Jedamzik, K. Y. Choi, L. Roszkowski and R. Ruiz de Austri, *JCAP* **0607**, 007 (2006) [arXiv:hep-ph/0512044].
- [27] K. Jedamzik, *Phys. Rev. D* **74**, 103509 (2006) [arXiv:hep-ph/0604251].
- [28] F. D. Steffen, *JCAP* **0609**, 001 (2006) [arXiv:hep-ph/0605306].
- [29] R. H. Cyburt, J. R. Ellis, B. D. Fields, K. A. Olive and V. C. Spanos, *JCAP* **0611**, 014 (2006) [arXiv:astro-ph/0608562].
- [30] A. Bouquet and P. Salati, *Nucl. Phys. B* **284**, 557 (1987); J. E. Kim, B. Kyae and J. D. Park, arXiv:hep-ph/9810503.

- [31] J. Ellis, J.S. Hagelin, D.V. Nanopoulos, K.A. Olive and M. Srednicki, *Nucl. Phys.* **B238**, 453 (1984).
- [32] D. V. Nanopoulos, K. A. Olive and M. Srednicki, *Phys. Lett. B* **127** (1983) 30.
- [33] J. R. Ellis, J. E. Kim and D. V. Nanopoulos, *Phys. Lett. B* **145** (1984) 181.
- [34] R. Juskiewicz, J. Silk and A. Stebbins, *Phys. Lett. B* **158** (1985) 463.
- [35] M. Kawasaki and K. Sato, *Phys. Lett. B* **189** (1987) 23.
- [36] T. Moroi, H. Murayama and M. Yamaguchi, *Phys. Lett. B* **303** (1993) 289.
- [37] T. Moroi, arXiv:hep-ph/9503210.
- [38] J. R. Ellis, D. V. Nanopoulos, K. A. Olive and S. J. Rey, *Astropart. Phys.* **4** (1996) 371 [arXiv:hep-ph/9505438].
- [39] M. Bolz, A. Brandenburg and W. Buchmuller, *Nucl. Phys. B* **606** (2001) 518 [arXiv:hep-ph/0012052].
- [40] J. Pradler and F. D. Steffen, *Phys. Lett. B* **648**, 224 (2007) [arXiv:hep-ph/0612291].
- [41] J. L. Feng, A. Rajaraman and F. Takayama, *Phys. Rev. D* **68** (2003) 063504 [arXiv:hep-ph/0306024]; J. L. Feng, S. F. Su and F. Takayama, *Phys. Rev. D* **70** (2004) 063514 [arXiv:hep-ph/0404198].
- [42] J. L. Feng, S. Su and F. Takayama, *Phys. Rev. D* **70** (2004) 075019 [arXiv:hep-ph/0404231].
- [43] J. R. Ellis, K. A. Olive, Y. Santoso and V. C. Spanos, *Phys. Lett. B* **588** (2004) 7 [arXiv:hep-ph/0312262].
- [44] J. R. Ellis, K. A. Olive, Y. Santoso and V. C. Spanos, *Phys. Lett. B* **573** (2003) 162 [arXiv:hep-ph/0305212]; J. R. Ellis, K. A. Olive, Y. Santoso and V. C. Spanos, *Phys. Rev. D* **70** (2004) 055005 [arXiv:hep-ph/0405110].
- [45] J. R. Ellis, K. A. Olive, Y. Santoso and V. C. Spanos, *Phys. Lett. B* **565**, 176 (2003) [arXiv:hep-ph/0303043].

- [46] H. Baer and C. Balazs, JCAP **0305**, 006 (2003) [arXiv:hep-ph/0303114]; A. B. Lahanas and D. V. Nanopoulos, Phys. Lett. B **568**, 55 (2003) [arXiv:hep-ph/0303130]; U. Chattopadhyay, A. Corsetti and P. Nath, Phys. Rev. D **68**, 035005 (2003) [arXiv:hep-ph/0303201]; C. Munoz, Int. J. Mod. Phys. A **19**, 3093 (2004) [arXiv:hep-ph/0309346]; R. Arnowitt, B. Dutta and B. Hu, arXiv:hep-ph/0310103.
- [47] M. Battaglia *et al.*, Eur. Phys. J. C **22**, 535 (2001) [arXiv:hep-ph/0106204]; M. Battaglia, A. De Roeck, J. R. Ellis, F. Gianotti, K. A. Olive and L. Pape, Eur. Phys. J. C **33**, 273 (2004) [arXiv:hep-ph/0306219].
- [48] R. I. Epstein, J. M. Lattimer and D. N. Schramm, Nature **263**, 198 (1976); T. Prodanovic and B. D. Fields, Astrophys. J. **597**, 48 (2003) [arXiv:astro-ph/0307183].
- [49] J. L. Linsky *et al.*, Astrophys. J. **647**, 1106 (2006) [arXiv:astro-ph/0608308].
- [50] E. Vangioni-Flam, K. A. Olive and N. Prantzos, Astrophys. J. **427**, 618 (1994) [arXiv:astro-ph/9310021]; S. Scully, M. Casse, K. A. Olive and E. Vangioni-Flam, Astrophys. J. **476**, 521 (1997) [arXiv:astro-ph/9607106]; G. Steigman, D. Romano and M. Tosi, Mon. Not. Roy. Astron. Soc. **378**, 576 (2007) [arXiv:astro-ph/0703682]; T. Prodanovic and B. D. Fields, JCAP **0809**, 003 (2008) [arXiv:0804.3095 [astro-ph]].
- [51] S. Burles and D. Tytler, Astrophys. J. **499**, 699 (1998) [arXiv:astro-ph/9712108].
- [52] S. Burles and D. Tytler, Astrophys. J. **507**, 732 (1998) [arXiv:astro-ph/9712109].
- [53] J. M. O’Meara, D. Tytler, D. Kirkman, N. Suzuki, J. X. Prochaska, D. Lubin and A. M. Wolfe, Astrophys. J. **552**, 718 (2001) [arXiv:astro-ph/0011179].
- [54] M. Pettini and D. V. Bowen, Astrophys. J. **560**, 41 (2001) [arXiv:astro-ph/0104474].
- [55] D. Kirkman, D. Tytler, N. Suzuki, J. M. O’Meara and D. Lubin, Astrophys. J. Suppl. **149**, 1 (2003) [arXiv:astro-ph/0302006].
- [56] J. M. O’Meara, S. Burles, J. X. Prochaska, G. E. Prochter, R. A. Bernstein and K. M. Burgess, Astrophys. J. **649**, L61 (2006) [arXiv:astro-ph/0608302].
- [57] M. Pettini, B. J. Zych, M. T. Murphy, A. Lewis and C. C. Steidel, MNRAS **391**, 1499 (2008) [arXiv:0805.0594 [astro-ph]].
- [58] Bania, T. M., Rood, R. T., & Balser, D. S. 2002, Nature, **415**, 54.

- [59] E. Vangioni-Flam, K. A. Olive, B. D. Fields and M. Casse, *Astrophys. J.* **585**, 611 (2003) [arXiv:astro-ph/0207583].
- [60] B. D. Fields, K. A. Olive, J. Silk, M. Casse and E. Vangioni-Flam, *Astrophys. J.* **563**, 653 (2001) [arXiv:astro-ph/0107389].
- [61] G. Sigl, K. Jedamzik, D. N. Schramm and V. S. Berezinsky, *Phys. Rev. D* **52** (1995) 6682 [arXiv:astro-ph/9503094].
- [62] M. Peimbert, A. Peimbert and M.T. Ruiz, *Astrophys. J.* **541**, 688 (2000); A. Peimbert, M. Peimbert and V. Luridiana, *Astrophys. J.* **565**, 668 (2002).
- [63] Y. I. Izotov and T. X. Thuan, *Astrophys. J.* **500**, 188 (1998).
- [64] K.A. Olive, and E. Skillman, *New Astronomy*, **6**, 119 (2001).
- [65] Y. I. Izotov and T. X. Thuan, *Astrophys. J.* **602**, 200 (2004) [arXiv:astro-ph/0310421].
- [66] K. A. Olive and E. D. Skillman, *Astrophys. J.* **617**, 29 (2004) [arXiv:astro-ph/0405588].
- [67] M. Fukugita and M. Kawasaki, *Astrophys. J.* **646**, 691 (2006) [arXiv:astro-ph/0603334].
- [68] F. Spite, M. Spite, *Astronomy & Astrophysics*, **115** (1992) 357.
- [69] S. G. Ryan, T. C. Beers, K. A. Olive, B. D. Fields, and J. E. Norris *Astrophys. J. Lett.* **530** (2000) L57 [arXiv:astro-ph/9905211].
- [70] P. Bonifacio *et al.*, *Astron. Astrophys.*, **390**, 91 (2002). [arXiv:astro-ph/0204332].
- [71] L. Pasquini and P. Molaro, *Astron. Astrophys.* **307**, 761 (1996).
- [72] F. Thevenin, C. Charbonnel, J. A. d. Pacheco, T. P. Idiart, G. Jasiewicz, P. de Laverny and B. Plez, *Astron. Astrophys.* **373**, 905 (2001) [arXiv:astro-ph/0105166].
- [73] P. Bonifacio, *Astron. Astrophys.* **395**, 515 (2002) [arXiv:astro-ph/0209434].
- [74] A. Hosford, S. G. Ryan, A. E. G. Perez, J. E. Norris and K. A. Olive, *Astron. Astrophys.* **493**, 601 (2009) [arXiv:0811.2506 [astro-ph]].
- [75] S. Vauclair and C. Charbonnel, *Astrophys. J.* **502**, 372 (1998); M. H. Pinsonneault, T. P. Walker, G. Steigman and V. K. Narayanan, *Astrophys. J.* **527**, 180 (2002) [arXiv:astro-ph/9803073]; M. H. Pinsonneault, G. Steigman, T. P. Walker and

- V. K. Narayanan, *Astrophys. J.* **574**, 398 (2002) [arXiv:astro-ph/0105439]; O. Richard, G. Michaud and J. Richer, *Astrophys. J.* **619**, 538 (2005) [arXiv:astro-ph/0409672]; A. J. Korn *et al.*, *Nature* **442** (2006) 657 [arXiv:astro-ph/0608201].
- [76] V.V. Smith, D.L. Lambert, and P.E. Nissen, *Astrophys. J.* **408**, 262 (1993); *Astrophys. J.* **506**, 405 (1998); L.M. Hobbs and J.A. Thorburn, *Astrophys. J. Lett.*, **428**, L25 (1994); *Astrophys. J.* **491**, 772 (1997); R. Cayrel, M. Spite, F. Spite, E. Vangioni-Flam, M. Cassé, and J. Audouze, *Astron. Astrophys.* **343**, 923 (1999).
- [77] M. Asplund, D. L. Lambert, P. E. Nissen, F. Primas and V. V. Smith, *Astrophys. J.* **644**, 229 (2006) [arXiv:astro-ph/0510636].
- [78] D. Thomas, D. N. Schramm, K. A. Olive and B. D. Fields, *Astrophys. J.* **406**, 569 (1993) [arXiv:astro-ph/9206002].
- [79] E. Vangioni-Flam, M. Cassé, R. Cayrel, J. Audouze, M. Spite, and F. Spite, *New Astronomy*, **4**, 245 (1999) [arXiv:astro-ph/9811327].
- [80] R. Cayrel *et al.*, *Astronomy & Astrophys.* **473**, L37 (2007).
- [81] G. Steigman, B. D. Fields, K. A. Olive, D. N. Schramm and T. P. Walker, *Astrophys. J.* **415**, L35 (1993).
- [82] B.D.Fields and K.A. Olive, *New Astronomy*, **4**, 255 (1999) [arXiv:astro-ph/9811183].
- [83] M. Kusakabe, T. Kajino and G. J. Mathews, *Phys. Rev. D* **74**, 023526 (2006) [arXiv:astro-ph/0605255]; M. Kusakabe, T. Kajino, R. N. Boyd, T. Yoshida and G. J. Mathews, *Phys. Rev. D* **76**, 121302 (2007) [arXiv:0711.3854 [astro-ph]]; M. Kusakabe, T. Kajino, R. N. Boyd, T. Yoshida and G. J. Mathews, arXiv:0711.3858 [astro-ph].
- [84] K. Jedamzik, *Phys. Rev. D* **77**, 063524 (2008) [arXiv:0707.2070 [astro-ph]]; K. Jedamzik, *JCAP* **0803**, 008 (2008) [arXiv:0710.5153 [hep-ph]].
- [85] D. Cumberbatch, K. Ichikawa, M. Kawasaki, K. Kohri, J. Silk and G. D. Starkman, *Phys. Rev. D* **76**, 123005 (2007) [arXiv:0708.0095 [astro-ph]].
- [86] S. Bailly, K. Jedamzik and G. Moulataka, arXiv:0812.0788 [hep-ph]; S. Bailly, K. Y. Choi, K. Jedamzik and L. Roszkowski, *JHEP* **0905**, 103 (2009) [arXiv:0903.3974 [hep-ph]].

- [87] E. Rollinde, E. Vangioni-Flam and K. A. Olive, *Astrophys. J.* **627**, 666 (2005) [arXiv:astro-ph/0412426]; E. Rollinde, E. Vangioni and K. A. Olive, *Astrophys. J.* **651**, 658 (2006) [arXiv:astro-ph/0605633]; E. Rollinde, D. Maurin, E. Vangioni, K. A. Olive and S. Inoue, *Astrophys. J.* **673**, 676 (2008) [arXiv:0707.2086 [astro-ph]]; T. Prodanovic and B. D. Fields, *Phys. Rev. D* **76**, 083003 (2007) [arXiv:0709.3300 [astro-ph]]; M. Kusakabe, arXiv:0803.3401 [astro-ph].
- [88] M. Pospelov, *Phys. Rev. Lett.* **98**, 231301 (2007) [arXiv:hep-ph/0605215]; C. Bird, K. Koopmans and M. Pospelov, *Phys. Rev. D* **78**, 083010 (2008) [arXiv:hep-ph/0703096].
- [89] K. Kohri and F. Takayama, *Phys. Rev. D* **76**, 063507 (2007) [arXiv:hep-ph/0605243].
- [90] M. Kaplinghat and A. Rajaraman, *Phys. Rev. D* **74**, 103004 (2006) [arXiv:astro-ph/0606209].
- [91] K. Hamaguchi, T. Hatsuda, M. Kamimura, Y. Kino and T. T. Yanagida, *Phys. Lett. B* **650**, 268 (2007) [arXiv:hep-ph/0702274].
- [92] T. Jittoh, K. Kohri, M. Koike, J. Sato, T. Shimomura and M. Yamanaka, *Phys. Rev. D* **76**, 125023 (2007) [arXiv:0704.2914 [hep-ph]].
- [93] J. Pradler and F. D. Steffen, *Phys. Lett. B* **666**, 181 (2008) [arXiv:0710.2213 [hep-ph]]; J. Pradler and F. D. Steffen, *Eur. Phys. J. C* **56**, 287 (2008) [arXiv:0710.4548 [hep-ph]]; F. D. Steffen, *Phys. Lett. B* **669**, 74 (2008) [arXiv:0806.3266 [hep-ph]].
- [94] M. Pospelov, arXiv:0712.0647 [hep-ph].
- [95] M. Pospelov, J. Pradler and F. D. Steffen, *JCAP* **0811**, 020 (2008) [arXiv:0807.4287 [hep-ph]].
- [96] J. L. Diaz-Cruz, J. R. Ellis, K. A. Olive and Y. Santoso, *JHEP* **0705**, 003 (2007) [arXiv:hep-ph/0701229]; K. Kohri and Y. Santoso, arXiv:0811.1119 [hep-ph].
- [97] M. Meneguzzi, J. Audouze, and H. Reeves, *Astronomy & Astrophys.*, **15** 337 (1971); R. Cowsik and L. W. Wilson, *In Denver 1973, Cosmic Ray Conference Vol.1, Denver 1973, 500-505*; R. Ramaty and R. E. Lingenfelter, in *Solar gamma-, X-, and EUV radiation*, ed. S. R. Kane, 363 (1975).

- [98] T. Sjostrand, P. Eden, C. Friberg, L. Lonnblad, G. Miu, S. Mrenna and E. Norrbin, Comput. Phys. Commun. **135** (2001) 238 [arXiv:hep-ph/0010017].
- [99] R. H. Cyburt and B. Davids, Phys. Rev. C **78**, 064614 (2008) [arXiv:0809.3240 [nucl-ex]].
- [100] J. P. Meyer, Astron. & Astrophys. Suppl. **7**, 417 (1972).
- [101] S. Ando, R. H. Cyburt, S. W. Hong and C. H. Hyun, Phys. Rev. C **74**, 025809 (2006) [arXiv:nucl-th/0511074].
- [102] P. Mohr *et al.*, Phys. Rev. C **50**, 1543 (1994).
- [103] W. A. Fowler and F. Hoyle, Astrophys. J. Suppl. **9**, 201 (1964).
- [104] V. N. Tystovich, Sov. Phys. JETP **15**, 561 (1962) [Zh. Eksp. Teor. Fiz. **42**, 803 (1962)].
- [105] R. J. Gould, Physica **58** (1972) 379.
- [106] M. Inokuti, Y. Itikawa and J. E. Turner, Rev. Mod. Phys. **50**, 23 (1978).
- [107] G. R. Blumenthal, Phys. Rev. D **1**, 1596 (1970).
- [108] M. J. Chodorowski, A. A. Zdziarski, and M. Sikora, Astrophys. J. **400**, 181 (1992)
- [109] V. S. Berezhinsky and S. I. Grigor'eva, Astron. Astrophys. **199**, 1 (1988).
- [110] R. J. Gould, Astrophys. J. **417**, 12 (1993).
- [111] J. E. Turner *et al.*, Phys. Rev. B **8** 4057 (1973).
- [112] J. Pradler, arXiv:0708.2786 [hep-ph].
- [113] J. F. Gunion and H. E. Haber, Nucl. Phys. B **272** (1986) 1.
- [114] H. E. Haber and G. L. Kane, Phys. Rept. **117** (1985) 75.
- [115] J. F. Gunion and H. E. Haber, Phys. Rev. D **37** (1988) 2515.
- [116] J. Wess and J. Bagger, *Supersymmetry and supergravity*, (Princeton University Press, Princeton, USA, 1992).